



AFRL-RX-TY-TR-2011-0046

**FIREFIGHTING AND EMERGENCY RESPONSE
STUDY OF ADVANCED COMPOSITES
AIRCRAFT; OBJECTIVE 1: COMPOSITE
MATERIAL DAMAGE IN MINOR AIRCRAFT
FIRES**

Robert T. Bocchieri, Kristofor S. Cozart, Steven P. Wells, Steven W. Kirkpatrick,
Robert A. MacNeill, Douglas S. Dierdorf, Mark A. Enlow
Applied Research Associates
430 West 5th Street, Suite 700
Panama City, FL 32401

John R. Hawk
Air Force Research Laboratory
Airbase Technologies Division
139 Barnes Drive, Suite 2
Tyndall Air Force Base, FL 32403-5323

Contract No. FA4819-09-C-0030

May 2013

DISTRIBUTION A. Approved for public release; distribution unlimited. AFCEC-201404; 10
January 2014.

**AIR FORCE RESEARCH LABORATORY
MATERIALS AND MANUFACTURING DIRECTORATE**

DISCLAIMER

Reference herein to any specific commercial product, process, or service by trade name, trademark, manufacturer, or otherwise does not constitute or imply its endorsement, recommendation, or approval by the United States Air Force. The views and opinions of authors expressed herein do not necessarily state or reflect those of the United States Air Force.

This report was prepared as an account of work sponsored by the United States Air Force. Neither the United States Air Force, nor any of its employees, makes any warranty, expressed or implied, or assumes any legal liability or responsibility for the accuracy, completeness, or usefulness of any information, apparatus, product, or process disclosed, or represents that its use would not infringe privately owned rights.

NOTICE AND SIGNATURE PAGE

Using Government drawings, specifications, or other data included in this document for any purpose other than Government procurement does not in any way obligate the U.S. Government. The fact that the Government formulated or supplied the drawings, specifications, or other data does not license the holder or any other person or corporation; or convey any rights or permission to manufacture, use, or sell any patented invention that may relate to them.

This report was cleared for public release by the AFCEC Public Affairs Office at Joint Base San Antonio-Lackland Air Force Base, Texas available to the general public, including foreign nationals. Copies may be obtained from the Defense Technical Information Center (DTIC) (<http://www.dtic.mil>).

AFRL-RX-TY-TR-2011-0046 HAS BEEN REVIEWED AND IS APPROVED FOR PUBLICATION IN ACCORDANCE WITH ASSIGNED DISTRIBUTION STATEMENT.

//SIGNED//

John R. Hawk, III, GS-13
Contracting Officer Representative

//SIGNED//

James E. Podolske, GS-14
Technical Advisor

This report is published in the interest of scientific and technical information exchange, and its publication does not constitute the Government's approval or disapproval of its ideas or findings.

REPORT DOCUMENTATION PAGE				Form Approved OMB No. 0704-0188	
<small>The public reporting burden for this collection of information is estimated to average 1 hour per response, including the time for reviewing instructions, searching existing data sources, gathering and maintaining the data needed, and completing and reviewing the collection of information. Send comments regarding this burden estimate or any other aspect of this collection of information, including suggestions for reducing the burden, to Department of Defense, Washington Headquarters Services, Directorate for Information Operations and Reports (0704-0188), 1215 Jefferson Davis Highway, Suite 1204, Arlington, VA 22202-4302. Respondents should be aware that notwithstanding any other provision of law, no person shall be subject to any penalty for failing to comply with a collection of information if it does not display a currently valid OMB control number.</small> PLEASE DO NOT RETURN YOUR FORM TO THE ABOVE ADDRESS.					
1. REPORT DATE (DD-MM-YYYY) 18 May 2013		2. REPORT TYPE Final Technical Report		3. DATES COVERED (From - To) 02-OCT-2009 -- 24-SEP-2012	
4. TITLE AND SUBTITLE Firefighting and Emergency Response Study of Advanced Composites Aircraft; Objective 1: Composite Material Damage in Minor Aircraft Fires				5a. CONTRACT NUMBER FA4819-09-C-0030	
				5b. GRANT NUMBER	
				5c. PROGRAM ELEMENT NUMBER 0909999F	
				5d. PROJECT NUMBER GOVT	
6. AUTHOR(S) *Bocchieri, R.; *Cozart, Kristofor S.; *Wells, Steven P.; *Kirkpatrick, Steven W.; *MacNeill, Robert A.; *Enlow, Mark A.; *Dierdorf, Douglas S.; and ^Hawk, John R.				5e. TASK NUMBER D0	
				5f. WORK UNIT NUMBER Q130D6A3	
7. PERFORMING ORGANIZATION NAME(S) AND ADDRESS(ES) *Applied Research Associates 430 West 5th Street, Suite 700 Panama City, FL 32401				8. PERFORMING ORGANIZATION REPORT NUMBER	
9. SPONSORING/MONITORING AGENCY NAME(S) AND ADDRESS(ES) ^Air Force Research Laboratory Materials and Manufacturing Directorate Airbase Technologies Division 139 Barnes Drive, Suite 2 Tyndall Air Force Base, FL 32403-5323				10. SPONSOR/MONITOR'S ACRONYM(S) AFRL/RXQES	
				11. SPONSOR/MONITOR'S REPORT NUMBER(S) AFRL-RX-TY-TR-2011-0046	
12. DISTRIBUTION/AVAILABILITY STATEMENT DISTRIBUTION A. Approved for public release; distribution unlimited.					
13. SUPPLEMENTARY NOTES Refer to Public Affairs Case # AFCEC-201404; 10 January 2014. Document contains color images.					
14. ABSTRACT Three aerospace composite materials with quasi-isotropic layup were exposed to varied uniform radiant heating to evaluate the delamination damage caused by the thermal environment. Three classes of matrix resins were evaluated with IM7 carbon fibers; epoxy 977-3, modified bismaleimide RM3002 and condensation polyimide AFR-PE-4. Thermal exposure was mild and indicative of a hydrocarbon pool fire at a standoff from the material. After exposure, the plates were machined into four-point bend and tensile samples and mechanically tested. Mechanical degradation in terms of tensile and flexural modulus and strength were documented as a function of exposure level. Microscopy of the machined sections was performed to document the observed damage.					
15. SUBJECT TERMS Thermal damage, radiant heating, delamination, polymer composite, mechanical degradation, microscopy, epoxy, modified bismaleimide, condensation polyimide					
16. SECURITY CLASSIFICATION OF:			17. LIMITATION OF ABSTRACT	18. NUMBER OF PAGES	19a. NAME OF RESPONSIBLE PERSON
a. REPORT	b. ABSTRACT	c. THIS PAGE			John R. Hawk
U	U	U	SAR	134	19b. TELEPHONE NUMBER (Include area code) 850-283-3736

Reset

TABLE OF CONTENTS

LIST OF FIGURES	iii
LIST OF TABLES	vii
1. SUMMARY	1
2. INTRODUCTION	4
3. ASSUMPTIONS, METHODS, AND PROCEDURES	7
3.1. Summary	7
3.2. Test Facilities	7
3.3. Materials	7
3.4. Procedures	9
3.4.1. Plate Heat Exposure	9
3.4.2. Moisture Content	15
3.4.3. Post-Fire Exposure Mechanical and Physical Testing	16
4. MODELING AND SIMULATION	26
4.1. Analysis Methodology	26
4.2. Aircraft Fire Model	26
4.2.1. Fire Scenarios	26
4.3. 1-D Heat Transfer Model with Pyrolysis and Thermal Damage	29
4.3.1. Background	29
4.3.2. One-Dimensional Heat Transfer Algorithm Overview	29
4.3.3. Model Improvements and Added Features	31
4.3.4. Pyrolysis Model Calibration	33
4.3.5. Temperature-Dependent Physical Properties	43
4.3.6. Predictions of Composite Plate Experiments	45
4.3.7. Heat Transfer Model Summary	50
4.4. Prediction of Post-Fire Mechanical Properties	51
5. RESULTS AND DISCUSSION	54
5.1. Physical Damage Evaluation	54
5.1.1. IM7/977-3	55
5.1.2. IM7/RM3002	61
5.1.3. IM7/AFR-PE-4	70
5.2. Thermal Exposure Histories	80
5.3. Delamination Time and Temperatures	87
5.4. Mechanical Test Results	91
5.4.1. Flexural Testing: Four-Point Bending	91
5.4.2. Tensile Testing	95
5.5. Modeling and Simulation of F-22 Fire Scenarios	97
5.5.1. Engine Nacelle Model	97
5.5.2. Engine Nacelle Fire	100
5.5.3. Small Fuel Spill Model	103
5.5.4. Small Fuel Spill Fire	105
5.5.5. Small Fuel Spill Fire Adjacent to Aircraft	107
6. CONCLUSIONS	109
7. RECOMMENDATIONS	112
7.1. Operational Recommendations	112
7.2. Technical Recommendations	112

7.2.1. Heat Exposure Testing.....	112
7.2.2. Thermally-induced Delamination Model.....	113
7.2.3. Heat Transfer Modeling.....	113
7.2.4. High-Fidelity Modeling and Simulation.....	113
8. REFERENCES	114
APPENDIX.....	116
LIST OF SYMBOLS, ABBREVIATIONS, AND ACRONYMS	126

LIST OF FIGURES

	Page
Figure 1. Analysis Methodology for Determining Firefighting Response Requirements	4
Figure 2. Test Plate Layout	8
Figure 3. IR Heater Up to Temperature	9
Figure 4. Top View Drawing of Heater Setup	10
Figure 5. Sample Table in Position under the Heater	11
Figure 6. Test Table Fixture and Instrumentation	12
Figure 7. Base Test Table Insulation	12
Figure 8. R2 Composite Plate Ready to be Exposed	12
Figure 9. Spacer Insulation for an IM7/AFR-PE-4 Test	13
Figure 10. Plate A8 with Edge Insulation	13
Figure 11. Test Table Ready; Surrogate Table under Heater During Preheat	14
Figure 12. Mass Gain for Three Material Plates Conditioned in a Humidity Chamber at 95 Percent Relative Humidity at 35 °C	15
Figure 13. Typical Panel Cut-Outs	16
Figure 14. Rotary Grinder/Polisher used to Prepare Samples	17
Figure 15. Unpolished Sample with Attached Samplklips (left), Polished Sample with Polished Face Down (iddle), and Polished Sample with Polished Face Up (right)	18
Figure 16. Epoxy Applied to the Top and Bottom of the Composite Samples	20
Figure 17. The Tabbing Procedure after Placing the Top Fiberglass Tabs	20
Figure 18. A Tabbed Composite Sample	20
Figure 19. Strain Measurements of Tensile Specimens	21
Figure 20. Typical Stress Strain Results	22
Figure 21. Small Bend Fixture	23
Figure 22. Typical Bend Results	25
Figure 23. Discretized Heat Transfer Model for a Composite Laminate	30
Figure 24. Comparison of Original and Revised Pyrolysis Model	32
Figure 25. Updated Heat Transfer Algorithm Flow Chart	33
Figure 26. Cycom IM7/977-3 Raw TGA Data	34
Figure 27. IM7/RM3002 Raw TGA Data	35
Figure 28. IM7/AFR-PE-4 Raw TGA Data	35
Figure 29. Decomposed Mass Fraction of IM7/RM3002 at 10 and 20 °C/min	36
Figure 30. Comparison of 20 °C/min TGA Data and Single-Process Arrhenius Model	37
Figure 31. Cycom IM7/977-3 System Decomposition Fit Comparison to TGA Data at Both Tested Heating Rates	38
Figure 32. IM7/RM3002 System Decomposition Fit Comparison to TGA Data at Both Tested Heating Rates	39
Figure 33. IM7/ARFPE System Decomposition Fit Comparison to TGA Data at Both Tested Heating Rates	39
Figure 34. Cycom IM7/977-3 System Decomposition Model, 20 °C/min Heating Rate	40
Figure 35. IM7/RM3002 System Decomposition Model, 20 °C/min Heating Rate	41
Figure 36. IM7/ARFPE System Decomposition Model, 20 °C/min Heating Rate	42
Figure 37. Temperature-Dependent Physical Properties	45
Figure 38. Example of Modeled Average Heat Flux Compared to Test Data	46

Figure 39. Predicted and Measured Temperatures of IM7/RM3002 Exposed to a Heat Flux of 35 kW/m ²	47
Figure 40. Predicted and Measured Temperatures of IM7/RM3002 Exposed to a Heat Flux of 25 kW/m ²	48
Figure 41. Predicted and Measured Temperatures of IM7/RM3002 Exposed to a Heat Flux of 15 kW/m ²	48
Figure 42. Predicted and Measured Temperatures of IM7/977-3 Exposed to a Heat Flux of 35 kW/m ²	49
Figure 43. Predicted and Measured Temperatures of IM7/977-3 Exposed to a Heat Flux of 15 kW/m ²	49
Figure 44. Predicted and Measured Temperatures of IM7/AFR-PE-4 Exposed to a Heat Flux of 35 kW/m ²	50
Figure 45. Schematic of Resin Degradation Through Laminate, with Resin Decomposition Zone and Residual Char, Alongside a Cross-Section Through a Glass/Polyester Woven Roving Laminate Exposed to a Heat Flux of 50 kW/m ² [13].....	51
Figure 46. Plate C4 Before (a) and After Exposure at 15.2 kW/m ² for 844s (b & c).....	56
Figure 47. Plate C9 (0.3 Percent Moisture Content) before (a) and After Exposure at 15.4 kW/m ² for 601s (b & c)	57
Figure 48. IR Image of C4 Approximately 20 s after Removal from Heat Source	58
Figure 49. IR Image of C9 (0.3 Percent Moisture Content) Approximately 8 s after Removal from Heat Source	59
Figure 50. Cross-Section of IM7/977-3 Plate after Being Cut with a Water-Jet.....	59
Figure 51. Cross Section of Plate C4 - Exposed at 15 kW/m ² for 844s	60
Figure 52. Cross section of plate C9 (0.3 percent moisture content) - Exposed at 15.4 kW/m ² for 601 s	61
Figure 53. Plate R6 before (top) and after Exposure at 34.2 kW/m ² for 101 s (bottom).....	62
Figure 54. Plate R2 before (top) and after Exposure at 26.2 kW/m ² for 214 s (bottom).....	63
Figure 55. Plate R3 before (top) and after Exposure at 24.9 kW/m ² for 91 s (bottom).....	63
Figure 56. Plate R8 before (top) and after Exposure at 15.3 kW/m ² for 1040 s (bottom).....	64
Figure 57. Plate R7 before (top) and after Exposure at 15.2 kW/m ² for 201 s (bottom).....	64
Figure 58. Plate R4 before (top) and after Exposure at 14.9 kW/m ² for 151 s (bottom).....	65
Figure 59. Plate R9 (0.4 percent Moisture Content) before (top) and after Exposure at 25.9 kW/m ² for 201 s (bottom)	65
Figure 60. IR image of R8 Approximately 8 s after Removal from Heat Source	66
Figure 61. IR image of R9 (0.4 percent Moisture Content) Approximately 30 s after Removal from Heat Source	66
Figure 62. Cross-section of IM7/RM3002 Plate after being Cut with a Water-jet.....	67
Figure 63. Cross section of Plate R2 – Exposed at 26.2 kW/m ² for 214 s	67
Figure 64. Cross section of Plate R3 – Exposed at 24.9 kW/m ² for 91 s	67
Figure 65. Cross section of Plate R6 - Exposed at 34.2 kW/m ² for 101 s	68
Figure 66. Cross section of Plate R8 – Exposed at 15.3 kW/m ² for 1040 s	69
Figure 67. Cross section of Plate R9 (0.4 percent Moisture Content) - Exposed at 25.9 kW/m ² for 201 s	69
Figure 68. Plate A2 after Exposure at 36.5 kW/m ² for 20 s	71
Figure 69. Plate A3 before (top) and after Exposure at 34.1 kW/m ² for 127 s (bottom).....	71
Figure 70. Plate A8 before (top) and after Exposure at 35.1 kW/m ² for 151 s (bottom).....	72

Figure 71. Plate A9 (1.15 percent Moisture Content) before (top) and after Exposure at 35.2 kW/m ² for 152 s (bottom)	73
Figure 72. IR image of A3 Approximately 50 s after Removal from Heat Source	74
Figure 73. IR image of A8 Approximately 40 s after Removal from Heat Source	74
Figure 74. IR image of A9 (1.15 percent Moisture Content) Approximately 20 s after Removal from Heat Source	75
Figure 75. Cross-section of IM7/AFR-PE-4 Plate after being Cut with a Water-jet	75
Figure 76. Cross section of Plate A3–Exposed at 34.1 kW/m ² for 127 s	76
Figure 77. Cross section of Plate A8 – Exposed at 35.1 kW/m ² for 151 s	77
Figure 78. Plate A9 (1.15 percent Moisture Content) – Exposed at 35.2 kW/m ² for 152 s	78
Figure 79. Plate A9 (1.15 percent Moisture Content) During Delamination at 35.2 kW/m ²	79
Figure 80. Plate C4 Thermocouple Data (Exposed at 15.2 kW/m ² for 844s).....	81
Figure 81. Plate C9 Thermocouple Data (0.3 percent Moisture Content, Exposed at 15.4 kW/m ² for 601 s).....	81
Figure 82. Plate R6 Thermocouple Data (Exposed at 34.2 kW/m ² for 101 s).....	82
Figure 83. Plate R2 Thermocouple Data (Exposed at 26.2 kW/m ² for 214 s).....	82
Figure 84. Plate R9 Thermocouple Data (0.4 percent Moisture Content, Exposed at 25.9 kW/m ² for 201 s).....	83
Figure 85. Plate R3 Thermocouple Data (Exposed at 24.9 kW/m ² for 91 s).....	83
Figure 86. Plate R8 Thermocouple Data (Exposed at 15.3 kW/m ² for 1040 s).....	84
Figure 87. Plate R7 Thermocouple Data (Exposed at 15.2 kW/m ² for 201 s).....	84
Figure 88. Plate R4 Thermocouple Data (Exposed at 14.9 kW/m ² for 151 s).....	85
Figure 89. Plate A8 Thermocouple Data (Exposed at 35.1 kW/m ² for 151s)	85
Figure 90. Plate A3 Thermocouple Data (Exposed at 34.1 kW/m ² for 127 s)	86
Figure 91. Plate A2 Thermocouple Data (Exposed at 34.0 kW/m ² for 20 s)	86
Figure 92. Plate A9 Thermocouple Data (1.15 percent Moisture Content, Exposed at 35.2 kW/m ² for 152 s).....	87
Figure 93. Delamination Times in (a) Dry IM7/RM3002 Plates at Three Heat Flux Magnitudes and (b) In Dry Plates Tested at 35 kW/m ²	88
Figure 94. Effect of Moisture Content on the Time to Delamination at Fixed Heat Flux Magnitudes.....	88
Figure 95. IM7/RM3002 Plate Front (TC 1) and Back (TC 7) TC Temperatures at the Time of Delamination	89
Figure 96. TC Temperatures at the Time of Delamination for all Plates Tested.....	90
Figure 97. Flexural Strength	92
Figure 98. Chord Modulus	92
Figure 99. Maximum Strain.....	93
Figure 100. Tensile Strength.....	95
Figure 101. Ultimate Tensile Strain.....	96
Figure 102. Tensile Chord Modulus of Elasticity.....	96
Figure 103. Pratt & Whitney F119-PW-100 Engine	97
Figure 104. First Engine Nacelle Model.....	98
Figure 105. Velocity Vectors from the First Engine Nacelle Model.....	98
Figure 106. Second Engine Nacelle Spill Fire Model. View from Below	99
Figure 107. Flow Streams and Fire Zone Temperatures in the Second Nacelle Model	99
Figure 108. Nacelle Fire and Interior Gas Temperatures	101

Figure 109. Interior Surface Temperatures of Top Nacelle Plates at Five Time Steps after Fire Ignition (Plan View From Underneath – Engine Inlet on Right)	102
Figure 110. Fire Zone Gas Temperature Profiles in Two Planes at Four Time Steps.....	103
Figure 111. Flow Streams and Fuel Spill Fire	104
Figure 112. Maximum Surface Temperatures on the Wing Lower Skin.....	105
Figure 113. Flow Streams and Fuel Spill Fire at 3 s.....	106
Figure 114. Lower Wing Composite Surface Temperatures at 3 s.....	106

LIST OF TABLES

	Page
Table 1. Composite Materials	9
Table 2. Element Temperatures and Corresponding Heat Fluxes	10
Table 3. Bend Test Information	24
Table 4. Summary of the Computational Modeling Parameters.....	28
Table 5. Composite Plate Heat Exposure Summary	54
Table 6. Examples of Flexural Failure Modes with and without Heat-induced Damage	94
Table 7. Summary of the Engine Nacelle Model.....	100
Table 8. Summary of the Small Fuel Spill Model	105
Table 9. Heat Flux Adjacent to a Fuel Spill Fire	107
Table 10. Delamination Predictions of Composites	108
 Table A-1. RM-3002.....	 116
Table A-2. AFRPE.....	117
Table A-3. CYCOM.....	117
Table A-4. RM-3002.....	118
Table A-5. AFRPE.....	121
Table A-6. CYCOM.....	122

1. SUMMARY

The intent of this effort was to develop an analysis method for estimating firefighting response requirements in order to limit fire damage to composite materials in small, Class B (<\$1M damage, no serious injury) mishap conditions. The objective was to determine a time, fire size and damage relationship for the composites and incorporate these in an analysis model so that the Air Force Civil Engineering Fire Panel can use the model to estimate firefighting response requirements and establish CONOPS which will permit these types of fires to be routinely extinguished while the level of damage is still small.

The analysis methodology developed consists of four primary steps: (1) model a fire event to obtain the thermal loading on a given composite structure, (2) model heat transfer and pyrolysis in the composite material, (3) evaluate damage to the material as a function of time, (4) determine response times to limit damage to acceptable levels. This methodology is supported by heat exposure and mechanical testing of the materials of interest to develop the modeling parameters needed. The focus of this research was on developing and utilizing the modeling tools in the first three steps. The last step would include a cost analysis for repairs in order to determine acceptable damage levels. This methodology and the experiments planned to support this analysis were based on the assumption that the dominant damage mode would be pyrolysis of the matrix (thermal decomposition of the polymer substrate) used in the composites, as is frequently reported in the literature. This was found not to be the case for the test conditions considered, however, leaving the algorithms for Step 3 incomplete and in need of further development. As will be discussed, an interim solution is proposed until further research can be conducted.

Three intermediate modulus (and intermediate strength) carbon fiber (IM7) composites were evaluated with significantly different resin systems and glass transition temperatures (T_g). Materials were selected for this study as representative of a wide array of composites used in military aircraft. They represent, theoretically, three levels of service temperature: epoxy 977-3 < 120 °C, RM3002 < 200 °C and AFR-PE-4 < 260 °C. Higher T_g materials can, in general, operate at higher temperatures without damage. Composite plates with quasi-isotropic layout were exposed to controlled radiant heat fluxes on one face for specified time periods. To emulate a modest heat exposure from small fires, the material was not ignited on the front face, either artificially or as a product of the exposure level, so that heat exposure was mild and the primary source of heating was radiant heating. After exposure, the plates were mechanically tested and mechanical degradation was documented as a function of exposure level. Microscopy was also performed to document the observed damage.

In all materials tested and at all heat flux magnitudes applied, it was found that the composite plate experienced sudden and catastrophic damage prior to any significant pyrolysis in the form of delaminations, sometimes throughout the entire thickness. Delaminated samples displayed little residual mechanical strength in flexure (up to 85 percent strength loss) and greatly reduced tensile strength (up to 40 percent strength loss). Samples exposed to similar heat flux and durations, but removed from heat prior to delamination, showed little reduction in mechanical strength. The time at which delamination occurred was indicated by thermocouple (TC) data and global buckling of the plate. The delamination time was also affected by the water moisture content of the plate, with delamination occurring at shorter exposure times for plates with higher

moisture content. High pressure gases in the plate from water vapor and resin outgassing are postulated to cause this delamination.

This mechanism of sudden and significant damage was not anticipated at the beginning of the program. The predominant form of composite damage due to fire in the literature is progressive pyrolysis of the heat-exposed surface. Both the experimental program and analysis methodology planned were based on measuring and predicting the effect of progressive pyrolysis and other chemical changes to the resin. Consequently, the experimental approach and analysis methods had to be significantly modified to characterize the failure mechanism actually observed in experiments.

To perform the second step in the analysis a 1-D heat transfer model was developed, suitable for predicting the through-ply temperatures and pyrolysis. The nonlinear heat transfer and thermogravimetric properties for the materials studied were calibrated using test data for the three composites of interest. The model demonstrates good agreement up to the delamination temperature ranges seen during heat exposure tests. However, these properties should be refined using test methods specific to measuring through-thickness thermal conductivity and specific heat in order to improve model predictions for general use.

There are currently no models that can predict the thermally-induced delaminations seen in the experiments. Therefore, Step 3 of the analysis, to predict mechanical degradation of the material as a function of time, cannot currently be performed with the desired accuracy. Although the 1-D heat transfer model can be used to predict temperatures up to delamination, there are currently no good criteria for predicting when this damage occurs. A thermodynamic-mechanical model to predict delamination initiation and growth in general structural laminates is needed before a complete analysis can be performed.

In the absence of a robust method for predicting composite mechanical degradation as a function of time with the dominant damage from heat-induced delaminations, an interim solution is to use maximum allowable temperatures based on the results from the limited testing performed.. However, this approach may still lead to delamination in general laminates and heat exposure histories, especially since the effect of water moisture in the IM7/AFR-PE-4 laminate causes delamination well below the dry T_g. To be more conservative in predicting time to damage, the temperature limits should be below the delamination temperatures in the experiments, which may also lead to extremely short response time requirements. Additional heat-exposure and mechanical testing are needed to develop a thermodynamic-mechanical delamination model and to establish improved aircraft firefighting recommended response times. In this research, the maximum allowable temperatures to prevent delamination were used as an interim method for evaluating response times for several fire scenarios.

High-fidelity simulations of aircraft fires either in the interior of the engine nacelle or on the ground beneath the wing when flames impinge on the composite material surface indicate that damage is likely in the first minute or less, based on temperature restrictions to prevent delamination and the degree of pyrolysis calculated. Although this result is from only two fire scenarios, the fire sizes selected were small (6.8 l/min in the engine nacelle and 1-m diameter at 3.4 l/min on the ground).

In the engine nacelle scenario, rapid heating makes either delamination and/or severe pyrolysis of the composite likely in less than 30 s. The composite material surface temperatures exceeded the criteria for delamination found in experiments within 5 s of exposure. By 30 s of exposure, the nacelle top plate is more than 50-percent pyrolyzed through 40 percent of the plate thickness. This plate would have very little residual strength or stiffness. With either damage mode the composite would be rapidly damaged in the first 30 s of exposure. In the scenario with a small fuel spill beneath the wing, the model results indicate that the critical delamination temperature for the wing composite material would be exceeded on the lower wing in less than 45 s.

Radiant heating on a surface from adjacent pool fires (no direct flame impingement) was predicted with a simple analytical model. This model is based on spill fire size and distance from the center of the fire to predict heat flux. This heat flux was then used as input to the 1-D heat transfer model developed under this effort to predict material temperatures versus time. The time at which the temperature restrictions are reached are then determined for each fire scenario for a given composite type and thickness. Use of this model demonstrated that many pool fires close to the aircraft can result in radiant heating such that composite delamination does not occur in the first two to three minutes for the thicknesses tested in this research.

The conclusions from this research lead to recommendations in two areas: (1) operational recommendations, (2) technical recommendations. Operationally, for small fires with direct flame impingement on the aircraft, emphasis should be on faster response times, fire mitigation and reduction of fire risk. For small fires adjacent to the aircraft where the dominant mode of heating is from thermal radiation, the tools developed in this program can be used as an interim method to evaluate the required response time for varied fire scenarios. Technical recommendations include continued experimentation and improvements to modeling and simulation to better predict the damage modes observed in this study.

2. INTRODUCTION

The increasing use of composite materials and other specialized AF and DoD materials in aircraft and weapons systems intensifies the challenges to firefighters. Extinguishing composite fires was a serious problem at recent F-22 [1] and B-2 [2,3] mishaps, and little is known about how composite aircraft burn, the hazards to first responders, and the most effective methods to prevent, attack, and extinguish the fires. This work is intended to provide interim solutions to these problems through an understanding of the basic processes of composite damage and developing a working model that relates composite damage to fire conditions and exposure times. The focus is on fire damage to composite structures in small, Class B (<\$1M damage, no serious injury) mishap conditions. The Air Force Civil Engineering Fire Panel will use the model to estimate firefighting response requirements and establish CONOPS which will permit these types of fires to be routinely extinguished while the level of damage is still small.

The analysis methodology developed consists of four primary steps shown in Figure 1: (1) model a fire event to obtain the thermal loading on a given composite structure, (2) model heat transfer and pyrolysis in the composite material, (3) evaluate damage to the material as a function of time, (4) determine response times to limit damage to acceptable levels. This methodology is supported by heat exposure and mechanical testing of the materials of interest to develop the modeling parameters needed. The focus of this research was on developing and utilizing the modeling tools in the first three steps. The last step would include a cost analysis for repairs in order to determine acceptable damage levels, and is outside the scope of this effort.

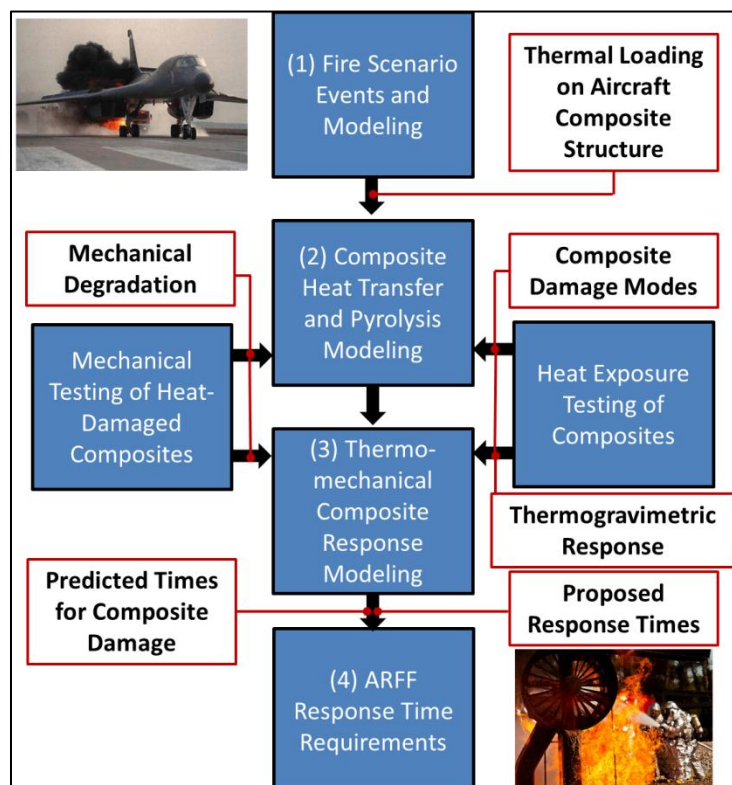


Figure 1. Analysis Methodology for Determining Firefighting Response Requirements

In the first step of the analysis method, either a simple heat exposure analysis or detailed CFD solver is used to predict the transient flow and heating environment on a portion of the aircraft composite structure some distance from the fire source. In Step 2, the heating environment predicted is applied to a one-dimensional (1-D) Finite Element heat transfer model, further developed under this effort, which predicts the transient through-thickness temperature change and degree of pyrolysis in the composite at different locations on the structure. Finally, in Step 3, the predicted through-thickness pyrolysis information from Step 2 is used in algorithms for predicting the post-fire mechanical properties of a composite. These algorithms in Step 3 and the experiments planned to support this analysis were based on the dominant damage modes to fire-exposed composites frequently reported in the literature, pyrolysis of the polymer matrix. However, the composite plates tested in this effort experienced sudden and catastrophic delaminations prior to any significant pyrolysis. There are currently no models that can predict the thermally-induced delaminations seen in the experiments. Therefore, Step 3 of the analysis, to predict mechanical degradation of the material as a function of time, requires further development, as will be discussed.

Thermal damage to composite materials is generally thought to result from three sequential mechanisms. The first mechanism is the loss of fiber/matrix coupling when the matrix material (resin) is heated above the T_g . This results in “melting” of the “crystalline” regions, though the actual process is more complex than this simplified description [4]. The largest portion of the thermal damage under fire and other high heat flux conditions is the thermal decomposition (pyrolysis) of the matrix resulting in the breakdown of the matrix polymer to smaller organic molecules most of which are volatile and boil off from the composite material.

When the temperature is high enough and quantity of volatiles is in the range of a few volume percent in air, the mixture will ignite. These gases burning next to the composite surface greatly increase the heat flux and often result in a runaway combustion process. This pyrolysis process leaves residual carbonaceous material described as “char.” The final combustion process is the solid state combustion of the char leaving only a residual mass of non-combustible carbon and/or glass fibers. The key assumption is that these reactions are dependent only on the polymer composition with only second order effects due to composite layup and fiber composition. This is probably a safe assumption only within a specific range of materials.

Three IM7 carbon fiber composites were evaluated; epoxy 977-3, modified bismaleimide (BMI) RM3002 and condensation polyimide AFR-PE-4. The matrices in these composites have a T_g of 221 °C, 296 °C and 340 °C, respectively. Two types of heat-exposure experiments were conducted: (1) Thermogravimetric tests to support the development of the 1-D heat transfer analysis in Step 2, and (2) composite plates with quasi-isotropic layup were exposed to controlled radiant heat fluxes on one face for specified time periods.

In the second type of tests, plates were thermally insulated on the back side and around the edges, to minimize edge damage. The material was not ignited on the front face, either artificially or as a product of the exposure level, so that heat exposure was mild and the primary source of heating was radiant heating. Thermocouples were placed throughout the thickness during manufacture. After exposure, the plates were machined into 4-point bend and tensile samples and mechanically tested. Mechanical degradation in terms of reductions in tensile and

flexural modulus and strength were documented as a function of exposure level. Microscopy of the machined sections was performed to document the observed damage.

Two fire scenarios were modeled in high fidelity using CFD analysis to demonstrate the first step of the analysis procedure. These were a fuel fire in an engine nacelle and a 1 m diameter fuel spill fire under the wing of a fighter aircraft. An existing analytical method for predicting radiant heating from pool fires adjacent to an aircraft (no direct flame impingement) was identified and exercised to demonstrate pool fire distances and burn times that cause the experimentally observed composite delaminations in general. The time to delamination was estimated using the 1-D heat transfer model developed and calibrated to the materials of interest to predict the through-ply temperatures (and any pyrolysis). The nonlinear material heat transfer and thermogravimetric properties for this model were calibrated using test data for the three composites studied.

This report documents the experimental findings from the heat-exposed composites, the modeling and simulation of fires and material heat transfer/damage, and the status of the analysis tools to support the development of aircraft firefighting requirements. Both operational and technical recommendations are made based on the research results.

3. ASSUMPTIONS, METHODS, AND PROCEDURES

3.1. Summary

Heat-exposure testing was conducted with composite plates that were first conditioned in an oven at a temperature of 55 °C for four days, to remove moisture from the plates. They were then stored on desiccant. Some plates were then conditioned in a humidity chamber so that the effect of water content in the plates could be determined. Heat exposure tests were conducted at three different intensities of radiant heat fluxes with radiant heating from an infrared heater. Heat flux was monitored with heat flux sensors throughout the test. The large variation in matrix thermal performance necessitated different test conditions for each of the three different carbon fiber composite materials, so exposure times varied considerably between materials. Temperature throughout the plate thickness was monitored with embedded TCs, and visual and infrared video was taken of the exposed surface of the plate. After heat exposure, plates were cut into flexural, tensile and microscopy samples. Some microscopy samples were polished on their edges. Microscopy of sample edges was conducted to document the through-thickness damage in the plates. Mechanical test samples were then tested in four-point bending and in tension per ASTM standards. Testing was conducted on samples with and without heat exposure. The SI system of measurement was used throughout this report.

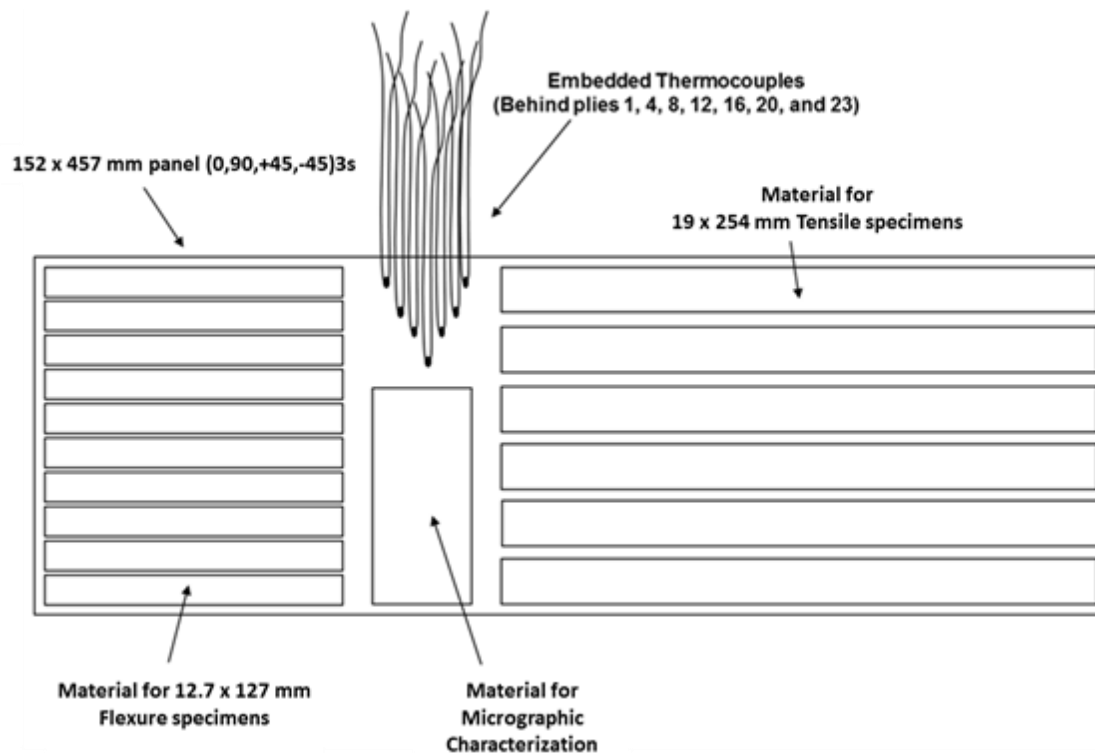
3.2. Test Facilities

All radiant heating tests were conducted at Tyndall AFB, FL in facilities controlled by the Air Force Research Laboratory (AFRL). Tensile and bending tests were performed using an MTS Model 244.31 test machine. Thermogravimetric analysis (TGA) was performed on a Netzsch STA 409 PC analyzer at the AFRL Fire Laboratory at Tyndall AFB and on a STA 449 F1 analyzer at Netzsch Instruments North America.

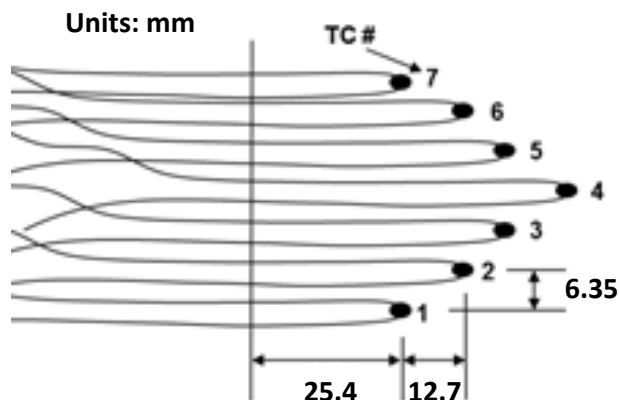
3.3. Materials

Materials were selected for this study as representative of a wide array of composites used in military aircraft. Three IM7 intermediate modulus carbon fiber (IM7) composites were evaluated; epoxy 977-3, modified (BMI) RM3002, and condensation polyimide AFR-PE-4. The three materials represent, theoretically, three levels of service temperature: epoxy 977-3 < 120 °C, RM3002 < 200 °C and AFR-PE-4 < 260 °C. In addition, they have, respectively, higher costs as the performance level increases and have evolved as high demands have been placed on aircraft weight and performance. Epoxy has been used the longest and represents the F-117A, B-2 generation of aircraft; the F-22 utilizes a hybrid of epoxy/BMI technology, and polyimides have been used more in recent composite applications.

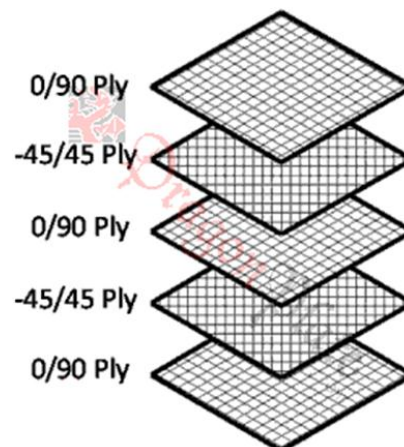
These three types of composite material plates were fabricated by AFRL/RXS at Hill AFB, UT for these heat exposure tests and are listed in Table 1. The test plates were manufactured in 152 × 457 mm (6 × 18-in) plates and trimmed to 140 × 445 mm (5.5 × 17.5 in) for testing. The plates were 24-ply quasi-isotropic layup of [0,90,45,-45]₃ s as shown in Figure 2. Ten plates of each type listed in Table 1 were manufactured.



EMBEDDED THERMOCOUPLES



LAYUP



Source: <http://www.dragonplate.com/>

Figure 2. Test Plate Layout

Nine of the test plates for each material system were fabricated with seven embedded 30-gauge, Type K TCs placed behind plies 1, 4, 8, 12, 16, 20 and 23. The objective of the embedded TCs was to measure the through thickness temperature profile during thermal exposure tests. The tenth plate, used to test the baseline properties of the materials before fire exposure, did not need TCs. The thickness of each composite type varied due to differences in the ply thickness of these material systems. Table 1 lists the average thickness for each material. The different thicknesses

affected the rate of temperature increase in each material for the same applied heat flux intensity. This difference was accounted for in the data analysis.

Table 1. Composite Materials

Resin (or equivalent)	Type	Cure °C	Dry T _g °C	Average Thickness (mm)
CYCOM 977-3	Epoxy	177	221	6.4
Renegade RM3002	Modified BMI	177	296	3.2
AFR-PE-4	Condensation polyimide	338	340	3.8
Fiber Volume Fraction: 60 percent				
Fiber type: Intermediate Modulus Carbon Fiber – IM7				

3.4. Procedures

3.4.1. Plate Heat Exposure

The composite plates were exposed on one side, for various periods of time, to three levels of heat flux: 15 kW/m², 25 kW/m², or 35 kW/m². Several experiments were conducted to verify that the composite plates would be exposed to uniform heat flux across the extent of the sample. These experiments led to the selection of an infrared heater, the design of the sample holder and insulation materials, and the determination of vertical and horizontal positioning of the sample underneath the heater. Heat flux was monitored with four heat flux gages at the corners of the plate support table, and one heat flux gauge in the center of the table.

The radiant heat source was a Process Thermal Dynamics model FS366-195A-20/3 infrared (IR) heater on a freestanding frame. The heat source had an effective heating area of 0.61 × 0.84 m and radiated downward from about 0.75 m above the floor, see Figure 3. The heater had a maximum output of 24.8 kW and a theoretical maximum heat flux of 48.4 kW/m².

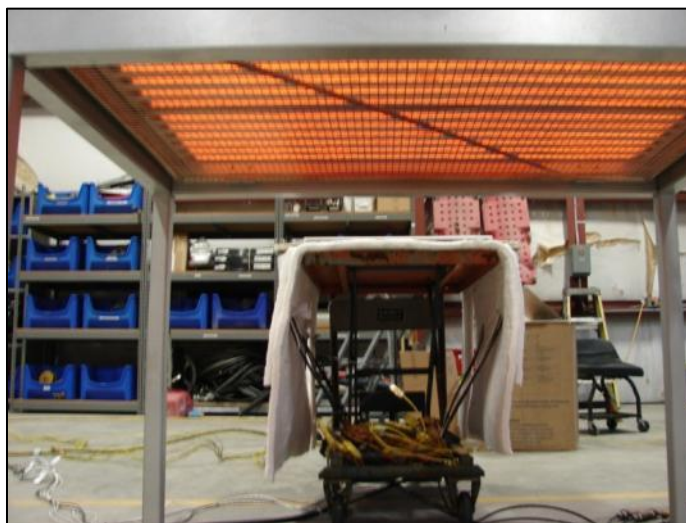


Figure 3. IR Heater Up to Temperature

Heater element temperature was controlled by a Watlow PM6C1FJ-AAAABAA temperature controller with type K TC feedback. A Control Concepts 1600-PM2 SCR power controller, a two-phase, time proportioning, zero-crossing high speed switch, linearly controlled power to the heating elements by varying the percentage of “on” time within the set duty cycle. The individual heating elements were connected in a delta configuration with the two SCR power controller outputs and the third, non-switched leg of the incoming power. This controlled the heater element temperature to a desired setpoint. Heater element temperatures corresponding to specific heat fluxes for this setup were determined experimentally and are shown in Table 2.

Table 2. Element Temperatures and Corresponding Heat Fluxes

Heater Element Temperature (°C)	Center Heat Flux (kW/m ²)
610	15
730	25
825	35

The heater from Process Thermal Dynamics was constructed from two separate heating element assemblies. When these two assemblies were combined, a gap was formed between the two inside heating elements that was larger than the gap between the other heating elements. This can be seen in Figure 3, the most prominent dark line running left-right in the middle of the glowing elements. Experimental procedures to test the setup with the composite plate centered under the combined heating elements resulted in non-uniform heat flux over the surface of the sample, likely due to the larger gap between the two inside heating elements. After experimenting with various plate locations and separation distances, it was determined that the most uniform heat flux in our range of interest, 15 to 35 kW/m², occurred at a separation distance of 13.7 cm, with the inside edge of the composite plate located 32 mm from the center of the support fixture and the center of the support fixture located 12.7 mm from the intersection of the two heaters, as shown in Figure 4. Furthermore, in this position the heat flux at the center of the fixture, where the center heat flux sensor was located, was the same as the heat flux at the middle of the composite plate.

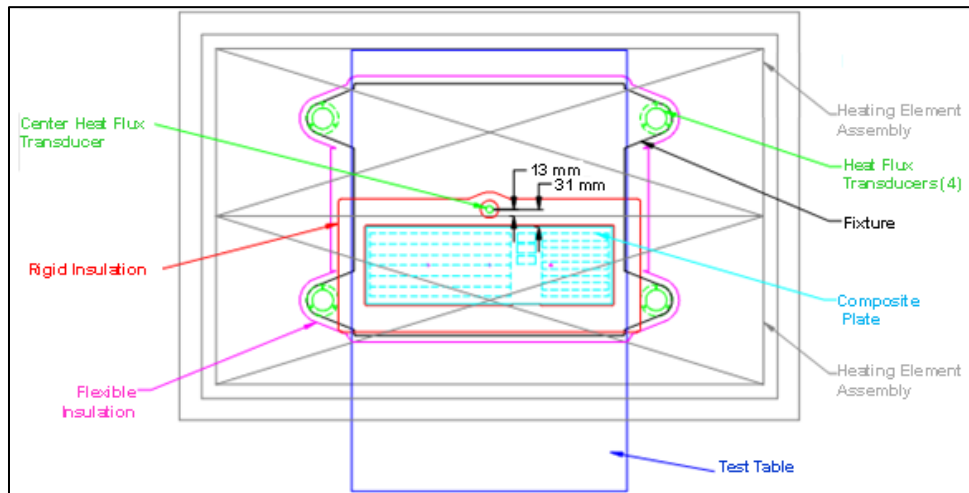


Figure 4. Top View Drawing of Heater Setup

The composite plate sample under test and associated instrumentation was positioned on a wheeled, height-adjustable table. The movable table allowed the composite to be rolled into position under the heater and then withdrawn after the desired exposure time. Figure 5 shows the test table in position under the heater. The heater remained in the same position from test to test. The lengths of the legs for the heater platform were set so that the platform was parallel to the inserted table. The height of the table was adjusted before each test to ensure the same separation distance between the heating elements and the composite plate under test. That separation distance was 13.7 ± 0.2 cm. It should also be noted that the table and heater were both level and that all four corners of the fixture (shown in Figure 4) shared the same separation distance measurement ± 0.2 cm.



Figure 5. Sample Table in Position under the Heater

The position of the table under the heater was kept constant test to test by visually aligning center marks on the table and heater during insertion and by use of a recessed expansion joint in the concrete floor that stopped the table at the same location under the heater each time.

Making up the base of the test table was a Dandy 250-kg capacity L-250 hydraulic lift table. The 0.8×0.5 m platform was draped with 12.7 mm flexible ceramic insulation. Centered on the far end was a rectangular sheet of 3.2 mm steel. This steel fixture had four holes near the corners to mount Medtherm 96-30T-30RP(Znse)-120-21746, Schmidt-Boelter type heat flux transducers. On top of the fixture, located at the center, another heat flux transducer, Medtherm GTW-7-32-485A Schmidt-Boelter type, was secured with magnetic strips. Three type K TC probes were equally spaced along the length where the composite plate was positioned and measured the backside temperature of the composite plate. A photo of this can be seen in Figure 6.

The fixture was covered in an additional layer of 12.7 mm flexible ceramic insulation with holes cut for the center and corner heat flux sensors and the three backside TCs, as shown in Figure 7. These TCs extended through the table insulation in order to be in contact with the composite plate once placed on the table. The composite plate was placed on top at a location determined to have the most uniform heat flux, as was discussed previously. The plate location was marked so placement was consistent from test to test. Tightly-fitted 6.4 mm flexible ceramic insulation was

placed all the way around the composite plate, to protect the edges of the plate from additional damage from the heat source. An additional 3.2 mm layer of rigid ceramic insulation was placed around the edges of the plate, with a cutout for the center heat flux sensor. Figure 8 shows a typical composite plate ready to be exposed by rolling the test table under the preheated IR heater.

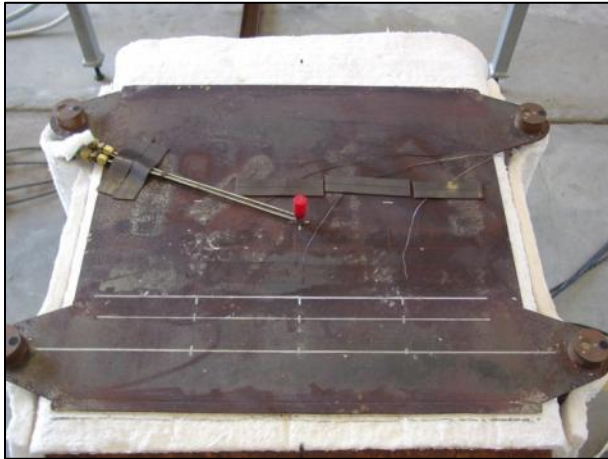


Figure 6. Test Table Fixture and Instrumentation



Figure 7. Base Test Table Insulation



Figure 8. R2 Composite Plate Ready to be Exposed

In addition to the five heat flux sensors and three TCs making up the test table, there were seven type K TCs embedded inside the composite test plates. National Instruments PXI/SCXI data acquisition hardware was used with LabVIEW software to record the data at 1 Hz. A video camera recorded each test and an IR video camera, FLIR Systems model SC 620, was used to record some of the tests.

A typical experiment consisted of the following steps:

1. Measure the weight of the composite plate, including TC wires.
2. Place spacer insulation, if needed, as shown in Figure 9. IM7/977-3 plates were much thicker than both IM7/AFR-PE-4 and IM7/RM3002. IM7/AFR-PE-4 and IM7/RM3002 plates required spacer plates made up of rigid insulation so that the distance from the heater elements to the surface of the plates was kept constant.

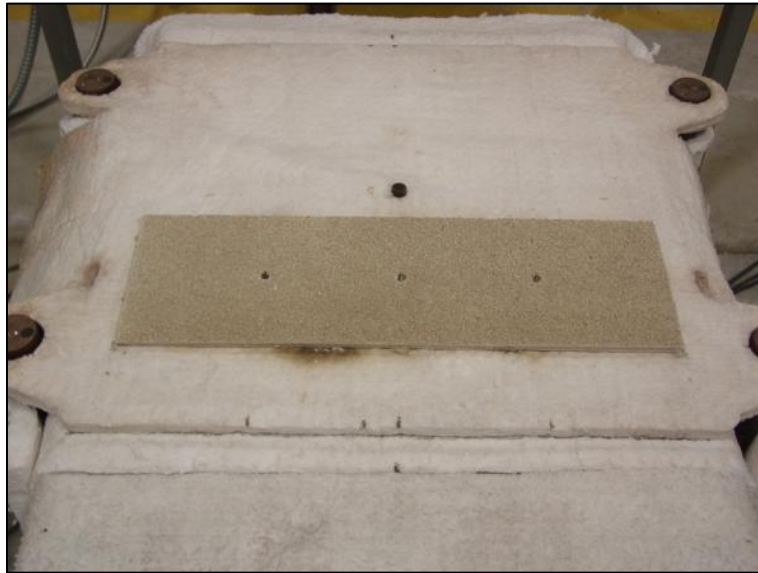


Figure 9. Spacer Insulation for an IM7/AFR-PE-4 Test

3. Check backside TCs (3) for proper orientation. They should be pointed up, just past the surface of the bottom insulation. Should be able to push straight down with light finger pressure.
4. Position composite sample on top of the backside TCs.
5. Tightly pack 6.4 mm flexible ceramic insulation all around the edges of the plate (Figure 10).



Figure 10. Plate A8 with Edge Insulation

6. Place 3.2 mm rigid ceramic insulation over the edge insulation making sure gaps around the sides are evenly spaced.
7. Cover the embedded TC wires with 12.7 mm flexible ceramic insulation.
8. Temporarily insert the test table under the heater and set table height to achieve 137 mm separation distance between composite plate and heating elements.
9. Remove test table from under heater.
10. Set the heater temperature controller to the temperature indicated in Table 2 to achieve the desired heat flux.
11. Turn the heater on.
12. Insert a surrogate table under the heater (Figure 11) set to the same separation distance and with similar physical characteristics (size, insulation type, thickness, etc.) to the actual test table. This allows the heater to come to equilibrium with something similar to the test table, without preheating the composite plate.



Figure 11. Test Table Ready; Surrogate Table under Heater During Preheat

13. Turn on the heat flux transducer cooling water.
14. Allow the heater to ramp up in temperature and preheat.
15. Once steady state has been reached at the desired temperature set point, the test can begin.
16. Start the data acquisition system.
17. Remove the surrogate table while at the same time inserting the test table under the heater.
18. Expose the composite plate for the desired amount of time, or until a specific internal temperature or damage has occurred.
19. Remove test table from under heater.
20. Immediately turn on a cooling fan directed horizontally across the top surface of the composite plate to mitigate any additional composite damage, while at the same time removing latent heat through the original damage path, through the top.
21. Turn off the heater.
22. Stop data acquisition system once all embedded TC readings are below 170 °C (338 °F).
23. Continue with fan cooling until composite plate can be safely handled.

24. Turn off cooling fan.
25. Turn off the heat flux transducer cooling water.
26. Remove composite plate from test table.
27. Measure the weight of the composite plate, including TC wires to determine mass loss during testing.

3.4.2. Moisture Content

Composite plates were tested in both dry and wet conditions in order to determine if there was an effect of moisture content on the thermal-damage response.

After manufacture, plates were stored at room temperature and relative humidity (approximately 50 percent). Before testing, plates were dried in a laboratory oven (Mettler UFE 500, with air circulation set to 50 percent) at 54.5 °C (130.1 °F) for 96 hours. The plates were weighed periodically to measure moisture loss and it was determined that moisture loss was negligible after 96 hours in the oven. The plates were then stored in a humidity controlled (25 percent) chamber with silica gel desiccant at room temperature until testing commenced.

Three plates, one of each material type, were first dried and then conditioned in a humidity chamber for 163 days at 95 percent relative humidity and 35 °C (95 °F). This condition was chosen as a typical environment for an aircraft while on the tarmac of, for example, Tyndall AFB. Use of higher temperatures to accelerate moisture uptake were not used in order to minimize risk of chemical damage to the material.

Mass gain for the conditioned plates is shown in Figure 12. Note the significantly higher diffusivity and final moisture content of the material with the AFR-PE-4 resin. This may be in part due to the large void content seen in this material (Section 5.1). Plate A9 appears to be close to the saturated moisture content at the time of testing where the other plates are not since these plates still show a linear dependence in moisture uptake with the square root of time [5].

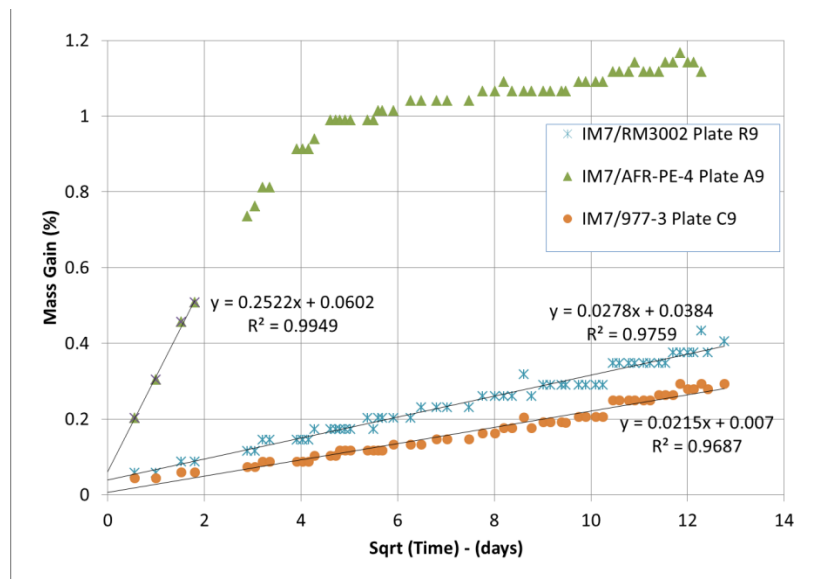


Figure 12. Mass Gain for Three Material Plates Conditioned in a Humidity Chamber at 95 Percent Relative Humidity at 35 °C

3.4.3. Post-Fire Exposure Mechanical and Physical Testing

After exposure to radiant heat each panel was cut into nine bend specimens, three microscopy specimens, and six tensile specimens using a water jet. Dimensions and locations for the cut-outs can be seen in Figure 13.

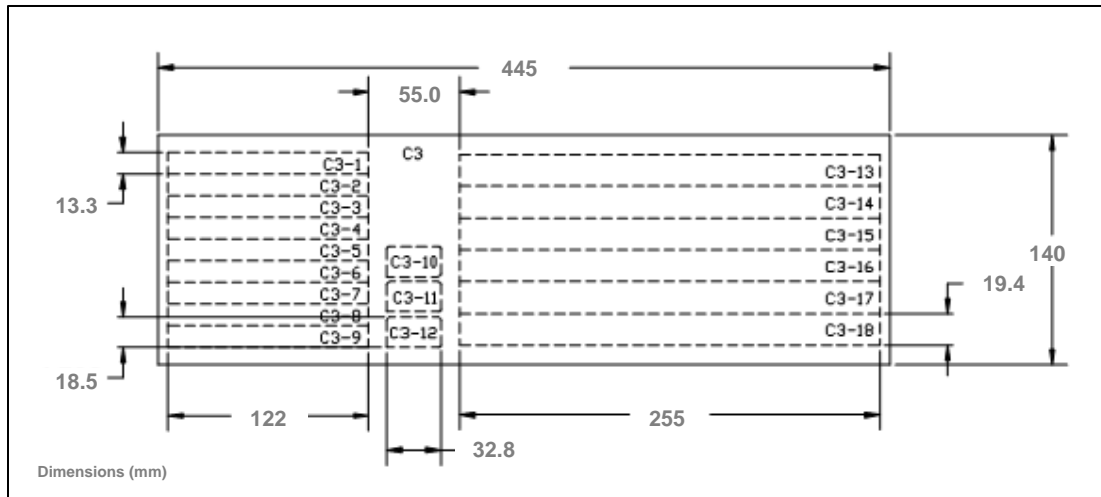


Figure 13. Typical Panel Cut-Outs

The dimensions indicated in Figure 13 are not the final dimensions of the specimens, merely the cut path for the CNC controlled water jet. The typical high pressure water and garnet flow path of the water jet cutting machine is 1.07 mm wide. The 1.07 mm of material removed in the cut path is known as kerf and is non-recoverable. This kerf width varies slightly with the condition of the orifice used in the machine, and therefore the size of the samples will vary as well. Typical final sample sizes were: 12.2×120.7 mm flexure/compression (bend) specimens, 31.8×17.5 mm microscopy specimens, and 18.3×254 mm tensile specimens.

It was intended to cut samples far enough from the edges of the panels to avoid any edge effects of the heat exposure in the final sample coupons. The unused material along the edges also allowed for any needed angular alignment of the long axis of the cut outs with the material fiber direction. This ensured that the long axes of the samples were always aligned with the fiber direction.

The specimens were numbered, as indicated in Figure 13, as they were cut and then removed from the water jet. The first letter of the sample number indicated the material: C for IM7/977-3, R for IM7/RM3002, and A for IM7/AFR-PE-4. The second number of the sample number signified the panel number (1-9) from which the samples were cut. The number after the dash identified the specific location from which the samples were cut from the panel.

Bend specimens (1-9) were ready for mechanical testing immediately after water jet cutting, as were microscopy specimens (10-12). However, tensile specimens (13-18) were tabbed before mechanical testing. A total of nine bend specimens and six tensile specimens were cut from each plate.

The portion of material with embedded TCs, the region below the TCs in Figure 2, was used to characterize the thermal damage to the plate. The material was sectioned and used for micrographic inspection to determine the depths of the char layers and extent of delamination that occurred.

3.4.3.1. Polishing Procedure

Three microscopy samples measuring 31.8×17.5 mm were cut from each composite plate. An optical microscope (Celestron Model 44302) was used to image the two long (31.8 mm) edges of each microscopy sample. A series of photographs were taken along the long edge at 1x and 40x magnification. These images were taken stepwise so that a composite of the photographs would reproduce the entire edge surface. In addition, the center of each long edge of each sample was photographed at 150x. Selected samples were then embedded in epoxy, polished and re-photographed using the above method in order to obtain more surface detail. The polishing procedure was as follows:

- Two plastic support clips (Buehler SamplKlip I 20-4100-100) were placed on each sample in order to maintain the sample in an upright position.
- The sample was placed in a plastic cup (Buehler 1.2"-inside diameter SamplKup 20-9181), with the side to be polished face-down in the cup.
- An epoxy mixture (7.60 g Buehler EpoThin Epoxy Resin 648-501286 and 2.97 g Buehler EpoThin Epoxy Hardner 684-501278) was poured into the cup.
- The resin was allowed to cure for 24 h. After curing, the sample, now embedded in epoxy, was removed from the cup.
- The sample was then sanded with P220 sand paper using a rotary grinder (South Bay Technology Grinder/Polisher Model 900, see Figure 14) set to 200 rpm, until approximately 3 mm of material had been abraded.



Figure 14. Rotary Grinder/Polisher used to Prepare Samples

- The sample was rinsed with water to remove any grit and abraded material.
- The sample was then polished with a silicon carbide grinding pad (Buehler CarbiMet 2 320/P400 abrasive paper 30-5118-320-102) and water using a rotary grinder set to 200 rpm for 3 min.
- The sample was rinsed with water to remove any grit and abraded material.

- The sample was then polished with a silicon carbide grinding pad (Buehler CarbiMet 2 600/P1200 abrasive paper 30-5118-600-102) and water using a rotary grinder set to 200 rpm for 3 min.
- The sample was rinsed with water to remove any grit and abraded material.
- The sample was then polished with a polishing pad (Buehler Texmet C 40-1108) and diamond suspension solution (Buehler MetaDi 3.0 μm diamond suspension 40-6631) using a rotary grinder set to 120 rpm for 5 min.
- The sample was rinsed with water to remove any grit and abraded material.
- The sample was then polished with a polishing pad (Buehler MicroCloth 40-7218) and diamond suspension solution (Buehler MasterPrep 0.05 μm suspension 63-6377-006) using a rotary grinder set to 120 rpm for 5 min.
- The sample was rinsed with water to remove any grit and abraded material.
- The sample was then dried and ready for imaging as shown in Figure 15.

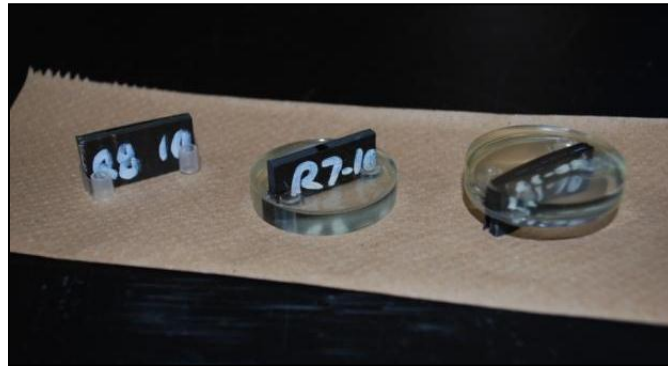


Figure 15. Unpolished Sample with Attached Samplklips (left), Polished Sample with Polished Face Down (,iddle), and Polished Sample with Polished Face Up (right)

3.4.3.2. Tabbing Procedure

Tensile test samples were attached to fiberglass tabs to facilitate tensile testing according to the following procedure.

Tab Material:

Rectangular cutouts measuring 187×76 mm were cut from $1.2 \text{ m} \times 1.2 \text{ m} \times 3.2 \text{ mm}$ FR-4 glass epoxy laminate fiberglass stock material and used as tab material. The cutouts were made such that the sides of each cutout were oriented 45 degrees with respect to the fibers in the stock material. One face of each tab (the face to be attached to the tensile samples) was prepared according to the following procedure:

- The fiberglass tab was hand sanded with P220 sand paper for 4 min.
- The tab was washed with water to remove any grit or abraded material.
- The tab was then hand buffed with an abrasive pad (Merit Abrasotex Abrasive Hand Pad) for 4 min.
- The tab was then washed with water to remove any grit or abraded material.
- The tab was then placed in an oven set to 54.5°C for 15 min to dry the samples.

- The tab was then wiped with a paper towel soaked in acetone (Aldrich 99.5 percent American Chemical Society (A.C.S.) Reagent Grade Acetone) to remove any organic residue material such as oil from the preparer's hands.

Tensile Test Samples:

Six tensile tests samples measuring 254×19.4 mm were cut from each composite plate. Both faces of the 76 mm length at both ends of the samples (the four regions of the sample to be attached to the fiberglass tabs) were prepared according to the following procedure:

- The sample was hand sanded with P220 sand paper. Sanding was only performed parallel to the length of the samples, because it was observed that sanding perpendicular to the length of the sample caused excessive abrasion to the corners of the sample. In general, each 76 mm length was sanded for 2 min. However some of the materials, especially samples that had been exposed to considerable heat, were noted to be softer and abrade more rapidly. Those samples were sanded for less time, until the preparer believed that sufficient abrasion had occurred.
- The sample was then washed with water to remove any grit or abraded material.
- The sample was hand buffed with an abrasive pad (Merit Abrasotex Abrasive Hand Pad) for 2 min.
- The sample was washed with water to remove any grit or abraded material.
- The sample was then placed in an oven set to 54.5°C for 15 min to dry the samples.
- The sample was wiped with a paper towel soaked in acetone (Aldrich 99.5 percent A.C.S. Reagent Grade Acetone) to remove any organic residue material such as oil from the preparer's hands.

Tabbing Procedure:

A stainless steel frame was custom built to facilitate attaching the composite samples to the fiberglass tabs. This frame held four fiberglass tabs and up to six composite samples (see Figure 16). The tabbing procedure was as follows:

- A non-stick spray (Dow Corning Molykote 316 Silicon Release Spray) was applied to the top and bottom faces of the steel frame.
- Two fiberglass tabs were placed on the bottom portion of the steel frame.
- Up to six composite test samples were placed on top of the fiberglass tabs. Three samples are shown in Figure 16.
- Epoxy resin (Armstrong A-12 Epoxy Resin) was applied to the top two prepared surfaces of each composite sample.
- The composite sample was then flipped over, so that the epoxy was in contact with the bottom tabs.
- Epoxy resin (Armstrong A-12 Epoxy Resin) was applied to the top two prepared surfaces of each composite sample. See Figure 16.
- Two additional fiberglass tabs were then placed on top of the composite strips. See Figure 17.

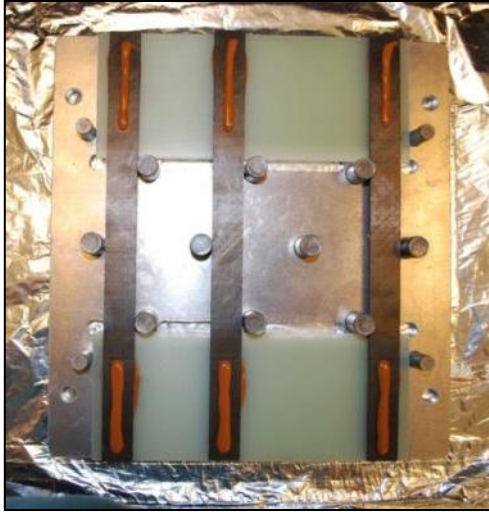


Figure 16. Epoxy Applied to the Top and Bottom of the Composite Samples

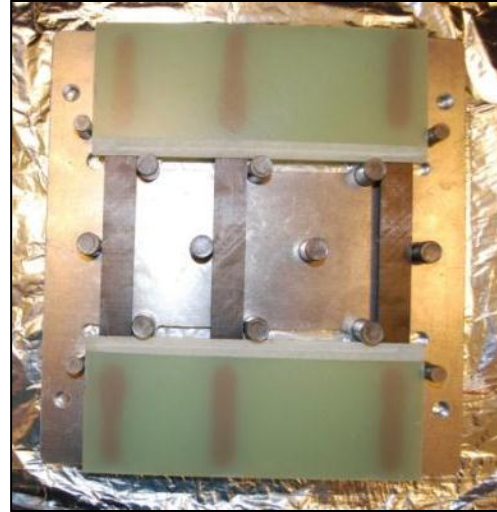


Figure 17. The Tabbing Procedure after Placing the Top Fiberglass Tabs

- The upper portion of the steel frame was then placed on top of the fiberglass tabs.
- A weight was positioned on top of the steel frame to press the apparatus together and insure proper contact between all surfaces. A weight massing 3.8 kg per composite test sample was chosen, totaling 22.7 kg if the maximum of six samples were being prepared.
- The epoxy was allowed to cure for 24 h. The fiberglass tabs and composite samples, now glued together, were then removed from the steel frame.
- The tab/sample structure was wiped with a paper towel to remove any remaining silicon spray residue.
- The tab/sample structure was then cut into approximately 25 mm wide strips using an industrial band saw to create the tabbed samples ready for testing. See Figure 18 for a photo of a finished sample.



Figure 18. A Tabbed Composite Sample

3.4.3.3. Tensile Tests

Tensile modulus of elasticity and ultimate tensile strength were determined from tension tests performed according to ASTM standard D3039 [6]. Strain was recorded on each side of the specimen. This “back-to-back” strain was measured using an electrical resistance strain gage in

the front, unexposed side of the specimen, and an extensometer (MTS model 632.11E-20) in the back, exposed side. Micro Measurements strain gages EA-06-250AE-350 were used for all strain gage measurements. A schematic of the tensile specimens is shown in Figure 19, which depicts the placement of the strain gage and extensometer.

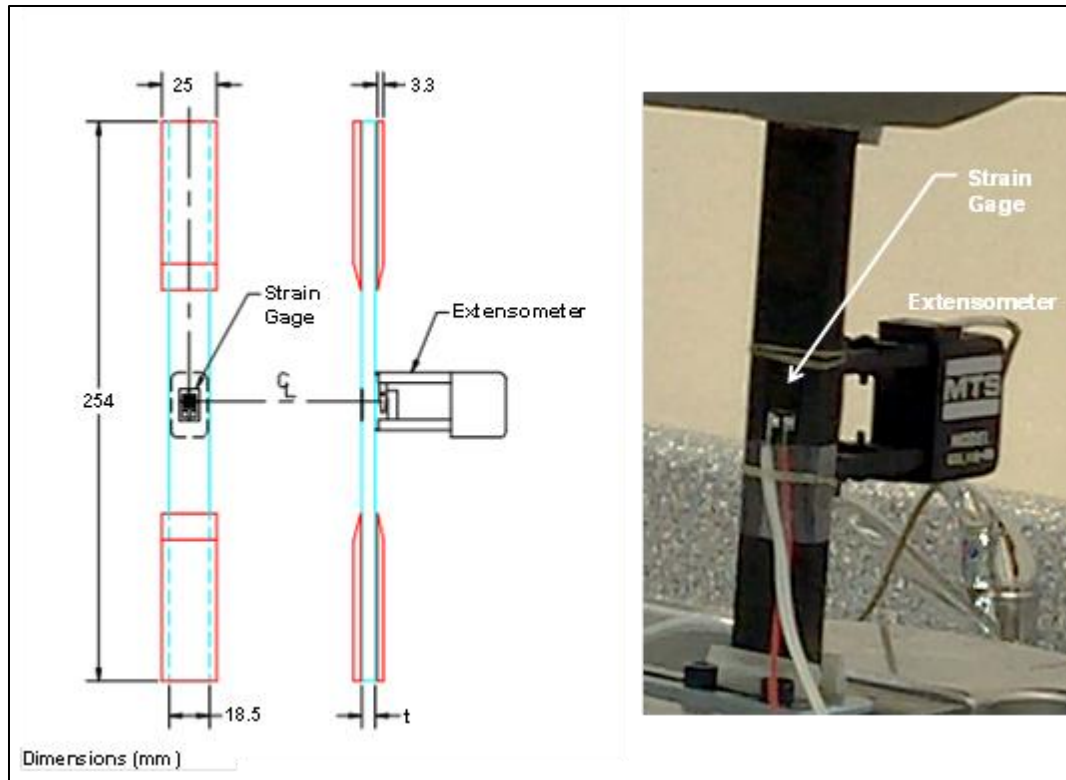


Figure 19. Strain Measurements of Tensile Specimens

Specimens were mounted in an MTS servo-hydraulic test machine and pulled to complete failure. The MTS 647 hydraulic wedge was fitted with MTS 418418-02 (6.1 - 17.0 mm (0.24 - 0.67-in) serrated grips and operated at 8.62 MPa to clamp the specimen without slipping. It was determined that higher clamping forces created excessive strain concentrations in the tab area and lead to premature failures. Tests were performed using a constant displacement rate of 1.3 mm/min. Strain was measured directly from the strain gage in front and the extensometer in back (thermally damaged side). Because the extensometer would typically jump from its zeroed position mid-test as a consequence of locally failing fibers, front and back strain were averaged only for low strain, modulus and percent bending, calculations. All other calculations rely solely on the strain gage for strain measurements. Figure 20 shows the back extensometer “jumping” three times during the test at mid- to high strains. Stress was calculated by dividing the tension force by the nominal cross-sectional area of the specimen.

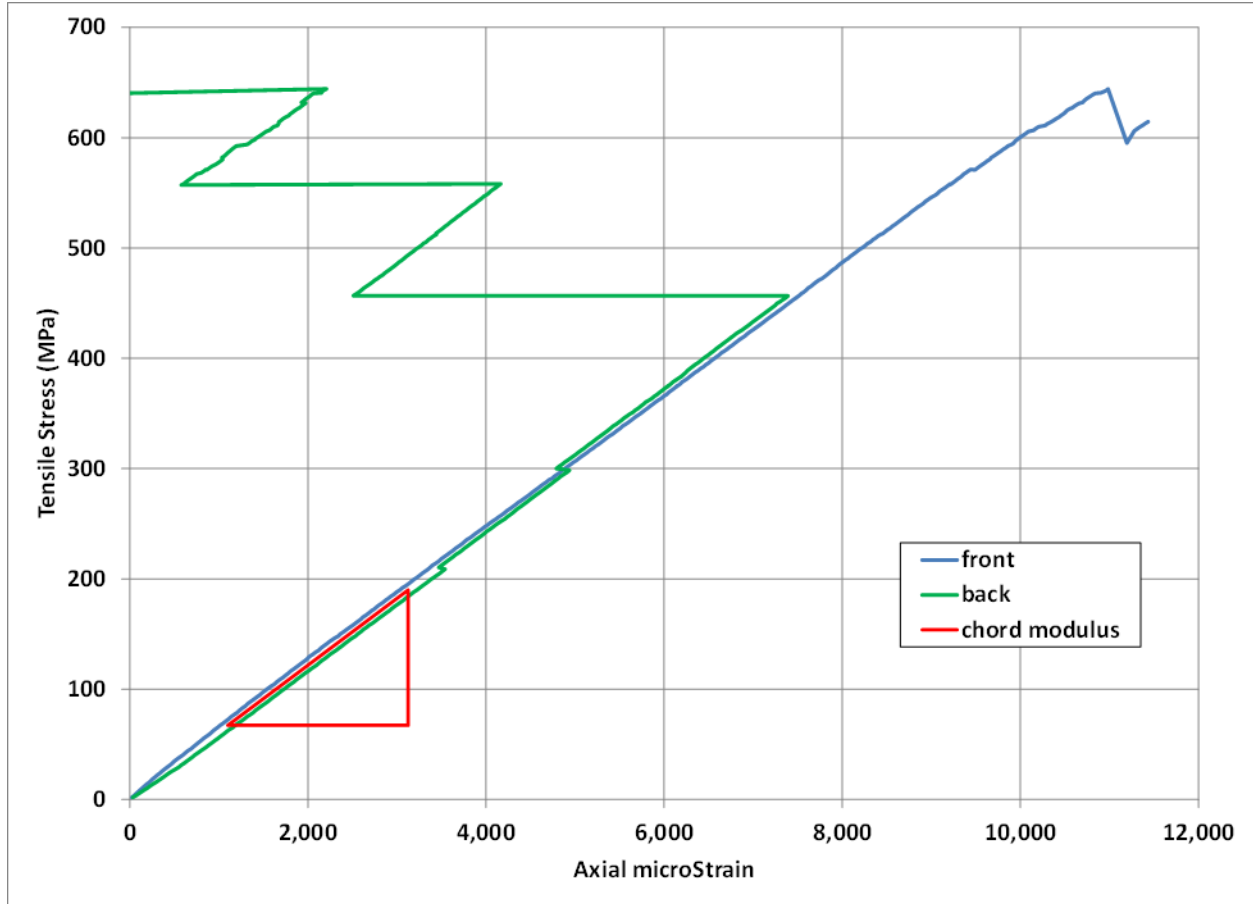


Figure 20. Typical Stress Strain Results

Ultimate tensile strength was defined as the maximum tension divided by the nominal cross-sectional area. Ultimate tensile strain was taken as the corresponding front strain. The tensile chord modulus of elasticity values were calculated from the initial slope of the linear portion of the stress-strain curve, defined in the standard to be between 1000 and 3000 micro strain ($\mu\epsilon$). In most cases the average of front and back strain was used in this region to define chord modulus. If the extensometer jumped or otherwise behaved erratically within this region, only front strain was used to calculate the chord modulus.

Since back-to-back axial transducers were used for all tests, specimen bending was calculated for all tests using the equation below. As per the ASTM, standard percent bending is to be calculated mid-range of the cord modulus strain range, using data points recorded near 2000 $\mu\epsilon$.

$$\text{Percent Bending} = \frac{|\epsilon_f - \epsilon_b|}{|\epsilon_f + \epsilon_b|}$$

Where:

ϵ_f = indicated strain from front transducer, $\mu\epsilon$;

ϵ_b = indicated strain from back transducer, $\mu\epsilon$.

Poor system alignment can cause premature specimen failure and property data scatter. To prevent this, grip alignment was checked before each series of tests with an alignment coupon. A rectangular alignment coupon was fabricated from $25.4 \times 254 \times 6.4$ mm 6061 aluminum by mounting two stacked rosette strain gages (Omega KFG-5-120-D16-11L3M3S) centered on each side. The two closely positioned gage grids are aligned to measure axial and transverse strains. An alignment check was performed with the same coupon inserted in each of the four possible installation permutations by gripping, slowly loading to 17,792 N (4,000 lbf), holding for 10 s, slowly releasing tension, then releasing the grip. The strain response was monitored and percent bending calculated in both the axial and transverse directions. If percent bending ever exceeded three percent at the full load of 17,792 N (this corresponds to a moderate strain of $1600 \mu\epsilon$ for this alignment coupon) then the grips were readjusted and checked again. The ASTM standard states that good testing practice is generally able to limit percent bending to a range of three to five percent at moderate strain levels.

3.4.3.4. Bend Tests

Flexural properties were determined from four point bend tests performed according to ASTM D 6272 [7]. As per the standard, a specimen of rectangular cross section rests on two supports and is loaded at two points, each an equal distance from the adjacent support point. The distance between the loading noses (the load span) is one third of the support span. The specimen is deflected until rupture occurs.

Two sets of loading noses and supports were fabricated. One set was used with the IM7/977-3 samples and the other set for both the IM7/AFR-PE-4 and IM7/RM3002 samples, because their thicknesses were similar and their resulting support span to depth ratios were similar. The bend fixture for AFRPE and RM3002 samples can be seen in Figure 21.

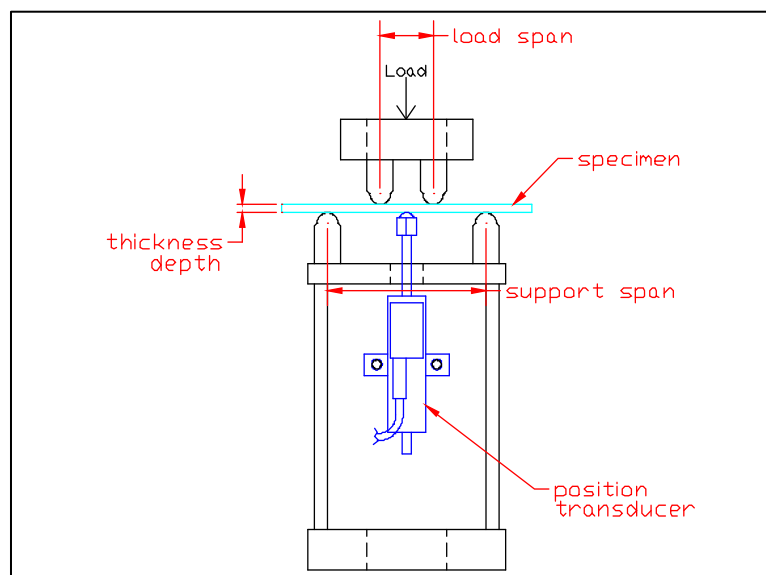


Figure 21. Small Bend Fixture

Primary dimensions for the loading noses and supports, as well as other relevant data, can be found in Table 3.

Table 3. Bend Test Information

Material Resin	Nominal Thickness (mm)	Support Span (mm)	Load Span (mm)	Nose Radii (mm)	Support Span to Depth Ratio	Minimum Specimen Length (mm)	Crosshead Rate (mm/min)	Maximum Deflection (mm)
977-3	6.4	95.3	31.8	9.0	15.0:1	114.3	2.6	15.0
RM3002	3.2	76.2	25.4	5.0	23.6:1	91.4	3.3	18.9
AFR-PE-4	3.8	76.2	25.4	5.0	20.0:1	91.4	2.8	16.0

Specimens were tested in the MTS servo-hydraulic machine. A Novotechnik TR25 position transducer was used to measure the deflection of the beam at the common center of the support span. Tests were performed using a constant displacement rate indicated in Table 3 for the specific material. Maximum stress in the outer fibers occurred between the two central loading points that define the load span. This stress may be calculated for any point on the load-deflection curve for relatively small deflections by the following equation:

$$S = PL/bd^2$$

Where:

S = stress in the outer fibers throughout the load span (MPa);

P = load at a given point on the load-deflection curve (N);

L = support span (mm);

b = width of specimen (mm);

d = thickness of specimen (mm).

The maximum strain in the outer fibers also occurs at mid-span, and it may be calculated as follows:

$$r = 4.7Dd/L^2$$

Where:

r = strain in the outer fibers (mm/mm);

D = deflection of the center of the specimen (mm);

L = support span (mm);

d = thickness of specimen (mm).

During testing as the specimen is slowly deflected, its resistance is measured as applied load. The outer fiber stress in Figure 22 is proportional to applied load. Applied load increases until some point of specimen failure, at which time the load suddenly drops. Bend tests were stopped after the first significant (greater than approximately 10 percent) drop in applied load. This greater than 10 percent load drop occurs in Figure 22 at ~750 MPa after three smaller load drops that were less than 10 percent. Because continued testing could have eventually resulted in an even higher load and increased flexural strength, this first peak in the stress strain curve will be referred to as simply flexural strength and not ultimate flexural strength. Flexural strength is

calculated from the above stress equation with P equal to the maximum load recorded. Flexural strain is the corresponding calculated strain.

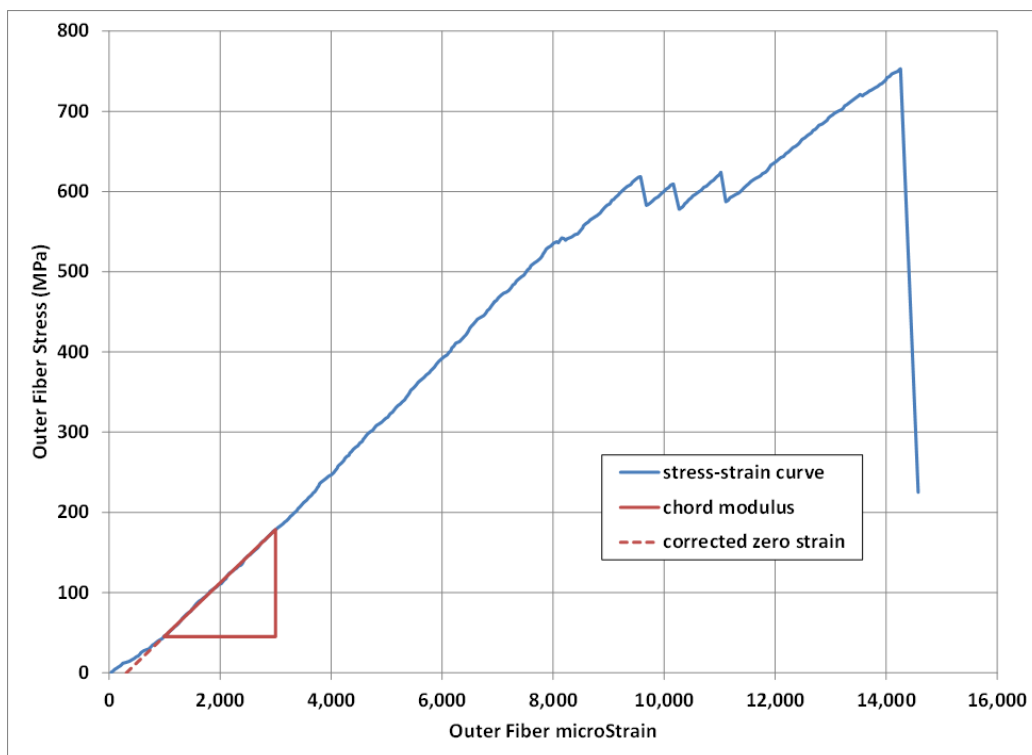


Figure 22. Typical Bend Results

The chord modulus of elasticity values were calculated from the initial slope of the linear portion of the stress-strain curve. In most cases, the linear region of the stress-strain curve was defined as being between 1000 $\mu\epsilon$ and 3000 $\mu\epsilon$. In tests with a larger toe region the linear region was increased in 500 $\mu\epsilon$ increments to get to the linear portion of the curve.

In a typical flexural stress-strain curve there is a nonlinear toe region at the beginning that does not represent a property of the material. It is an artifact caused by the take up of slack and seating of the specimen. In order to obtain correct values for such parameters as strain, strength, and modulus, this artifact must be compensated for to give the correct zero point on the strain axis. In this case the materials exhibited a region of Hookean (linear) behavior, and a continuation of the linear region of the curve is constructed through the zero stress axis. This intersection is the corrected zero strain point from which all extensions or strains were measured.

4. MODELING AND SIMULATION

4.1. Analysis Methodology

The analysis methodology developed consists of four primary steps shown in Figure 1: (1) model a fire event to obtain the thermal loading on a given composite structure, (2) model heat transfer and pyrolysis in the composite material, (3) evaluate damage to the material as a function of time, (4) determine response times to limit damage to acceptable levels. This methodology is supported by heat exposure and mechanical testing of the materials of interest to develop the modeling parameters needed.

In the first step of the analysis method a CFD solver, ANSYS FLUENT, is used to predict the transient flow and heating environment on a portion of the aircraft composite structure some distance from the fire source. Modeling of two fire scenarios are presented in this report. In Step 2, the heating environment predicted by the CFD model is applied to a 1-D FE heat transfer model. This model was further developed under this effort and predicts the transient through-thickness temperature change and degree of pyrolysis in the composite at different locations on the structure.

Finally, a modeling method was developed to predict the mechanical degradation of a composite based on the output from the heat transfer and pyrolysis analysis. This approach provides general predictions on the reduction in mechanical strength and stiffness of composite structures by providing predicted reductions in the tensile, flexural and compressive strength and stiffness in terms of their so-called in-plane and flexural ‘Engineering Constants’ based on the degree of pyrolysis through the thickness. As will be described in the following section, however, the composite plates tested in this effort experienced sudden and catastrophic delaminations prior to any significant charring. There was not significant damage from pyrolysis for the test conditions, so the code for this model was not completed.

There are at present no models that can predict the thermally-induced delaminations seen in the experiments. Therefore, prediction of the mechanical degradation of the material as a function of time cannot currently be performed with the desired accuracy.

In the following sections, the models developed to support the three steps in this analysis process are described in more detail.

4.2. Aircraft Fire Model

Aircraft fire modeling was accomplished using the CFD Program ANSYS FLUENT operating at DoD High Performance Computing Modernization Office, Major Shared Resource Centers at ERDC and AFRL.

4.2.1. Fire Scenarios

Fire scenarios were defined based on the historically frequent fire types experienced by Air Force fire fighters during normal flight operations. There were four specific incident types considered and two events were modeled:

- a. Engine Nacelle Fire – occurs when a fuel or hydraulic line leaks within the nacelle and is ignited by contact with a hot surface.
- b. Spill Fire – occurs when spilled fuel pools on the ground near or under the aircraft and ignites.
- c. Wet Starts Fire - occurs on engine start, when fuel pumped to the engine fails to ignite in the combustor but ignites in the exhaust section. Historically these events are common but readily extinguished with flight line fire extinguishers and result in minimal damage to the aircraft (not modeled in this effort).
- d. Auxiliary Power Unit (APU) Fire - occurs when a fuel or hydraulic line leaks within the APU compartment and is ignited by contact with a hot surface (not modeled in this effort).

Catastrophic fires such as disk failures or ground collisions are also not considered in this report as the presumed level of damage exceed that of a Class B mishap before fire damage occurs.

The F-22 was chosen as the aircraft for fire modeling. The most important part of developing a realistic CFD model of real world effects is obtaining an accurate design specification of the components modeled. This proved to be difficult since no single organization holds all of the required data. In the case of the F-22 aircraft engine and surrounding structures, the engine drawings are owned by Pratt & Whitney, the engine nacelle design is owned by Boeing, and the integration drawings are owned by Lockheed Martin. None of these companies had any obligation to provide any information for this effort. At the request of AFRL/RXQ, the F-22 System Program Office (SPO) was able to arrange a teleconference with appropriate engineering staff. The companies and the SPO were eventually able to provide reasonably detailed models of the engine and wing fire zones. Details were not obtained of the APU area of the aircraft.

CFD combustion models typically require multiple features including multi-scale turbulent flow mixing, interacting chemical kinetic combustion processes, radiation heat transfer effects, and soot production [8, 9]. Multiple physical sub-models were solved simultaneously using ANSYS FLUENT to approximate these calculations. This software's compatibility within a multi-physics environment and support for complex mesh topologies reinforced the choice of this application over alternatives.

There are many models for jet fuel combustion published in the literature and one is built-in the ANSYS FLUENT non-premixed combustion model. This model is described in detail in the ANSYS FLUENT Theory Guide [10]. For the past several years the Air Force Office of Scientific Research (AFOSR) has been sponsoring an international consortium of universities and the National Institute of Standards and Technology (NIST) in developing an optimum model for computing jet fuel combustion. This model is JetSurF Version 2.0 – a working model for the combustion of n-alkane up to n-dodecane, cyclohexane, and mono-alkylated cyclohexane up to n-butyl-cyclohexane [11]. This model was used for calculation in this report. Table 4 summarizes the computational methodology implemented with each physical sub-model for both fire scenarios.

Table 4. Summary of the Computational Modeling Parameters

Physical Sub-Model	Physical Sub-Model Description
3-D Navier Stokes	Conservation Equations of Fluid Motion
Non-Premixed Combustion	Chemical Reaction Kinetics
Realizable k- ϵ	Turbulence
Discrete Ordinates (DO)	Radiation Heat Transfer
JetSurF Version 2.0	Jet Fuel Model

4.2.1.1. Engine Nacelle Model

The fire scenario in the engine nacelle compartment of the F-22 consisted of a JP-8 fuel spill from a broken, pressurized fuel line. The fuel flow rate from the fuel line into the compartment was set to 0.091 Kg/s or about 1.8 gal/min at a location on the bottom of the F-119 engine. The fuel ignition occurs from contact with a hot surface.

Design sketches of the structural components that make up the engine nacelle area were part of the information provided by the SPO. The engine nacelle area is partially constructed of BMI or IM7/5250 composite wall plates which are similar to the RM-3002 plates that were evaluated in this test program. This material is located mostly on the top surface of the nacelle compartment with smaller quantities of materials on the lower portion of the compartment. From information provided, the side walls do not appear to be constructed using composite materials. In addition to information provided by the SPO, details of the aircraft engine and nacelle areas were obtained from TO 00-105E-9 [12] and from information on manufacturers' web sites.

More details of the model development and implementation are found in Section 5.5.1.

4.2.1.2. Spill Fire Model

The second fire scenario was a fuel spill under the wing of an F-22. This fire scenario assumes a 0.025 kg/s (0.5 gal/min) fuel flow from the aircraft fuel system onto the ground below. This spill results in a 1-m (3.3-ft) diameter ground fuel spill that ignites. The fuel spill is located half way between the landing gear and the wing tip. The model included a cross wind speed of 1 m/s (3.3 ft/s) from the wing tip toward the fuselage across the fire area.

Information needed to model the airplane materials and dimensions were obtained from TO 00-105E-9 [12] and from information on manufacturers' web sites. The F-22 under-wing area mostly consists of BMI or IM7/5250 which are similar to the RM-3002 plates that were evaluated in this test program. More details of the model development and implementation are found in Section 5.5.3.

4.2.1.3. Spill Fire Adjacent to Aircraft Analysis

Due to the rapid, severe damage from direct flame impingement on composite aircraft surfaces, in addition to the spill fire model, an additional analysis described in Section 5.5.5 summarizes the expected damage from small fuel spill fires adjacent to the aircraft based on material properties data gathered during this effort.

4.3. 1-D Heat Transfer Model with Pyrolysis and Thermal Damage

4.3.1. Background

The primary form of observed damage to polymeric composites exposed to fire is pyrolysis of the resin [e.g. 13-17]. The ability to predict the initiation of pyrolysis and char growth through the thickness of a composite exposed to external heating is therefore needed to predict tolerable exposures due to fires. Unfortunately, most commercial heat transfer solvers do not model the decomposition of material at elevated temperatures. There are, however, well documented approaches for modeling char development and material decomposition due to heating. A common approach is the implementation of a rate-dependent Arrhenius model of decomposition [18]. Several special purpose codes have been developed to predict heat transfer mechanisms that include an Arrhenius decomposition model, including one developed by Applied Research Associates [19]. The previously developed code was adapted to model the test conditions of this specific project through model improvements and updated properties for the specific material systems considered.

With uniform heating to a composite plate and negligible edge effects, a 1-D analysis of the heat transfer through the thickness is appropriate. Even with a discrete area of uniform heating, if the area is sufficiently large, the edge effects have been shown to have minimal effect in the heated region [19]. For this reason, most of the codes that consider pyrolysis, including the one used in this study, are simplified as one-dimensional. To analyze structures in more detail with strong gradients of heat flux across the surface, the thermal damage model developed in this project would need to be integrated into an existing computational three-dimensional heat transfer code. This is recommended to improve the accuracy of results in general application.

In the following subsections, an overview of the existing code and its capabilities is given along with modifications made to the code for this project. Development of material properties used in the heat transfer analysis is also discussed. The code is applicable up to the point of delamination, should it occur. Lastly, comparison of model predictions to collected test data is presented.

4.3.2. One-Dimensional Heat Transfer Algorithm Overview

A comprehensive heat transfer analysis tool was developed to evaluate externally heated composite panels where 1-D heat transfer dominates the through thickness temperature profile. The tool was originally developed with the capability to model the basic heat transfer phenomenon of conduction through the sample, surface convection, and environmental radiation. More advanced processes related to resin decomposition at elevated temperatures, commonly referred to as pyrolysis were also included in the algorithm. The primary process for the heat transfer effect of material decomposition is included with a rate-dependent Arrhenius relation, discussed further in Section 4.3.2.1. The model can also predict the secondary heat transfer effect of pyrolysis byproduct outgassing through the remaining char of pyrolyzed outer layers. However, the outgassing term contribution has been found to be insignificant compared to the other processes, the properties of the process are not well characterized, and the feature can lead to convergence issues. Therefore, this optional feature of the model was not considered in the present analysis.

In the model, a laminate is discretized into nodes through the sample thickness. The algorithm was set up as an explicit transient finite difference solver with fixed grid spacing based on an

initial thickness. The thickness and grid spacing is assumed constant, and does not presently account for the effects of delamination between adjacent plies. The number of nodes through the thickness is a user-specified number parameter but typical runs are executed with 2 grid points per ply, which is convergent at the heat flux levels considered in this study. Higher heat levels tend to require more refined discretization or smaller time stepping due to higher temperature differences between nodes. Temperature at every node is calculated explicitly at every time step until a user-defined end time is reached. The calculation time step is updated automatically for each iteration.

A diagram of the model is shown in Figure 23. Separate effects considered by the model are broken out into individual terms in the provided nodal temperature equations.

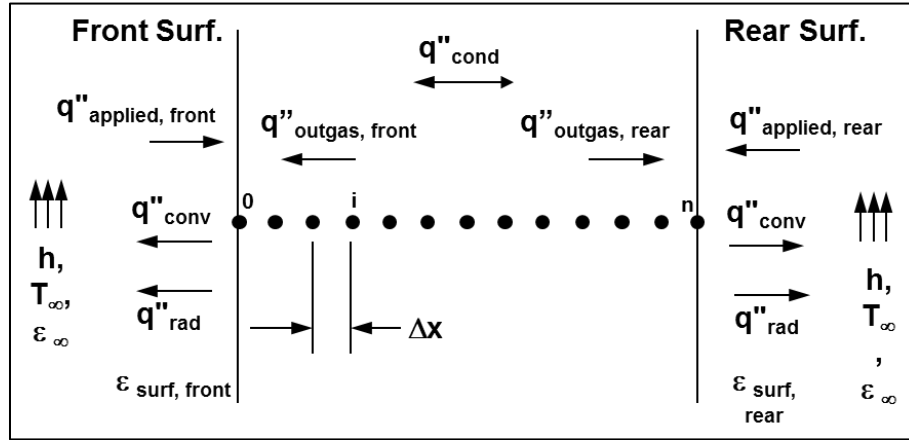


Figure 23. Discretized Heat Transfer Model for a Composite Laminate

The heat transfer formulation on the front surface, node 0, at the p+1 timestep is

$$T_0^{p+1} = T_0^p + \frac{2\Delta t}{\rho_0^p c_0^p \Delta x} \left[\underbrace{q''_F}_{\text{heat addition}} + \underbrace{h(T_\infty - T_0^p)}_{\text{surface convection}} + \underbrace{\sigma(\epsilon_\infty T_\infty^4 - \epsilon_F T_0^{p4})}_{\text{surface radiation}} + \underbrace{k_0^p \frac{(T_1^p - T_0^p)}{\Delta x}}_{\text{internal conduction}} - \underbrace{\Delta x \rho_0^p \Delta H \dot{\alpha}_i^p}_{\text{pyrolysis reaction}} - \underbrace{h_{gas,0}(T_0^p - T_{gas,0}^p)}_{\text{pyrolysis outgassing}} \right]$$

where T is temperature, Δt is the time step, ρ is density, c is specific heat, σ is the Stephan-Boltzmann constant, ϵ is emissivity, k is thermal conductivity, h is the convection coefficient, ΔH is the heat generated/absorbed by the pyrolysis reaction, α is the fraction of decomposed material and Δx is the spacing between nodes. The q'' is the heat flux exposed to the free surface with subscript ' F ' for front. The pyrolysis reaction term is described in more detail in the next section. Similar to the front surface formulation the temperature on the rear surface, node n , with heat flux, q''_R , is

$$T_n^{p+1} = T_n^p + \frac{2\Delta t}{\rho_n^p c_n^p \Delta x} \left[q''_R + h(T_\infty - T_n^p) + \sigma(\epsilon_\infty T_\infty^4 - \epsilon_R T_n^{p4}) + k_n^p \frac{(T_{n-1}^p - T_n^p)}{\Delta x} - \Delta x \rho_n^p \Delta H \dot{\alpha}_i^p - h_{gas,n}(T_n^p - T_{gas,n}^p) \right]$$

The temperature formulation for interior (i) nodes, T_i , without surface heat transfer effects reduces to

$$T_i^{p+1} = T_i^p + \frac{\Delta t}{\rho_i^p c_i^p \Delta x} \left[\frac{k_i^p}{\Delta x} (T_{i+1}^p - 2T_i^p + T_{i-1}^p) - \Delta x \rho_i^p \Delta H \dot{\alpha}_i^p - h_{gas,i} (T_i^p - T_{gas,i}^p) \right]$$

4.3.2.1. Pyrolysis Reaction Modeling

A physically meaningful approach to modeling pyrolysis is with an energy conservation equation. This is done by adding a rate dependent term

$$\frac{dQ}{dt} = -\rho \Delta H \frac{d\alpha}{dt}$$

where ρ is solid mass density, ΔH is the heat generated/absorbed by the reaction, α is the fraction of decomposed material, and Q is heat flux. The process is exothermic for negative values of ΔH and endothermic for positive values (the decomposition/phase change model allowed for endothermic reactions only). The decomposition rate term is typically modeled using an Arrhenius relation [e.g., 20, 21], which is shown here in the form

$$\frac{d\alpha}{dt} = A(1-\alpha)^m e^{(B/T)}$$

For a specific material system of interest, decomposition kinetic parameters A , m , and B can be determined empirically through TGA. Determination of decomposition kinetic parameters for the materials considered in this study is discussed in detail in Section 4.3.4. Improvements to the pyrolysis model, among other changes, are discussed in the following section.

4.3.3. Model Improvements and Added Features

Several changes were made to the previously developed heat transfer code [19] to suit the specific needs of this study. The changes are described in the following subsections.

4.3.3.1. Model Input and Output

Basic input and output features were added to the code including:

- Comma-separated-value (CSV) output files were added to monitor pyrolyzed fraction and temperature vs. depth at each time step.
- The user-specified input of surface heat flux and free-stream temperatures was made more flexible by adding time-dependent input tables in place of the previously specified constant input values.
- The user input front and rear surface free-stream temperature was made independent, such that the test conditions could be better represented by a transient, hot flame on one side and atmospheric conditions on the other.

4.3.3.2. Pyrolysis Model Improvements

The original model was developed with density and decomposed fraction values as temperature-dependent user-specified tabular values. The intended use for the model was with very high heating rates, making this approximation valid. In reality, decomposition is dependent on heating rate as discussed in Section 4.3.2.1, not fixed temperatures, and the previously used approximation is not valid at the lower heating rates considered in this study. To properly model

heating rate dependent decomposition, the code was improved to directly calculate density and decomposed fraction as a function of time through direct integration of the Arrhenius decomposition rate equation. This approach is consistent with other pyrolysis models in the literature [18, 20].

To evaluate the effect of the change, a test case was run with both the original and the revised pyrolysis algorithm. The test case considered a 13-ply AS4/3501 Graphite-Epoxy sample with properties taken from reference 12 exposed to a 10 s soak on the front surface of 250 kW/m². The calculated front and rear surface temperatures for both scenarios are compared in Figure 24. For the conditions considered, the model change had an appreciable effect and resulted in higher overall surface temperatures.

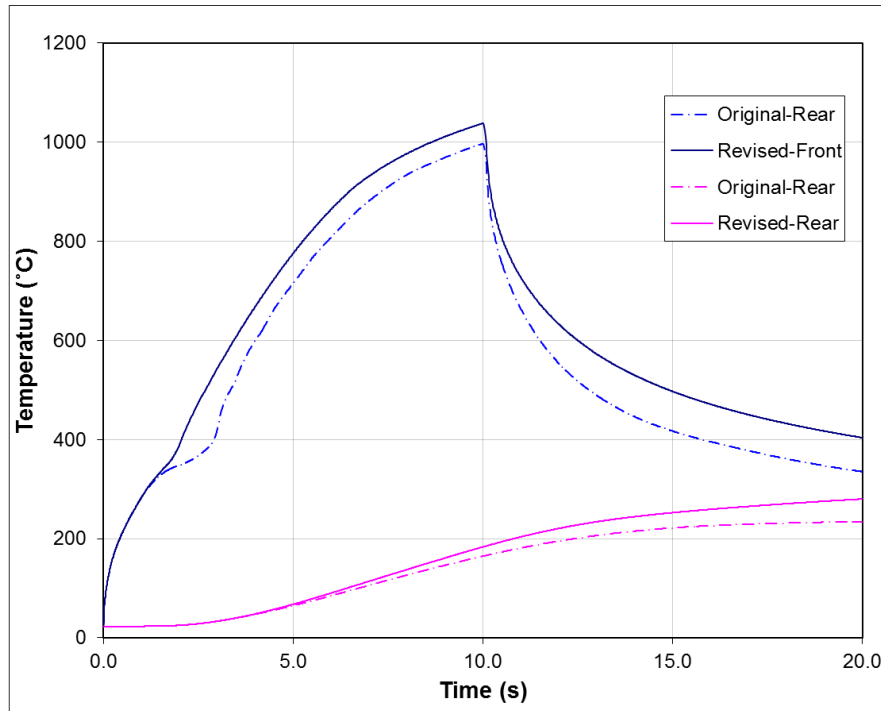


Figure 24. Comparison of Original and Revised Pyrolysis Model

Though typically dominated by a primary stage, the constituents of organic resin compounds often decompose at different rates [22, 23]. TGA for the three systems of interest indicated multiple decomposition stages, with a dominant primary stage and a secondary stage occurring at lower temperatures. Modeling the secondary stage was considered important for predicting the relatively low temperature decomposition that preceded delamination in some systems. An approach to multi-process decomposition is to model the processes individually with multiple overlapping Arrhenius relations. In the multi-process Arrhenius decomposition model, the decomposition rate term used in the heat transfer model was reformulated to be the sum of the rates from the various modeled processes:

$$\dot{\alpha} = \sum_i A_i (CF_i - \alpha_i)^{m_i} e^{(B_i/T)}$$

Where α is the decomposed fraction; A , B , and m are model fit parameters; and CF is the process conversion fraction (single process: $CF = 1$). Pyrolysis for the systems of interest was modeled with two rate equations, one for the main process and one for lower temperature decomposition. Decomposition kinetic parameters for each process were determined by fitting TGA data from each system. In the model, the heat transfer contribution from each process is calculated independently based on these separate parameters and superimposed for a total pyrolysis term contribution. Development of the pyrolysis model parameters based on TGA data for the systems of interest is discussed in detail in the next section.

The overall heat transfer algorithm highlighting the added features is shown in Figure 25.

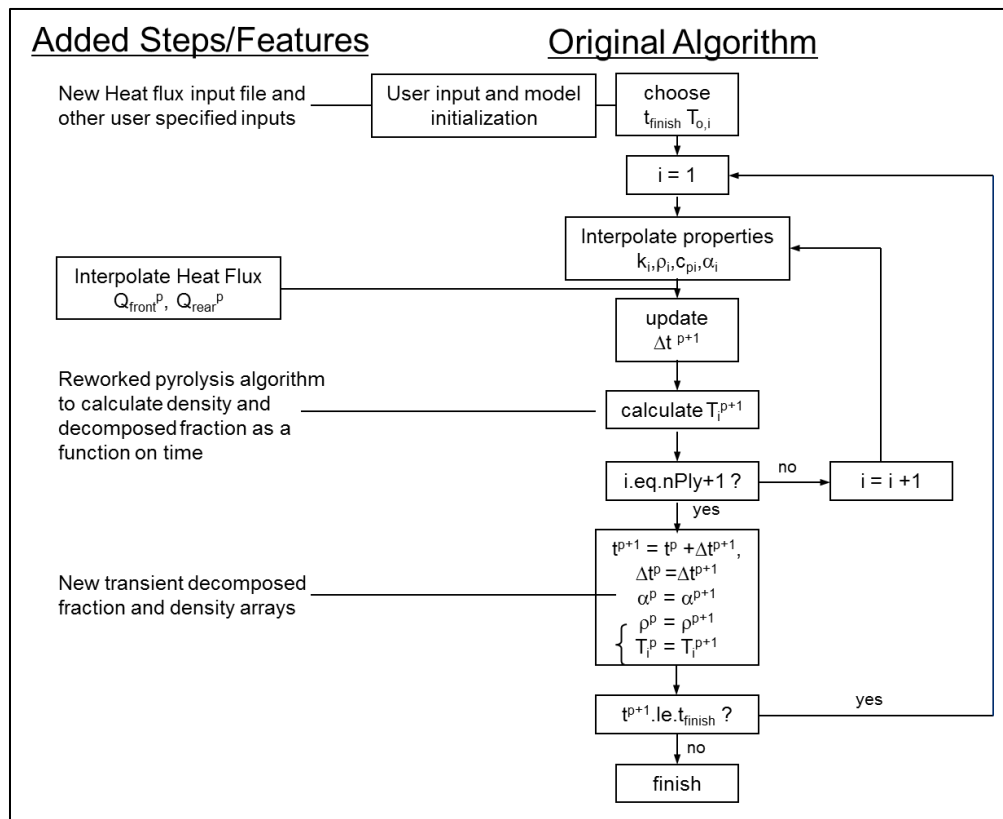


Figure 25. Updated Heat Transfer Algorithm Flow Chart

4.3.4. Pyrolysis Model Calibration

Decomposition kinetic parameters vary widely from material to material and are not typically published by manufacturers or in the open literature. Some data exists for similar resin systems but, given the important nature of pyrolysis on heat transfer and composite material damage, developing accurate decomposition models for each specific system was necessary. To achieve this, parameters for Arrhenius pyrolysis decomposition models were developed from TGA testing of each of the three IM7 reinforced resin systems of interest: Cycom 977-3, IM7/AFR-PE-4, and RM3002. The TGA testing and pyrolysis model parameter fitting is discussed in the following subsections.

4.3.4.1. Thermogravimetric Data

Thermogravimetric testing was conducted on samples of the composite systems per ASTM Standard E1641-07, “Standard Test Method for Decomposition Kinetics by Thermogravimetry.” [24] The standard provides guidance on testing procedures with thermogravimetry equipment and for the determination of decomposition kinetic parameters from the resulting data. The main outputs from TGA sample testing are plots of mass fraction versus temperature, which are later used to determine decomposition kinetic parameters.

Tests were conducted per the standard from granulized 3 ± 1 mg samples for each fiber-resin system. Samples were prepared from sections of the composite heating and mechanical test panels. The tests were conducted at four heating rates of 2, 5, 10 and 20 °C/min up to 1000 °C. Tests done at the AFRL/RXQ Fire Laboratory, labeled ‘AFRL’ in the following figures, were conducted with a NETZSCH STA 409PC/PG specifically designed for TGA sample testing. Some tests were performed by the manufacturer on their own test equipment (NETZSCH STA 449F1), labeled ‘Netzsch’ in the following figures. Plots of mass fraction versus temperature at four heating rates are shown in Figure 26–Figure 28 for each of the three composite systems.

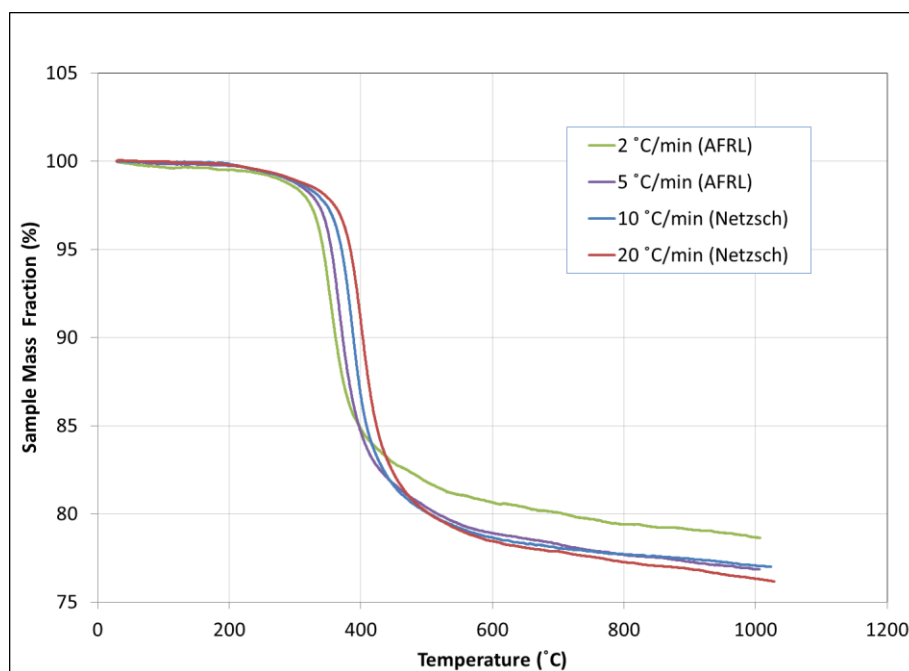


Figure 26. Cycom IM7/977-3 Raw TGA Data

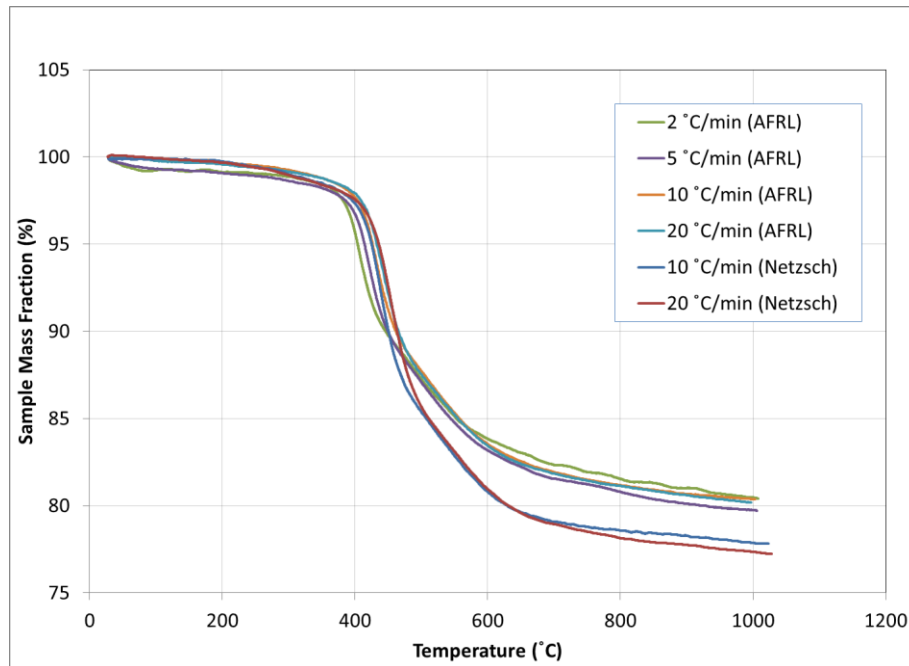


Figure 27. IM7/RM3002 Raw TGA Data

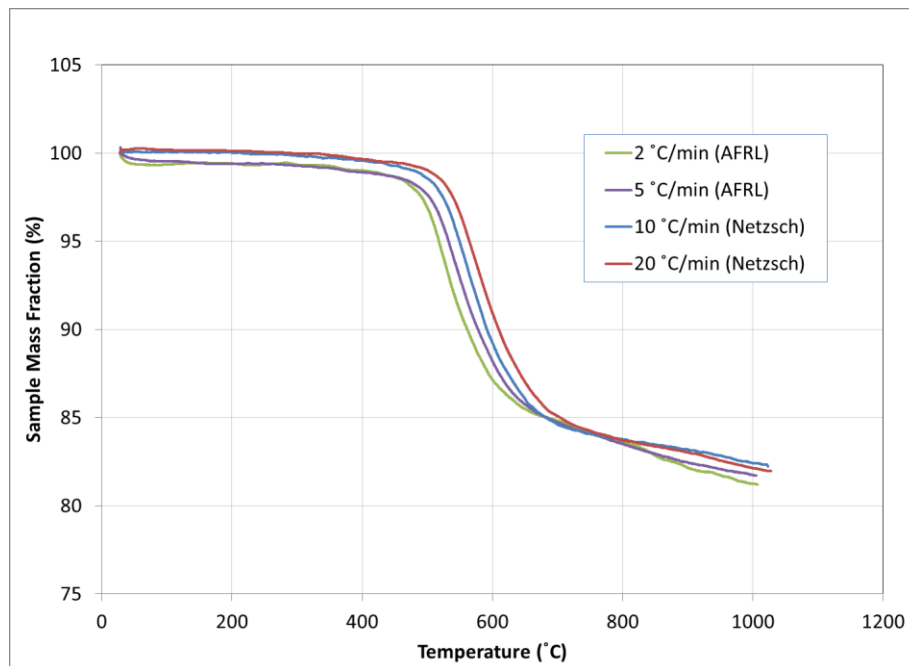


Figure 28. IM7/AFR-PE-4 Raw TGA Data

For each of the tests, approximately 20 to 25 percent of the total sample mass is converted to gaseous byproducts due to heating. In these composite systems, the resin undergoes decomposition leaving behind the carbon fiber and possibly resin char byproducts.

There was an apparent drop in mass at low temperatures for tests performed at AFRL (2 and 5 °C/min heating rates) in Figure 27 (IM7/RM3002) and Figure 28 (IM7/AFR-PE-4). The reason for this drop is unclear. The drop in mass could be artificial and due to unresolved issues with the test apparatus mass balance. Or the effect could be an artifact of a true low temperature degradation process that is only evident at lower heating rates. In either case, the higher rate data was taken as more appropriate for pyrolysis model development since it was closer to the heating rates that were used in the panel testing and those that would be experienced in a typical fire.

Repeated tests of IM7/RM3002 at the 10 and 20 °C/min heating rates were conducted on both test equipment. As shown in Figure 27, note that the mass fraction lost when tested in the Netzsch laboratory is greater. This difference is likely due to different fiber mass fractions between samples, where samples tested at AFRL had a higher fiber mass fraction and therefore less mass decomposed (up to a 6% difference in thickness seen (there were variations in thickness of over 10% in these plates). This difference among samples can be normalized by plotting the fraction of decomposed material, α , versus temperature, as shown in Figure 29. In this comparison, a reference value for a fully decomposed total sample mass fraction is taken at the upper test temperature (1000 °C) and the data is normalized between 100 percent (no decomposition) and 0 percent (fully decomposed). The comparison verifies that the rates and character of the decomposition curves are quite similar. The AFRL tests are more tightly grouped but fall within the Netzsch data. The nearly fixed 10-15 °C offset exhibited by the Netzsch data at the two tested heating rates is more typical of other TGA data in the literature [24,22,23], than the tightly grouped and sometimes overlapping AFRL data.

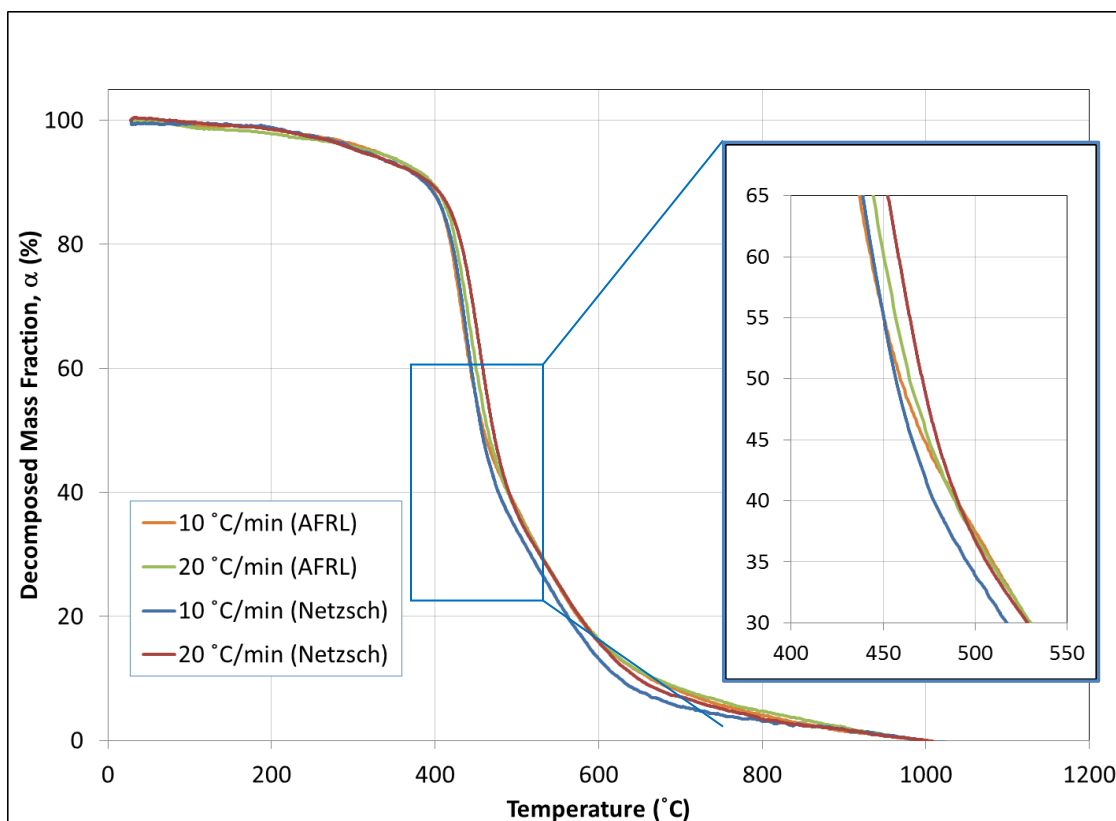


Figure 29. Decomposed Mass Fraction of IM7/RM3002 at 10 and 20 °C/min

The data provided by Netzsch at 10 and 20 °C/min were used as a basis for the pyrolysis model fit for all three materials. This was done for several reasons. The heating rates for the full plate heat exposure tests are substantially higher than those tested thermogravimetrically, so the highest rate TGA tests were most appropriate for developing the pyrolysis model. Furthermore, whether the low temperature mass loss seen at the low testing rates was real or an artifact of the test equipment could not be determined since no low-rate testing were performed in the Netzsch laboratory. The model fit procedure using the Netzsch 10 and 20 °C/min heating rate data is described in detail in the next subsection.

4.3.4.2. TGA Data Fitting

Pyrolysis models were fit to the TGA data using the iterative procedure defined in ASTM E1641-07. Initially, the basic procedure was used to fit a single-process Arrhenius decomposition model to the TGA data described in Section 4.3.2.1. However, it was clear from comparing the single process fit to the TGA data that the systems of interest exhibit multiple decomposition processes. This behavior is common in organic compounds where the decomposition onset of the volatile constituents can occur at different temperatures [22]. Single-process models compared to the 20 °C/min TGA can be seen in Figure 30. This model reproduces the primary decomposition rate very well for each system. However, deviation from the TGA data is seen at low and high temperatures on either side of the primary process.

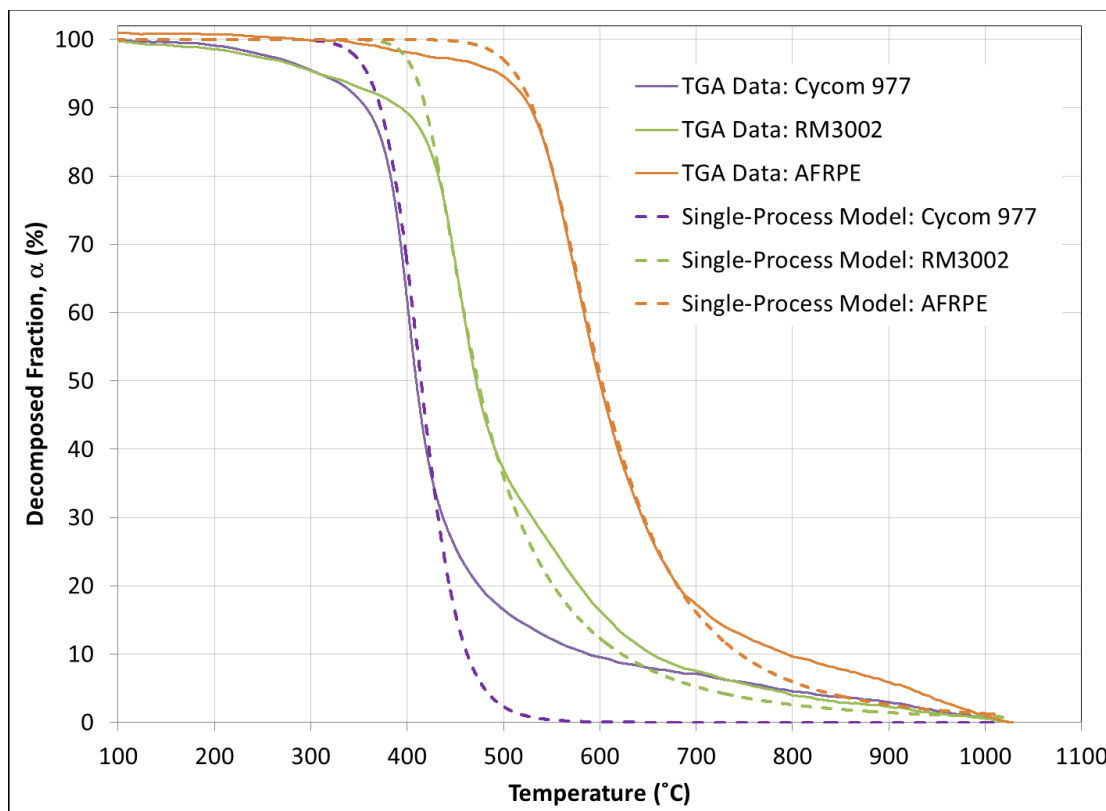


Figure 30. Comparison of 20 °C/min TGA Data and Single-Process Arrhenius Model

For this study, the low temperature decomposition transition proved an important part of the temperature range. Thus, a multi-process modeling approach was adopted to model the low temperature process as well as the primary process. The higher temperature processes were not addressed directly in this study because the heat exposure testing and residual mechanical composite strength assessment was focused on moderate heat damage seen during pyrolysis onset. A dual-Arrhenius process model was fit to the TGA data for each of the three composite systems. As with the initial single-process models, the iterative procedure defined in ASTM E1641-07 was used to fit the primary process, using the 20 °C/min rate data for reference values. The secondary low temperature process was fit manually by trial-and-error selection of the Arrhenius model parameters and of the total conversion fraction on which the secondary process acts.

As shown in Figure 31–Figure 36, the model compares well to the TGA data for both 10 and 20 °C/min heating rates. The decomposition rate is closely modeled from low temperature through the majority of the primary process. Some deviation is seen at higher temperatures, which was not of critical importance for this study. If more accurate simulation of high temperature decomposition is required in the future, the models can be improved by fitting more Arrhenius processes.

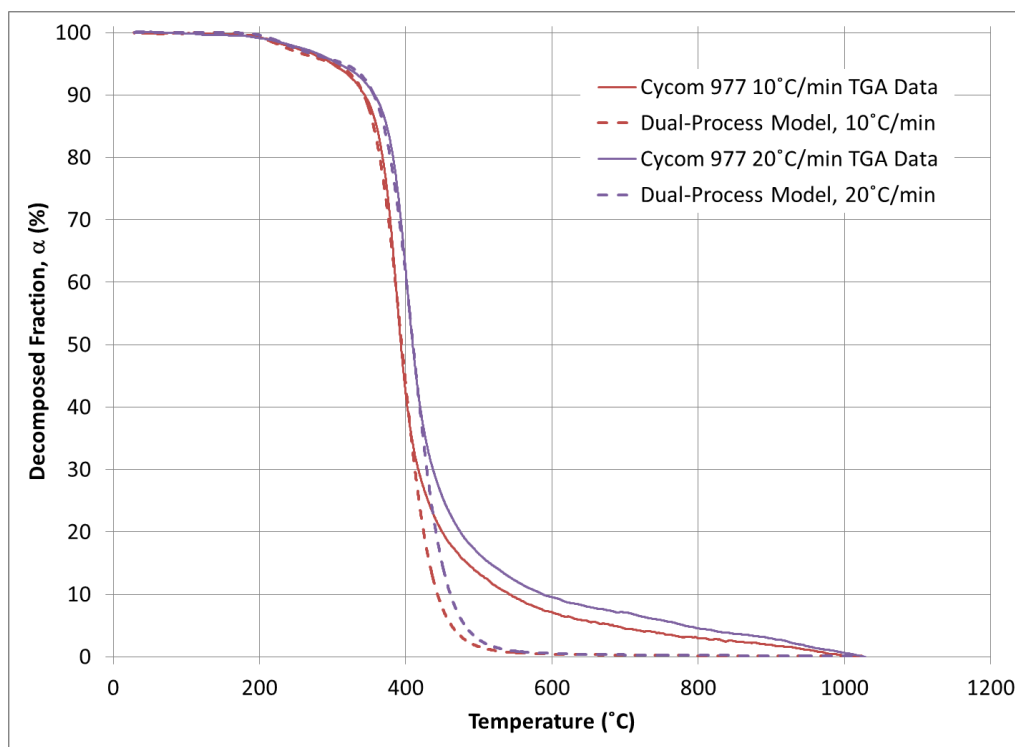


Figure 31. Cycom IM7/977-3 System Decomposition Fit Comparison to TGA Data at Both Tested Heating Rates

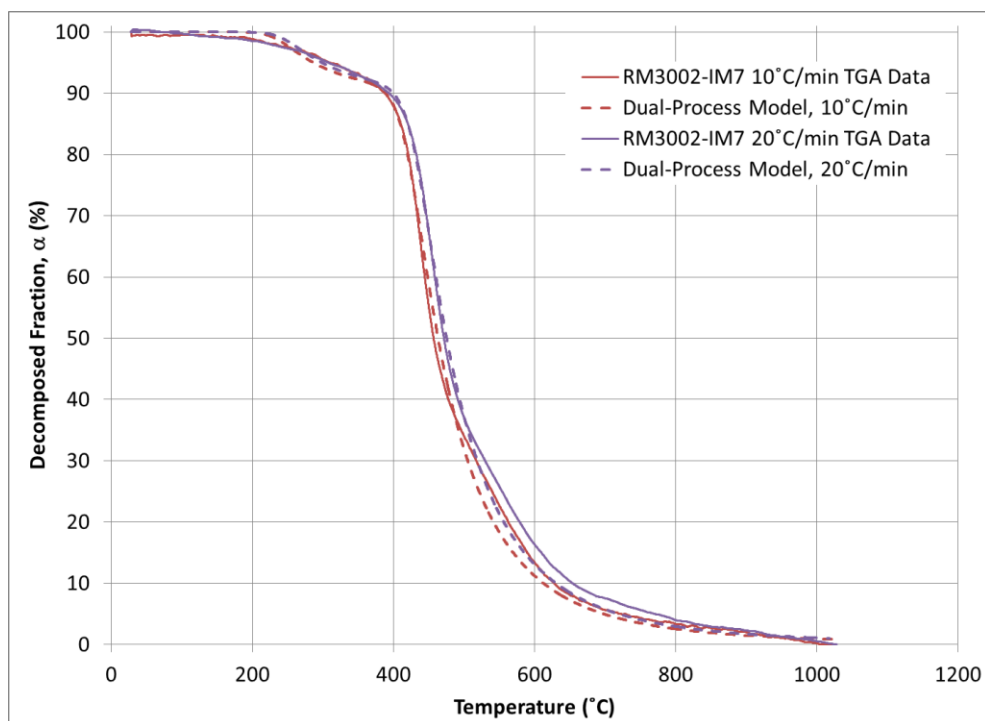


Figure 32. IM7/RM3002 System Decomposition Fit Comparison to TGA Data at Both Tested Heating Rates

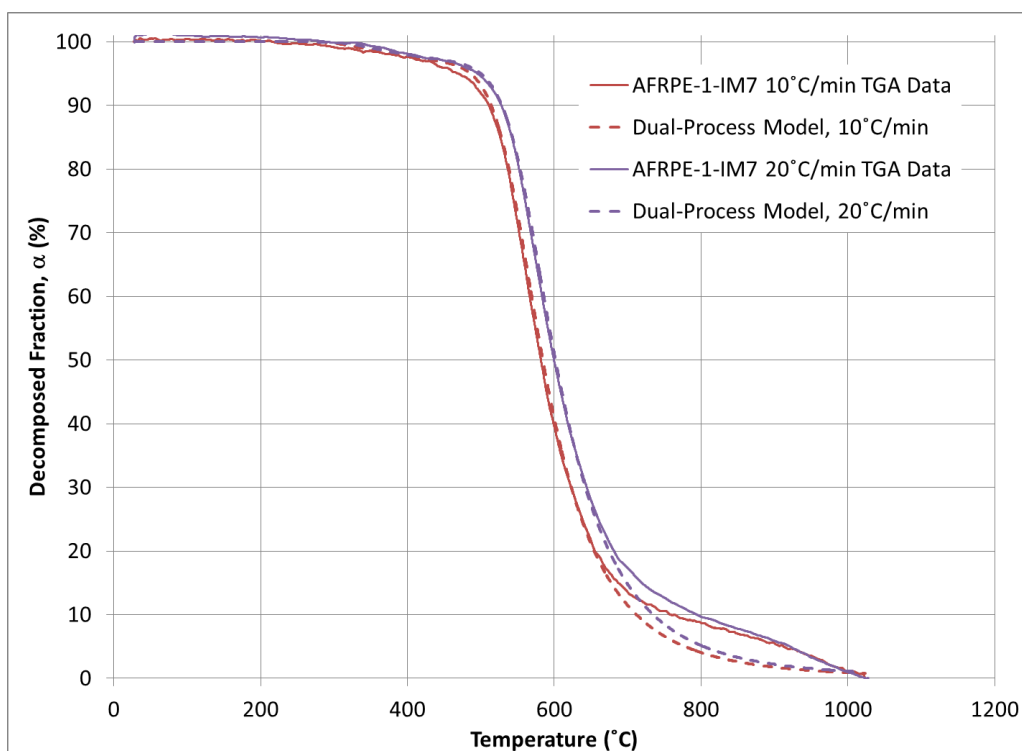
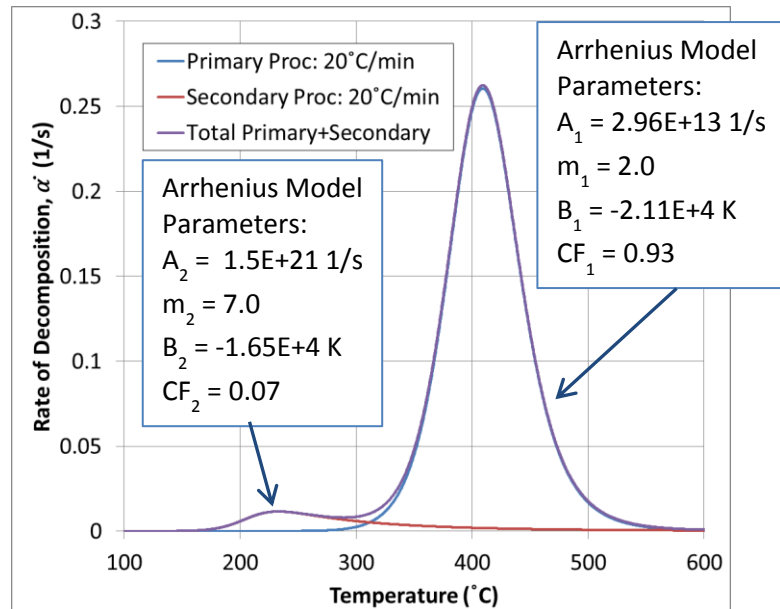
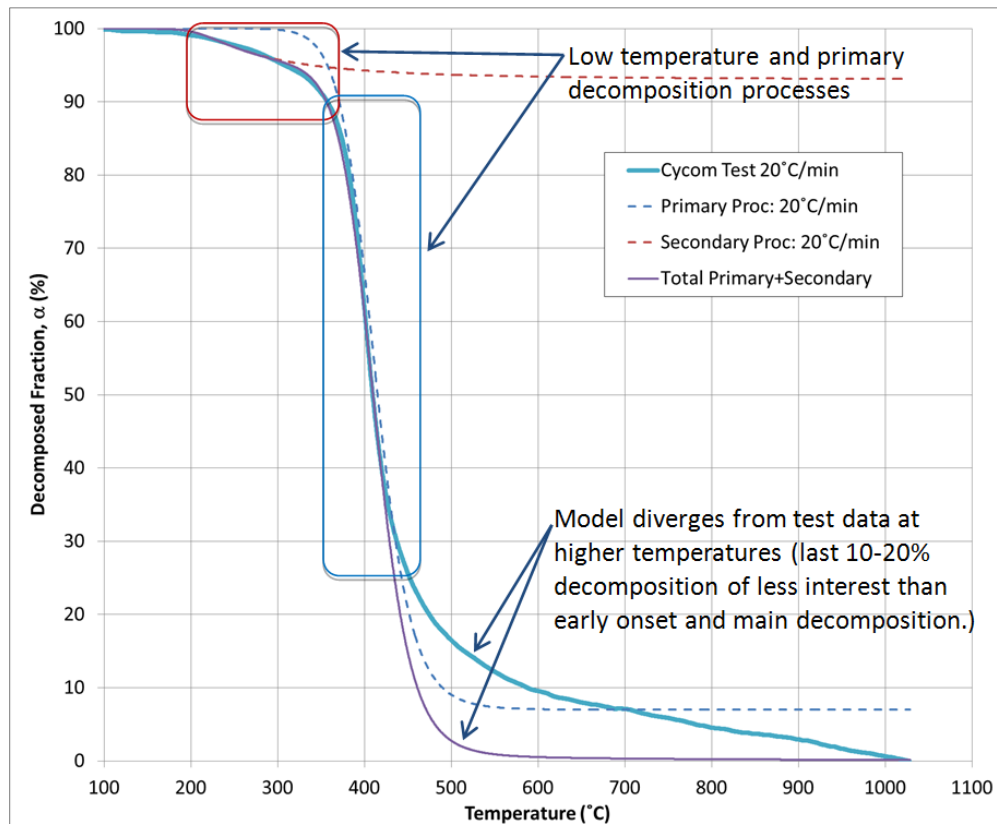


Figure 33. IM7/ARFPE System Decomposition Fit Comparison to TGA Data at Both Tested Heating Rates

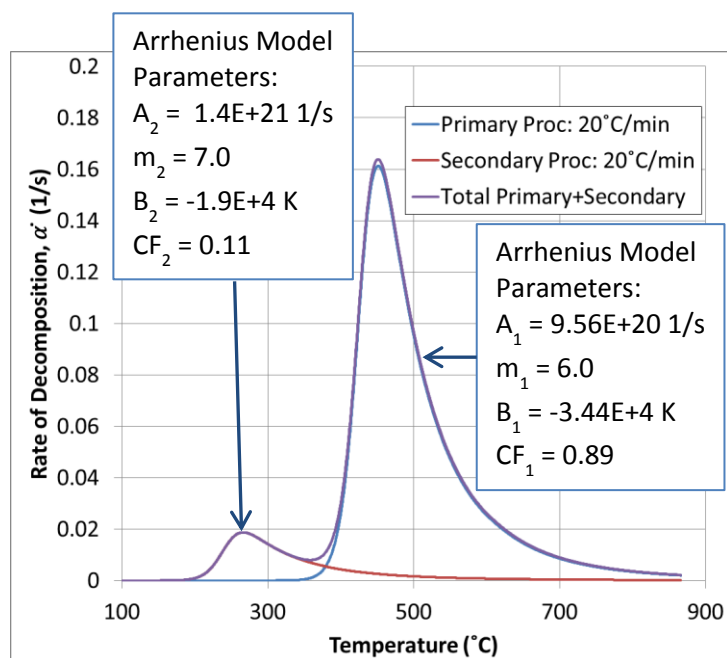


a) Rate of Decomposition

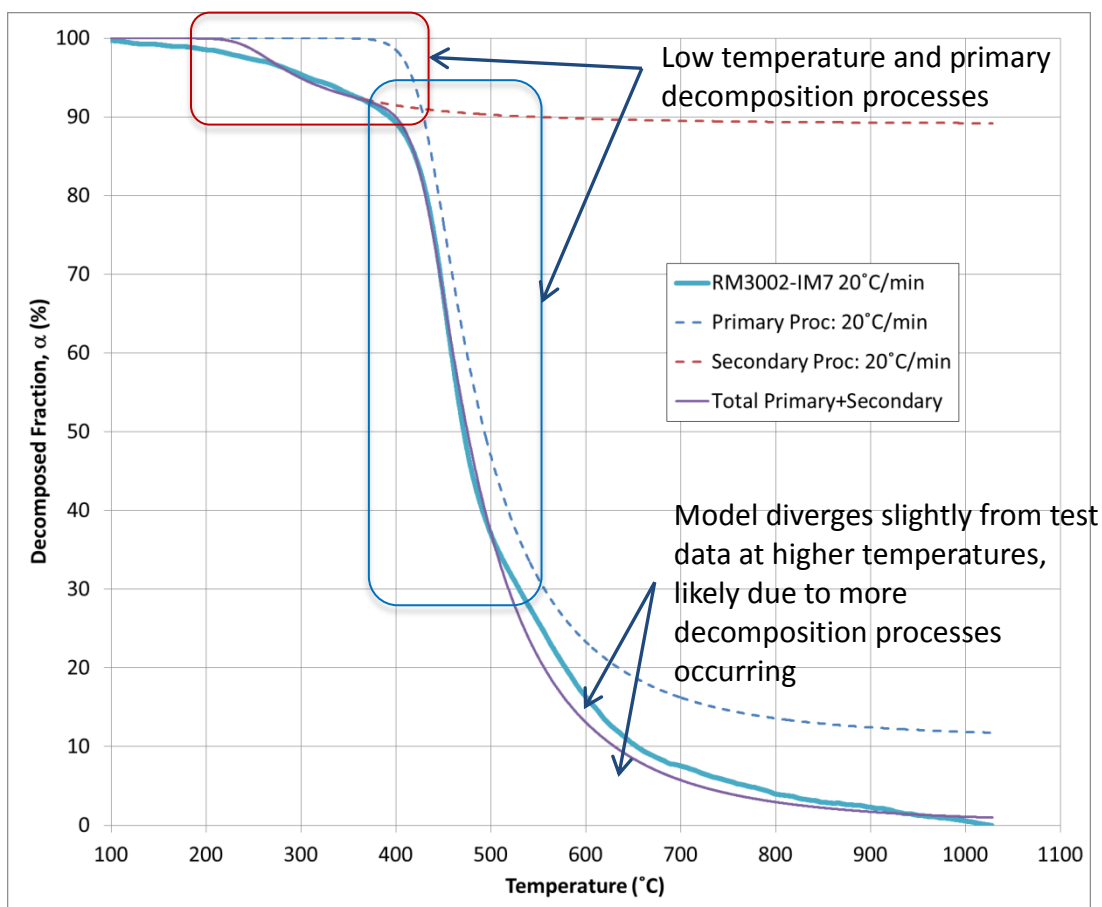


b) Decomposition Fraction

Figure 34. Cycom IM7/977-3 System Decomposition Model, 20 $^{\circ}\text{C}/\text{min}$ Heating Rate

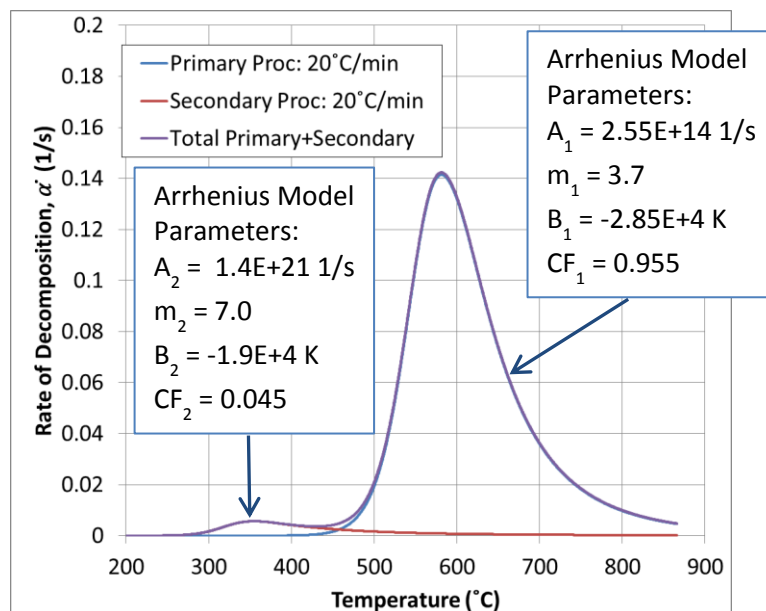


a) Rate of Decomposition

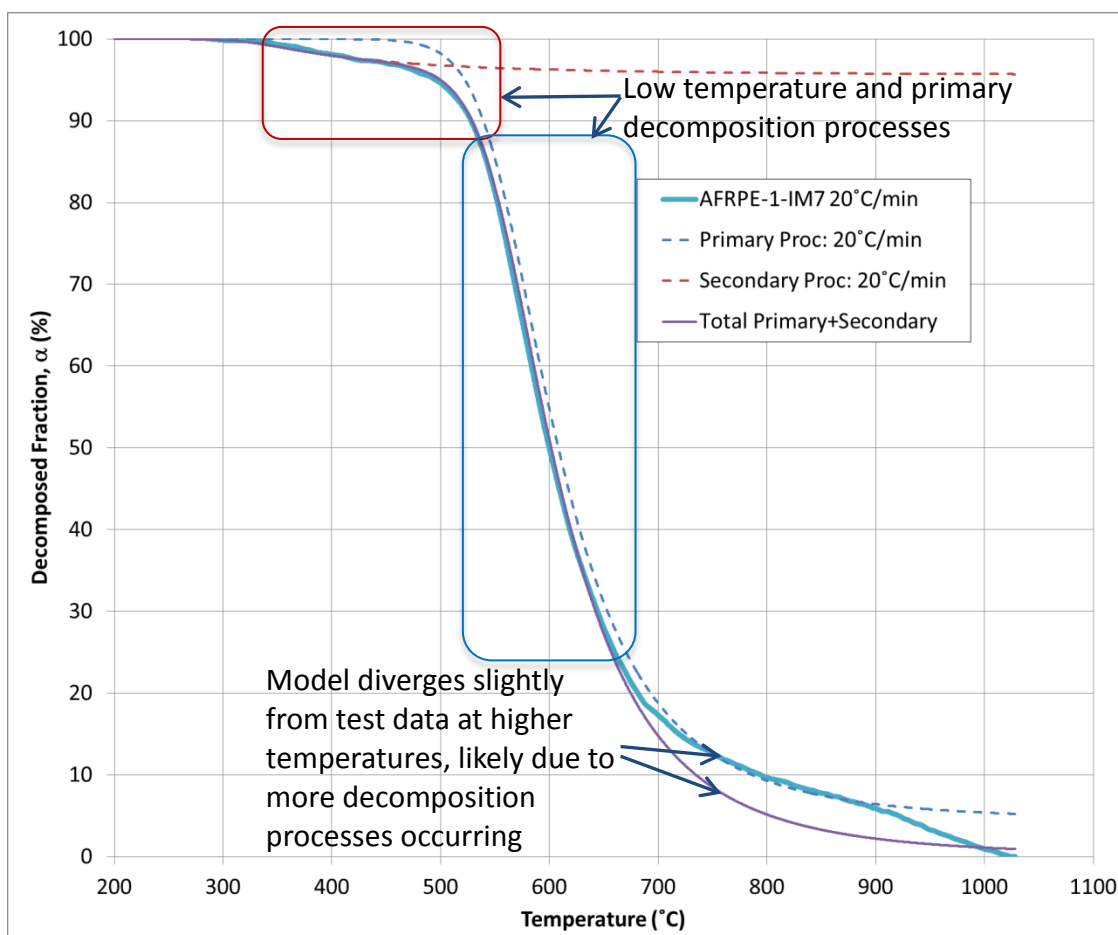


b) Decomposition Fraction

Figure 35. IM7/RM3002 System Decomposition Model, 20 °C/min Heating Rate



a) Rate of Decomposition



b) Decomposition Fraction

Figure 36. IM7/ARFPE System Decomposition Model, 20 °C/min Heating Rate

4.3.5. Temperature-Dependent Physical Properties

Temperature-dependent properties for density, thermal conductivity, and specific heat are required to accurately predict heat transfer through the composite materials. As the material chemistry and constituents change, thermal properties can vary widely in carbon fiber reinforced polymers (CFRP) as temperature is elevated from virgin material properties, up to and through pyrolysis decomposition, and finally as fully pyrolyzed char/fiber material.

Properties can vary significantly from system to system and data is typically not readily available from the component manufacturers or in the open literature. For the materials used in this study, thermal property data was not available and the required thermal properties were not directly measured. Instead, properties were initially estimated with existing published data for similar systems [21, 25-28]. Then the properties were calibrated based on observed behavior from the composite plate heat exposure tests. Calibration was limited to the temperature range of the tested samples. Properties above the tested temperatures are estimates based on properties of similar systems.

Prior to calibration, initial profiles were developed with the following considerations:

- Initial properties were estimates based on existing data for similar systems.
- Virgin material density was calculated based on fabricated weights and volume of the test article plates.
- System-specific T_g were used for decomposition onset breakpoints in thermal properties.
- System-specific properties were adjusted as higher temperature data became available from ongoing tests.
 - Properties were calibrated up to pyrolysis onset in most cases (~340 °C).
 - Higher temperature properties are estimated based on reported behavior of other similar systems and assumes decomposed material (consisting mostly of IM7 fiber) is basically the same in all systems tested.

The temperature-dependent thermal properties developed during this study are shown in

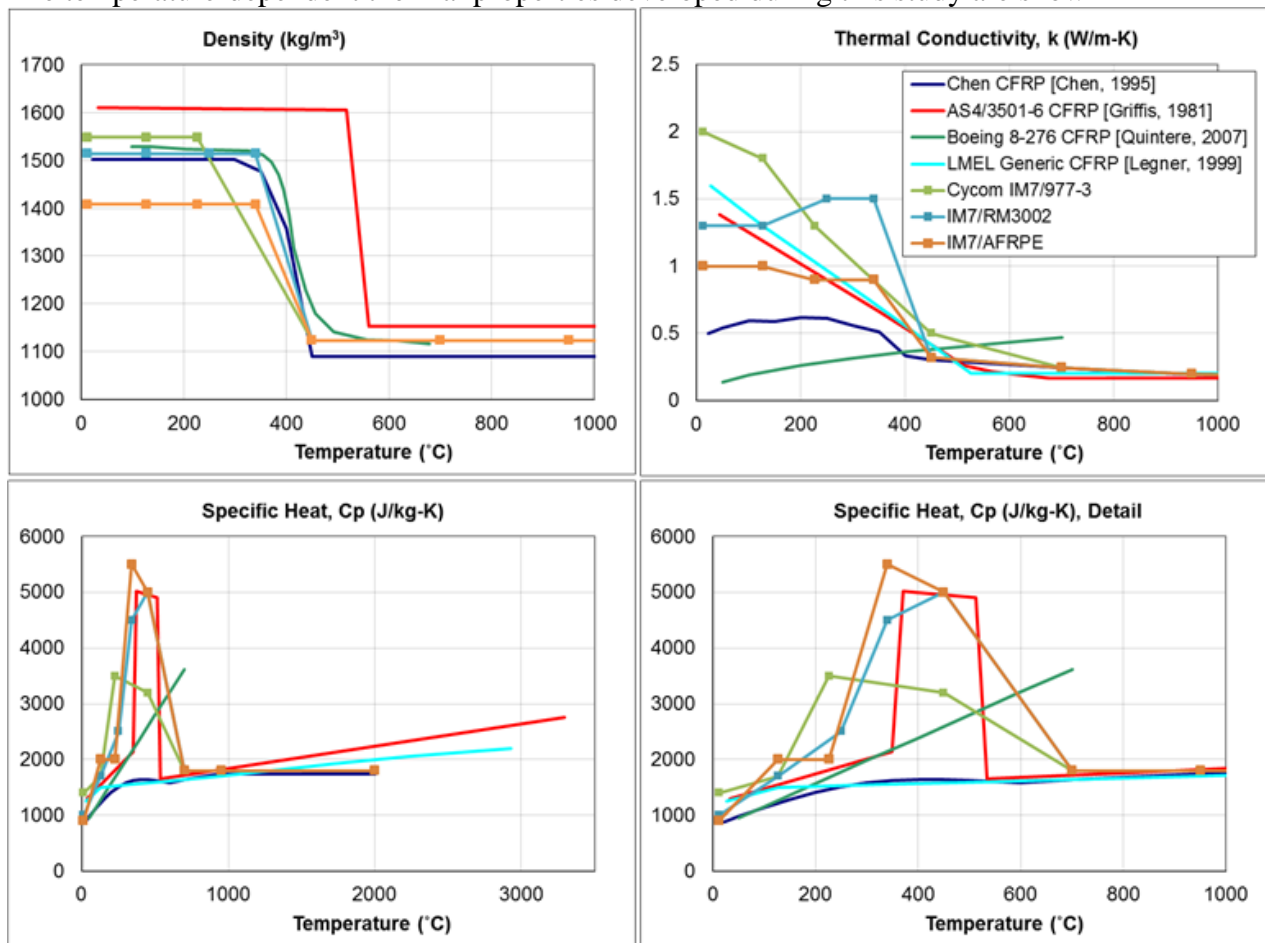


Figure 37, which compare the three tested systems and the published data used as an initial basis for property estimation. Predicted behavior from the property calibrated model is compared to tested response of each system in Section 4.3.6.

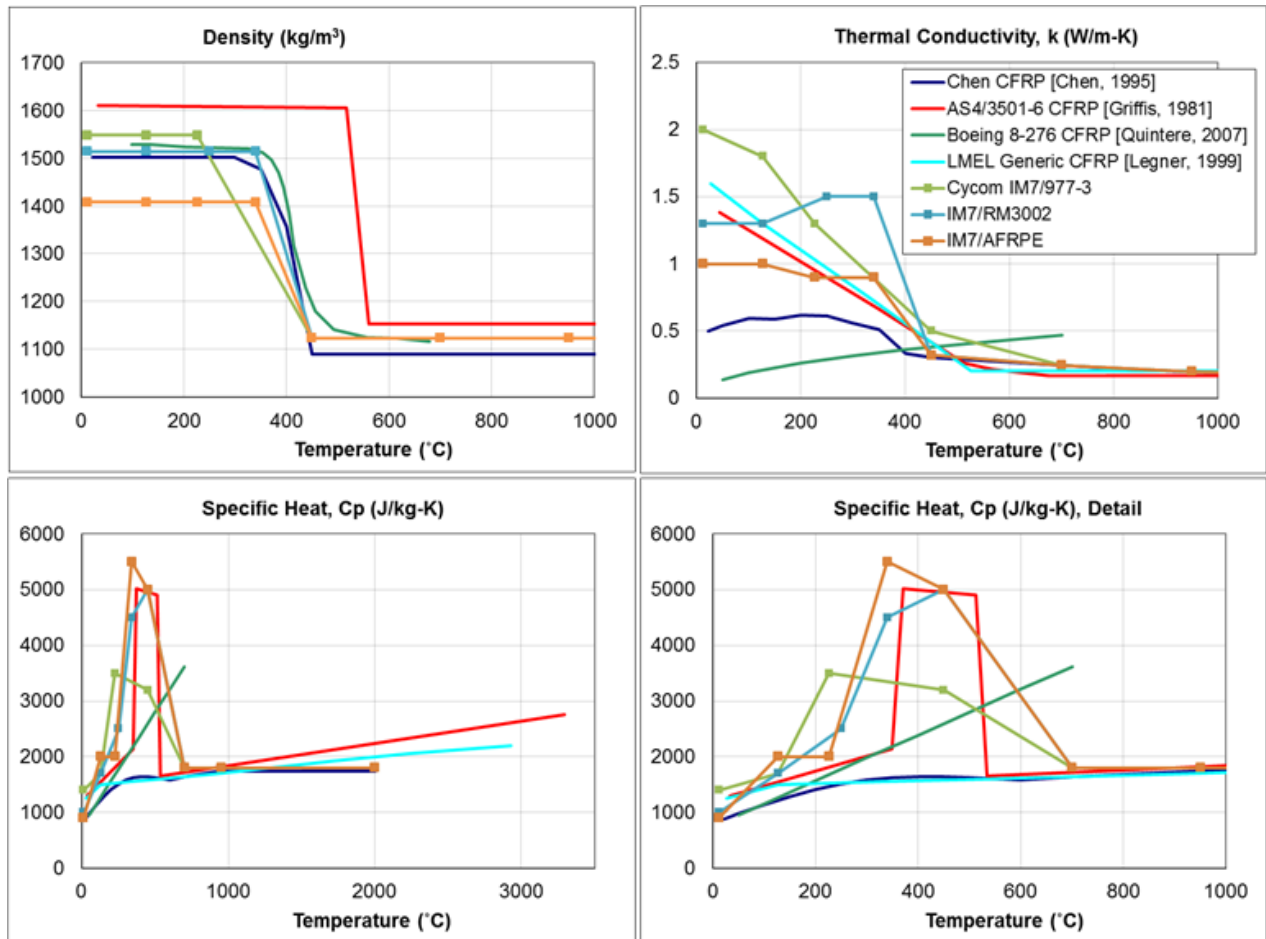


Figure 37. Temperature-Dependent Physical Properties

4.3.6. Predictions of Composite Plate Experiments

With the fully developed 1-D heat transfer code and calibrated thermal properties, the model can be used to predict through-thickness temperature profiles up to the point of delamination. The model was used to guide plate heat exposure tests and can be used to predict thermal histories under other exposure conditions and composite layups.

4.3.6.1. Model Input Procedures

The same procedure was used to model all heat exposure tests. In running the model, environmental conditions as well as plate conditions were taken into account. Measured thickness from each sample plate was used in pre- and post-test predictions. For post-test sample predictions, the initial temperature was set based on thermocouple data. For predictions not based on individual tests, a representative temperature for the test lab was used.

Front surface heat flux as a function of time was prescribed in the model. The input heat flux accounts for all environmental heat transfer processes on the heat-exposed side (e.g. radiation and convection), which is captured in the test setup by a heat flux sensor adjacent to the plates and approximately in the center of the heat exposed area. For pre-test predictions, constant heat

flux was applied as an idealized step function for a pre-selected exposure time and stepped down to zero flux to simulate exposure and removal of a plate to a heat source.

For post-test predictions, the heat flux as a function of time was provided directly from the test data. For cases where multiple tests at similar heat exposures were used for model parameter calibration, an average time dependent heat flux curve was used in the model. Figure 38 shows an example of a simplified average heat flux profile used in model calibration. In this case for IM7/AFR-PE-4, four tests were performed (A3, A2 A8, and A9) with similar nominal 35 kW/m^2 heat flux profiles. The data collected from the heat flux sensor was averaged and a simplified piecewise linear representation of the average was used to calibrate the model response to the test behavior.

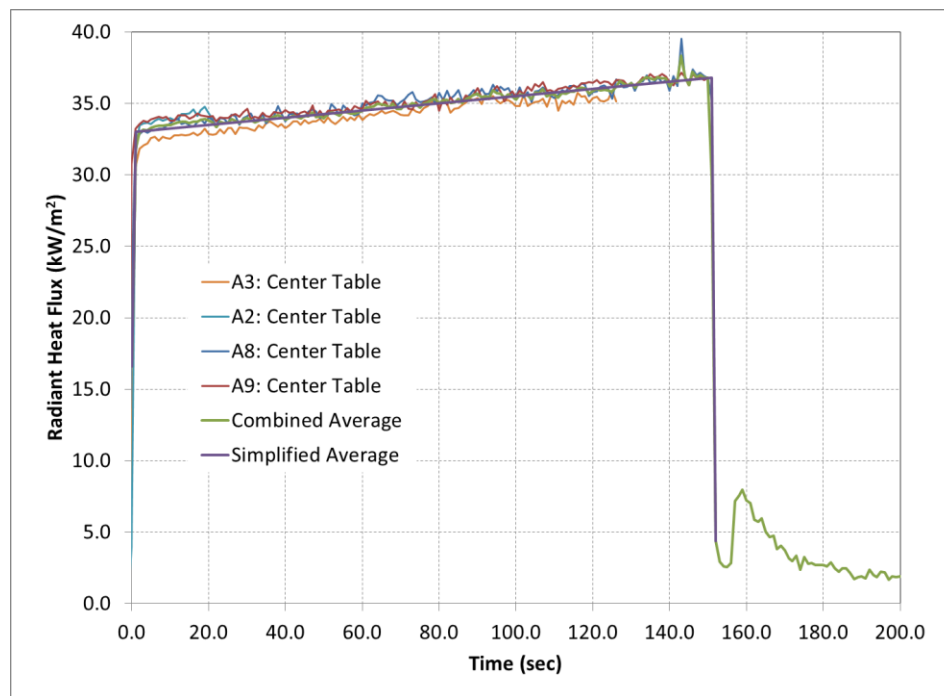


Figure 38. Example of Modeled Average Heat Flux Compared to Test Data

The rear face of each composite plate was insulated with 12.7 mm thick flexible insulation. In the model, the backside of the panels were considered perfectly insulated. Environmental convection and radiation, and conduction with the insulation material were effectively not allowed in the model by means of zeroing the process input parameters through the rear face. In the tested panels, some amount of rear face heat transfer does occur, as indicated by collected backside insulation TC data. However, the mechanism and extent of heat loss through the rear face was uncharacterized. Given the higher temperature gradients and reduced heating time, the backside heat loss is minimized at the highest heat flux of 35 kW/m^2 . Therefore, thermal properties were calibrated to the high flux test data with the assumption that heat flux through the rear face for these tests was negligible. Without modeling rear face heat loss, the model will tend to over predict through-thickness temperatures at lower heat input levels, compared to the test data. Calibrated properties are therefore estimates and should be better characterized using test

methods specific to measuring through-thickness thermal conductivity and specific heat in order to improve model predictions for general use [e.g., 26].

4.3.6.2. Test Predictions

The model was calibrated using data from the embedded TCs in the composite plates. In the following sections, the embedded TCs closest to the front and rear face of the test plates, labeled TC 1 and TC 7, respectively, are compared to the modeled response at various heat input levels.

4.3.6.2.1. IM7/RM3002

Plate R6 was tested with a nominal heat flux of 35 kW/m^2 and was used to calibrate the physical properties for IM7/RM3002. A comparison of the test and modeled response is shown in Figure 39. The model was then used for post-test predictions of the 25 kW/m^2 tests (R2, R3, and R9) and 15 kW/m^2 tests (R4, R7, and R8). The model and test comparisons are shown in Figure 40 and Figure 41, respectively. Note that sample R9 had higher moisture content, referred to as ‘wet’ in Figure 40. The test data indicates that moisture content had little effect on the conductivity and specific heat properties. Moisture content did, however, have a significant impact on delamination time. Estimated times when delamination occurs, affecting the embedded temperatures, are also shown in the figures.

The method for estimating these times and data from all embedded TCs are discussed in Section 5.3, but generally occurred when TC 1 reached approximately 250 to 300°C . As expected, the model tends to over predict the actual test data temperatures at lower heat flux levels, due to heat lost at the rear face that is not included in the modeling. Still, the model provides an adequate fit for all tested flux levels up to the expected delamination temperature.

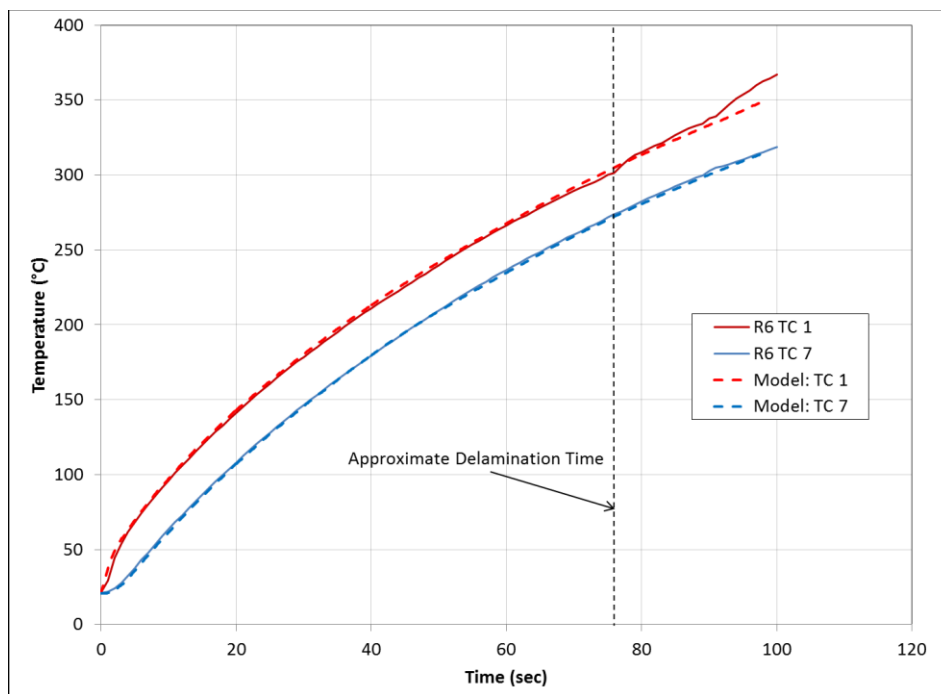


Figure 39. Predicted and Measured Temperatures of IM7/RM3002 Exposed to a Heat Flux of 35 kW/m^2

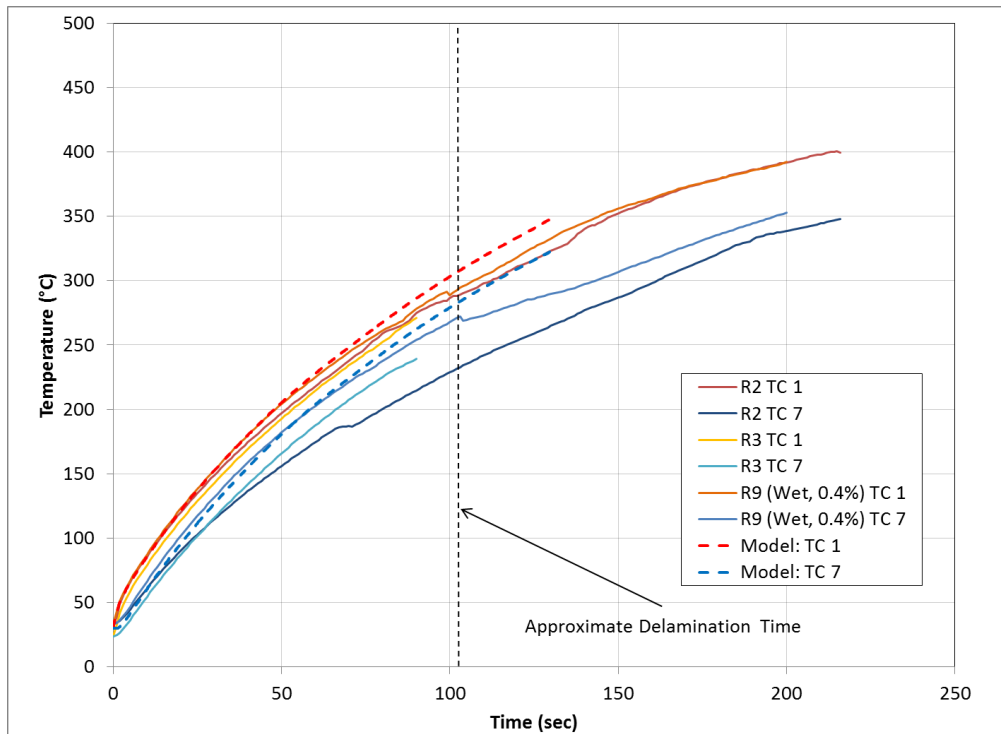


Figure 40. Predicted and Measured Temperatures of IM7/RM3002 Exposed to a Heat Flux of 25 kW/m²

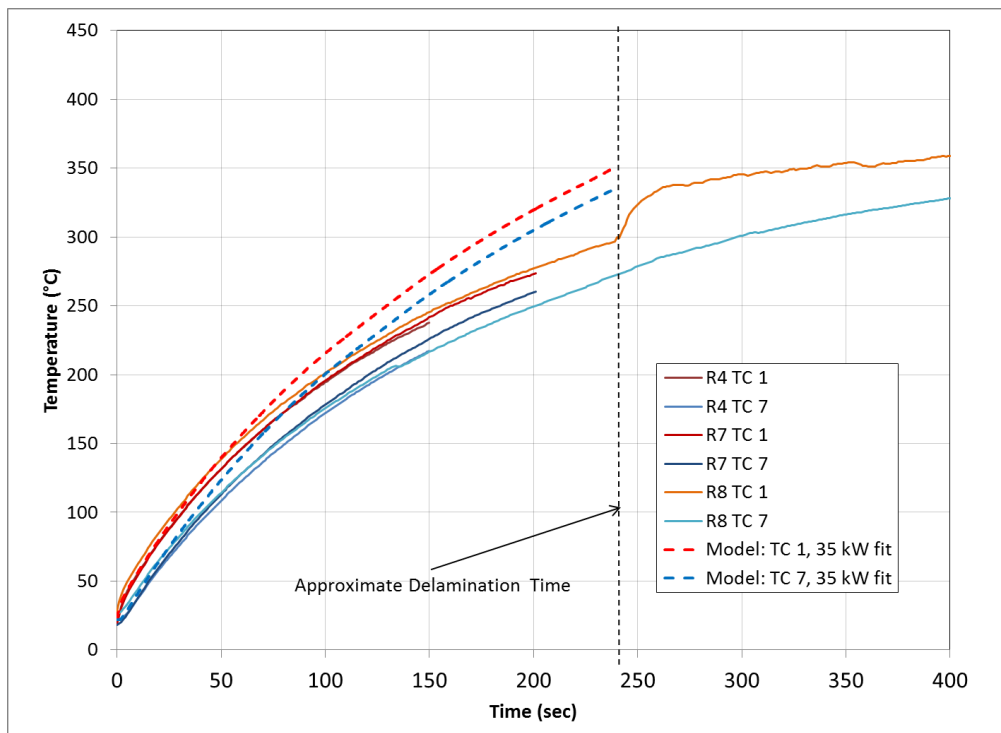


Figure 41. Predicted and Measured Temperatures of IM7/RM3002 Exposed to a Heat Flux of 15 kW/m²

4.3.6.2.2. IM7/977-3

Limited heat exposure testing was performed on IM7/977-3. Only one test with a short 20 s exposure at the high heat flux of 35 kW/m^2 was suitable to calibrate the physical properties of IM7/977-3. The short duration of this test only resulted in embedded temperatures of 110°C , as shown in Figure 42. To calibrate properties to higher temperatures, tests on plates C4 and C9 with a 15 kW/m^2 heat exposure were used. The model and test data comparison for 15 kW/m^2 heat exposure is shown in Figure 43. Since the 15 kW/m^2 tests have more significant heat loss on the rear surface the estimated properties are affected accordingly.

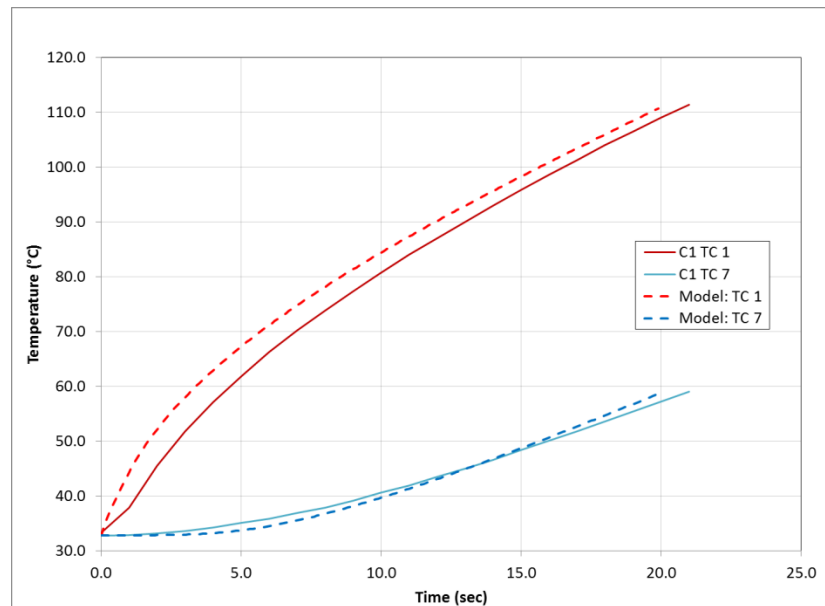


Figure 42. Predicted and Measured Temperatures of IM7/977-3 Exposed to a Heat Flux of 35 kW/m^2

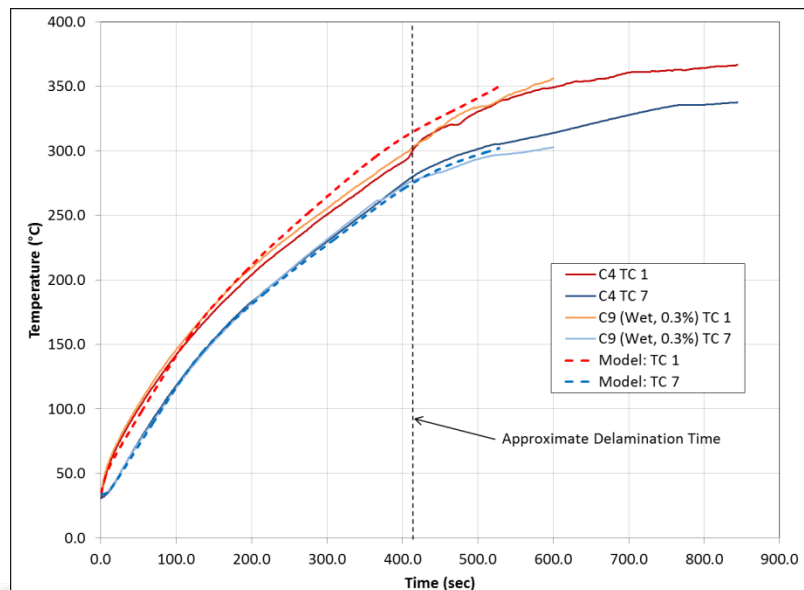


Figure 43. Predicted and Measured Temperatures of IM7/977-3 Exposed to a Heat Flux of 15 kW/m^2

IM7/AFR-PE-4

Tests on plates A2, A3, A8, and A9 were all performed at 35 kW/m^2 and were used to calibrate the model thermal properties for IM7/AFR-PE-4. The resulting model prediction compared to the test data is shown in Figure 44. No other tests were performed at lower heat flux. For a 35 kW/m^2 heat flux input, the model demonstrates close agreement with the test response up to delamination. At about 400°C , both the model and test TC 1 data sharply increase, which likely corresponds to the onset of the primary, more rapid pyrolysis process described by the TGA test data in Section 4.3.4.2. The model predicts the process at a slightly lower temperature compared to the test data, which results in a temporal mismatch of about 20 s. The effect is exaggerated at the relatively low heat flux tested; higher heating rates would result in less time shift and closer matching predictions. The degree of scatter is unknown with the limited data available.

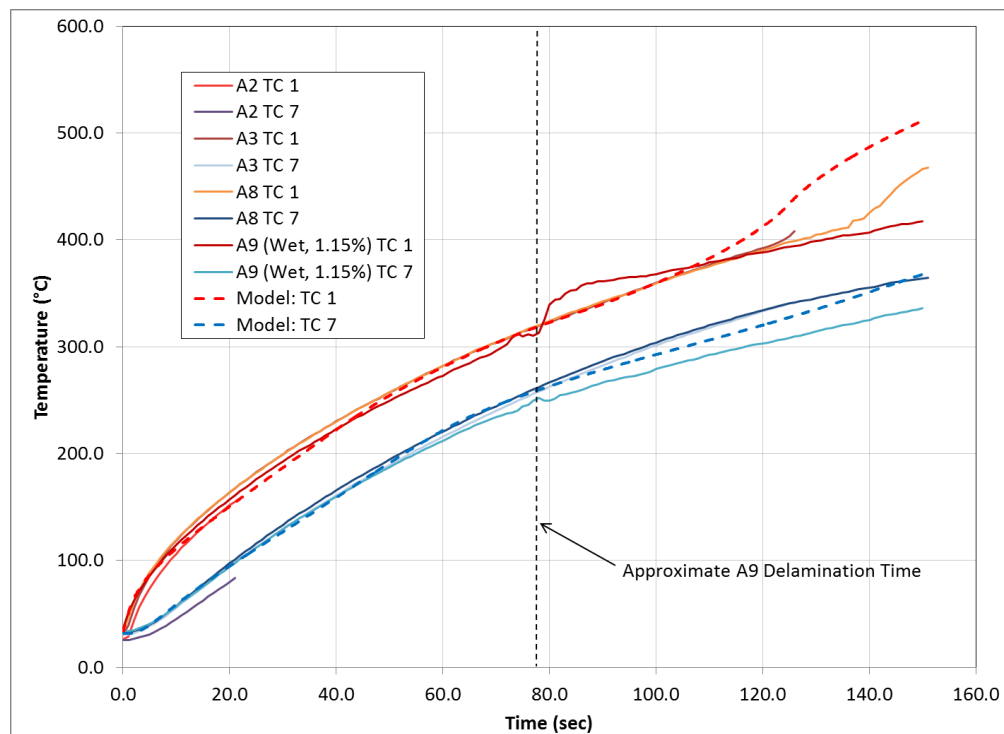


Figure 44. Predicted and Measured Temperatures of IM7/AFR-PE-4 Exposed to a Heat Flux of 35 kW/m^2

4.3.7. Heat Transfer Model Summary

A 1-D heat transfer model suitable for predicting the through-ply temperatures and pyrolysis was developed and calibrated to test data for the three CFRP systems of interest. The model demonstrates good agreement up to the delamination temperature ranges seen during panel heat exposure tests. Due to uncharacterized heat loss at the rear face of the plates tested, the calibrated properties are estimates and should be better characterized using test methods specific to measuring through-thickness thermal conductivity and specific heat in order to improve model predictions for general use [e.g., 26].

The heat transfer model would need further development to predict the post-delamination heat transfer behavior. These improvements would involve two major components: (1) a

thermomechanical model to predict delamination and (2) modification to the heat transfer code to allow for heat transfer across cracks between plies.

To analyze structures in more detail with strong gradients of heat flux across the surface, the thermal damage model developed in this project would need to be integrated into an existing computational 3-D heat transfer code. This is recommended to improve the accuracy of results in general application.

4.4. Prediction of Post-Fire Mechanical Properties

Frequent experimental observations of composites exposed to heat exposures typical of hydrocarbon fires results in two fairly distinct layers: (1) a charred layer where the organic constituents have been decomposed and (2) an undamaged laminate [e.g., 13-17]. There is a 'resin decomposition region' that is relatively small compared to the two distinct layers. These layers are shown in Figure 45 for a glass/polyester woven roving laminate. There is evidence of some damage to the 'undamaged' laminate in the form of matrix cracks and delaminations close to the decomposition region. It is important to note that in these tests the composite panels were exposed to radiant heating that led to ignition on the heat-exposed surface of the composite.

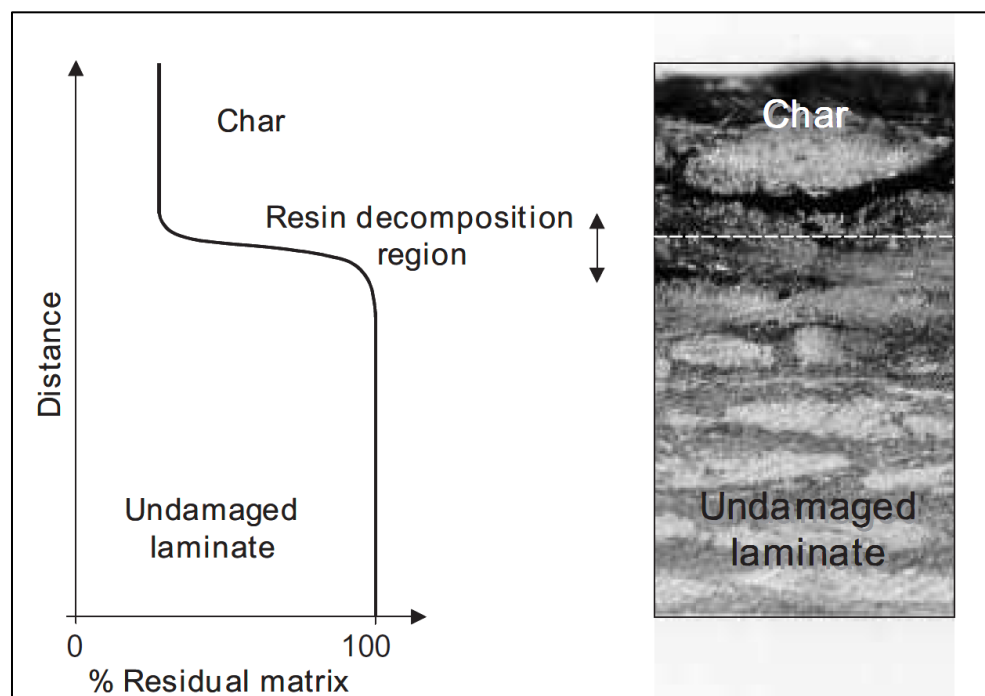


Figure 45. Schematic of Resin Degradation Through Laminate, with Resin Decomposition Zone and Residual Char, Alongside a Cross-Section Through a Glass/Polyester Woven Roving Laminate Exposed to a Heat Flux of 50 kW/m² [13]

To predict the post-fire mechanical response of single skin, flat composite laminates Mouritz and Mathys [14-17] proposed a simple two-layer model, one for the thermally affected region to have reduced or zero mechanical properties and a completely undamaged region with room temperature mechanical properties. The resin decomposition region is not considered to have

degraded properties. They demonstrate that such a model is reasonably accurate for a variety of glass and carbon fiber composites in tension, compression and flexure. The same assumption is made in this study to predict the post-fire mechanical response for the composite materials of interest.

The effect of a fire on specific composite structural designs can be quite complicated depending on the layup that is used and the design loads for the structure. A design may be driven by particular loadings and failure modes. This may be particularly true for layups that are highly asymmetric post-fire where significant axial-bending and axial-torsional coupling may occur. A robust analysis of fire damage would require FE analysis of the degraded structure to determine how much a structure was degraded as compared with its design loads. However, in order to provide general predictions on the reduction in mechanical strength and stiffness of composite structures, as is the objective of this study, they can be generalized by providing predicted reductions in the tensile, flexural and compressive strength and stiffness in terms of their so-called in-plane and flexural ‘Engineering Constants’.

In-plane engineering constants are

$$E_1^o = 1/a_{11}^*, \quad E_2^o = 1/a_{22}^*, \quad E_6^o = 1/a_{66}^*.$$

The flexural engineering constants are

$$E_1^f = 1/d_{11}^*, \quad E_2^f = 1/d_{22}^*, \quad E_6^f = 1/d_{66}^*.$$

The a_{ij}^* and d_{ij}^* , $i = 1, 2, 6$, are defined as the axial and flexural compliance matrices for a symmetric laminate, where from laminate plate theory

$$\begin{Bmatrix} \varepsilon_i^o \\ \varepsilon_i^f \end{Bmatrix} = \begin{bmatrix} a_{ij}^* & 0 \\ 0 & d_{ij}^* \end{bmatrix} \begin{Bmatrix} \sigma_i^o \\ \sigma_f^o \end{Bmatrix}.$$

The $\{\sigma^o\} = 1/h \{N\}$, where the $\{N\}$ are the in-plane loads on a laminate and h is the thickness.

The $\{\sigma_f^o\} = 6/h^2 \{M\}$, where $\{M\}$ are the moments on the laminate. The $\{\varepsilon^o\}$ are in-plane strains and the $\{\varepsilon^f\} = h/2 \{k\}$ are flexural strains where $\{k\}$ are the curvatures.

In general, engineering constants for asymmetric laminates are not strictly defined and difficult to measure because of the coupling between in-plane and flexural deformations. However, for laminates with many repeated sub-laminates (i.e., a laminate with a repeated stacking sequence) the asymmetry is small and the engineering constants are approximately correct.

With application to the fire exposure experiments in this study, the quasi-isotropic 24-ply (0,90,45,-45)_{3s} laminates are symmetric. However, when exposed to fire they become asymmetric. This asymmetry is weak for small char depths, but becomes more significant if a large amount of the ply thickness is degraded. Since the use of many sub-laminates is in common use throughout the composite structures industry, this approximation is also appropriate for making high-level general assessments for the effect of fire exposure on composite structures.

This approach was implemented in this effort through modification of a progressive damage growth computer code for laminated composites, the Composite Material Analysis Program (CMAP). CMAP is based on classical linear plate theory and classical composite lamination theory [29] with a progressive damage methodology based on the work of Chang and Chang [30]. In the existing version of the code, ply-level properties and stacking sequence are entered into the code to determine the engineering stiffness values and failure.

This code was modified by allowing for input of the predicted char depth results from the 1-D heat transfer analyses and degrading the mechanical properties of the charred plies. A linear degradation of properties is assumed where intact plies have non-degraded properties and complete mechanical degradation occurs at a user-specified level of pyrolysis that can be calibrated with mechanical test results in tension and flexure.

Modification of CMAP for this application was not fully completed. As will be described in the following section, the composite plates tested in this effort experienced sudden and catastrophic delaminations prior to any significant charring. The charring mode of damage was not significant for the test conditions, so modifications to CMAP were not completed in order to focus on the experimental results.

There are currently no models that can predict the thermally-induced delaminations seen in the experiments. Therefore, prediction of the mechanical degradation of the material as a function of time cannot currently be performed with the desired accuracy. A thermodynamic-mechanical model to predict delamination initiation and growth in general structural laminates is needed before a complete analysis can be performed.

5. RESULTS AND DISCUSSION

The average heat flux applied to each composite plate is shown in Table 5 for the exposure durations listed. Also provided are the moisture content, maximum temperatures recorded from the embedded TCs, the percentage mass loss of the entire plate and a summary of the physical changes to the plate.

Table 5. Composite Plate Heat Exposure Summary

Sample	Avg. Heat Flux (kW/m ²)	Exposure Time (sec)	Moisture Content (%)	Max Int. Temp (°C)	Mass Loss (%)	Physical Observations
IM7/977-3						
C4	15.2	844	Dry	367	2.10%	smoked heavily; popped and crackled; about 50% of top surface bubbled; slits formed on top and back face; stuck to edge insulation
C9	15.4	601	0.3%	356	1.04%	smoked slightly, popped and crackled; about 10% of top surface bubbled; slits formed on top, no damage on back face; stuck to edge insulation
IM7/R3002						
R2	26.2	214	Dry	401	1.15%	smoked moderately; popped and crackled; about 50% of top surface bubbled; back face not inspected; stuck to edge insulation
R3	24.9	91	Dry	271	0.06%	no visible damage
R4	14.9	151	Dry	240	0.03%	no visible damage
R6	34.2	101	Dry	367	0.42%	smoked moderately; popped and crackled; about 40% of top surface bubbled; back face not inspected
R7	15.2	201	Dry	274	0.03%	no visible damage
R8	15.3	1040	Dry	382	1.63%	smoked slightly; popped and crackled; about 5% of top surface bubbled; back face not inspected; stuck to edge insulation
R9	25.9	201	0.4%	392	1.38%	smoked moderately; popped and crackled; about 50% of top surface bubbled; no damage on back face; plate warped; stuck to edge insulation
IM7/AFR-PE-4						
A2	34.0	20	Dry	155	0.00%	no visible damage
A3	34.1	127	Dry	411	0.18%	smoked slightly; popped and crackled; about 30% of top surface bubbled; no damage on back face; plate warped
A8	35.1	151	Dry	468	0.23%	smoked slightly; popped and crackled; about 60% of top surface bubbled; no damage on back face; plate warped
A9	35.2	152	1.15%	417	1.13%	smoked slightly; popped forcefully; about 20% of top surface bubbled; slits formed on top, no damage on back face; plate warped

5.1. Physical Damage Evaluation

Physical damage to the composite plates during heat exposure, as well as the plate response itself, was documented with regular video, infrared video, and post-test imaging, sectioning and microscopy. Plates that showed little to no mechanical degradation after heat exposure showed no visual evidence of damage, aside from small discoloration on the exposed surface in a few cases. Microscopy of sectioned samples showed no delamination or charring of the materials.

In all materials and heat flux magnitudes tested where there was mechanical degradation measured, it was found that the composite plate experienced sudden damage, prior to any significant charring or mass loss, in the form of delaminations, sometimes throughout the entire thickness. The general sequence observed during testing was that no physical response, including little or no smoking, was evident up to the time where surface bubbling formed (localized raised regions of the material), indicating delamination initiation. The plate would then bend upward,

many times exhibiting audible cracking. The plate would then dynamically rebound to some degree, indicating further delamination, many times showing permanent curvature after the test. This sequence would occur quickly, in typically less than 10 s. In no case did ignition of the plate occur.

Infrared imaging of the plates immediately following removal from the heat source show uneven cooling of the plate surface, as would occur with delaminated regions. Images typically showed a few large and many small regions with greater cooling than surrounding material. Most regions of greater cooling were away from the edges of the plate, indicating that edge delamination was not the likely cause of initiation. The larger regions sometimes showed swelling after the plate completely cooled. These observations indicate that some delaminations grew to cover large regions of the plate, as later observed in plate sectioning.

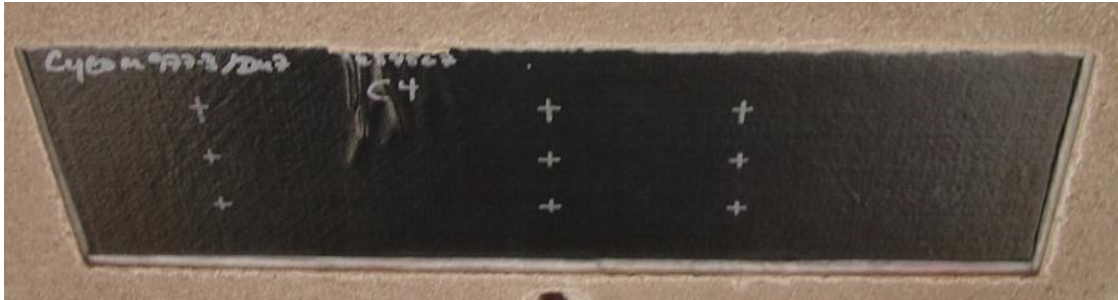
Optical microscopy was performed on all samples cut from the exposed plates. Widespread delaminations were evident throughout the thickness of the plates showing mechanical degradation. There was no apparent pattern to where the delaminations occurred. Large widespread delaminations were seen throughout the thickness in the IM7/RM3002 and IM7/977-3 composites, but only on the plies on the heat exposed side of IM7/AFR-PE-4. Only small delaminations were seen on the unexposed side of this material. It is obvious that delaminations seen by the visual surface bubbling of the plates during testing were caused by the application of heat. However, it is possible that some of the delaminations throughout the thickness were also caused by the mechanical stresses caused by plate bending.

It is postulated that high pressure gases in the plate from water vapor and resin outgassing, coupled with the reduction of the interlaminar strength at elevated temperatures, are the cause for the sudden delamination observed in experiments. Once a small crack initiates, strong thermal gradients are produced since heat transfer across an open crack is much smaller than through intact material. The corresponding thermal stresses drive the delamination further. This mode may not occur when the materials are exposed to a much higher heat flux, such as from ignition and burning of volatiles on the composite surface or direct flame impingement from a fuel fire. This high heat flux causes pyrolysis at the surface, creating an avenue for internal gases to escape through the remaining fibers rather than building up pressure.

The following sections provide some of the results from this study. Images were selected to demonstrate the representative damage seen in each material at each exposure level. All cross-sectional images are oriented with the heat exposed side up.

5.1.1. IM7/977-3

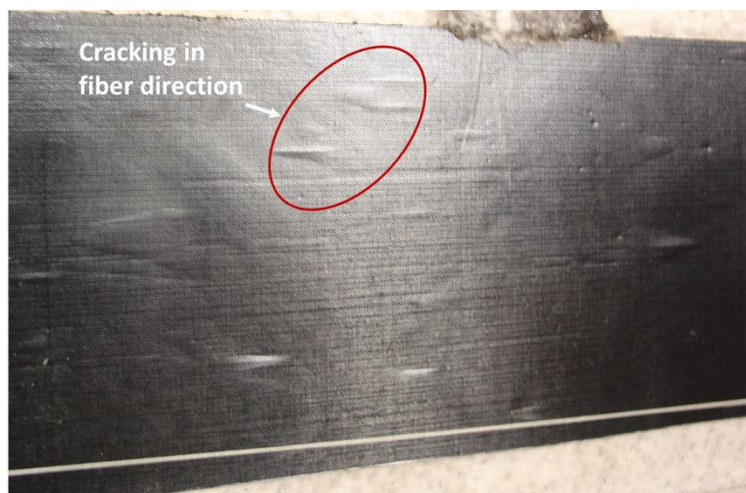
Images of IM7/977-3 composite plates C4 and C9 before and after heat exposure are shown in Figure 46 and Figure 47. Both plates were tested at the same heat flux. Plate C4 was tested dry and C9 at 0.3 percent moisture content for 200 s less than the dry plate. Surface damage on both plates included discoloration and multiple raised regions on the heat-exposed surface. There were also one to two-inch long cracks running in the surface ply fiber direction on the back (insulated) surface of plate C9 and both faces of C4.



(a) Front - Prior to testing



(b) Front – after heat exposure

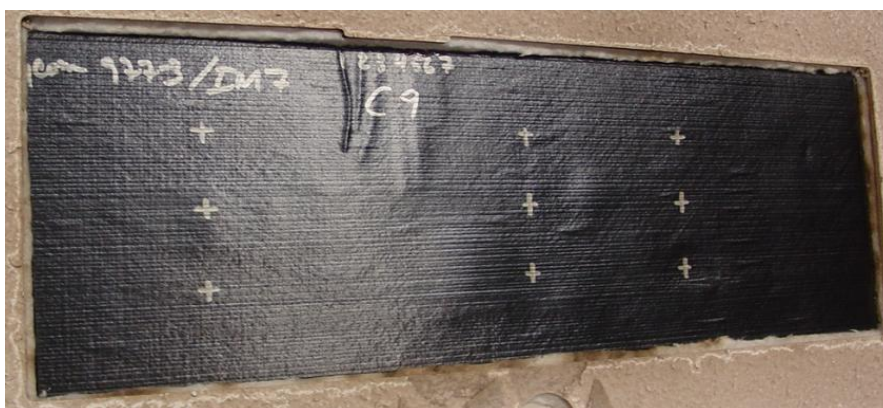


(c) Back – after heat exposure

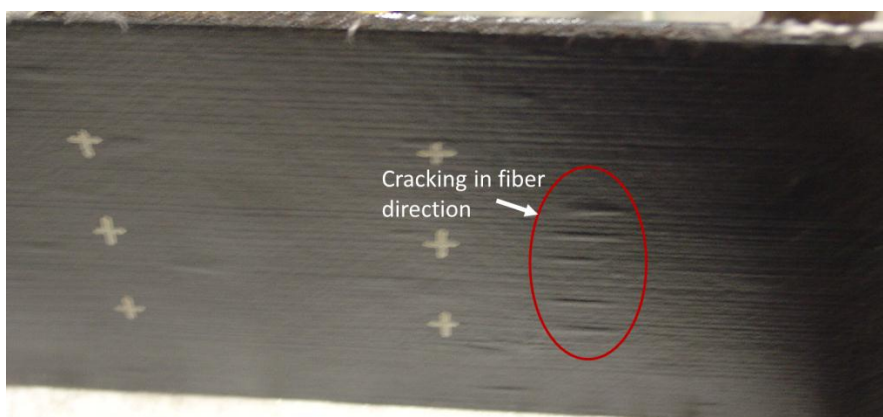
Figure 46. Plate C4 Before (a) and After Exposure at 15.2 kW/m^2 for 844s (b & c)



(a) Front - Prior to Testing



(b) Front – After Heat Exposure



(c) Front – After Heat Exposure

Figure 47. Plate C9 (0.3 Percent Moisture Content) before (a) and After Exposure at 15.4 kW/m² for 601s (b & c)

This type of cracking was also evident on the front (heat exposed) side, but to a lesser extent in the dry plate, C4. Infrared images of these plates shortly after removal from the heater are shown in Figure 48 and Figure 49. Note that the raised regions shown in the photographs are seen as cooler regions in the IR images, indicating that these are delaminated areas that cool more quickly when removed from heat. Delaminated areas cool faster because these regions are thin layers of material separated from adjacent layers.

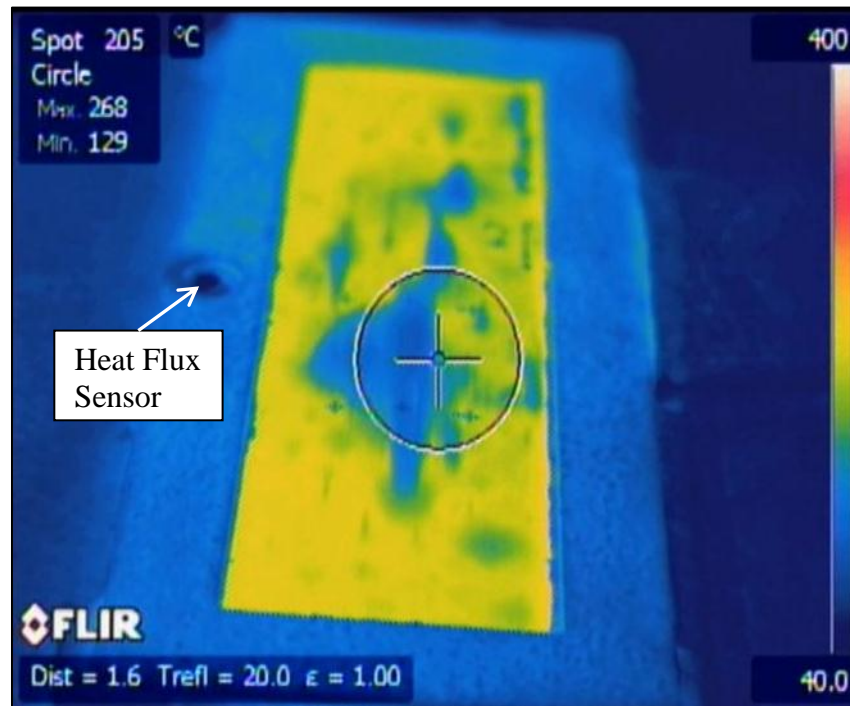


Figure 48. IR Image of C4 Approximately 20 s after Removal from Heat Source

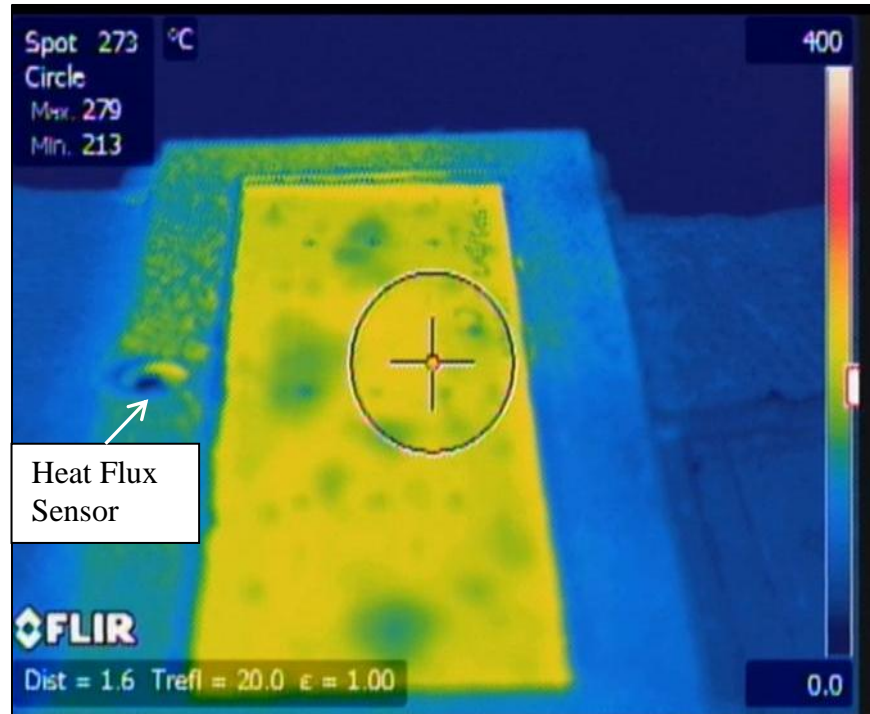


Figure 49. IR Image of C9 (0.3 Percent Moisture Content) Approximately 8 s after Removal from Heat Source

A cross section of the material prior to any heat exposure is shown in Figure 50. It shows good consolidation with no evidence of large voids or pre-existing delaminations. Cross sections of the heat-exposed plates are shown in Figure 51 and Figure 52. Small and large delaminations are seen through the thickness of the plate. There is no apparent pattern with regard to the extent of delaminations towards the hot or cooler side of the plate.

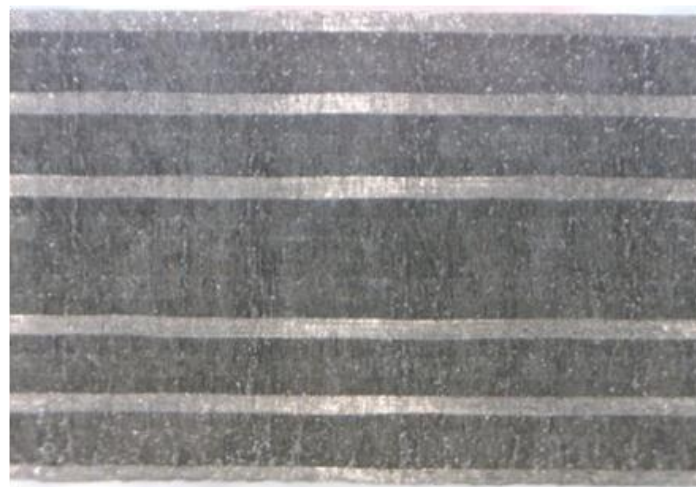


Figure 50. Cross-Section of IM7/977-3 Plate after Being Cut with a Water-Jet

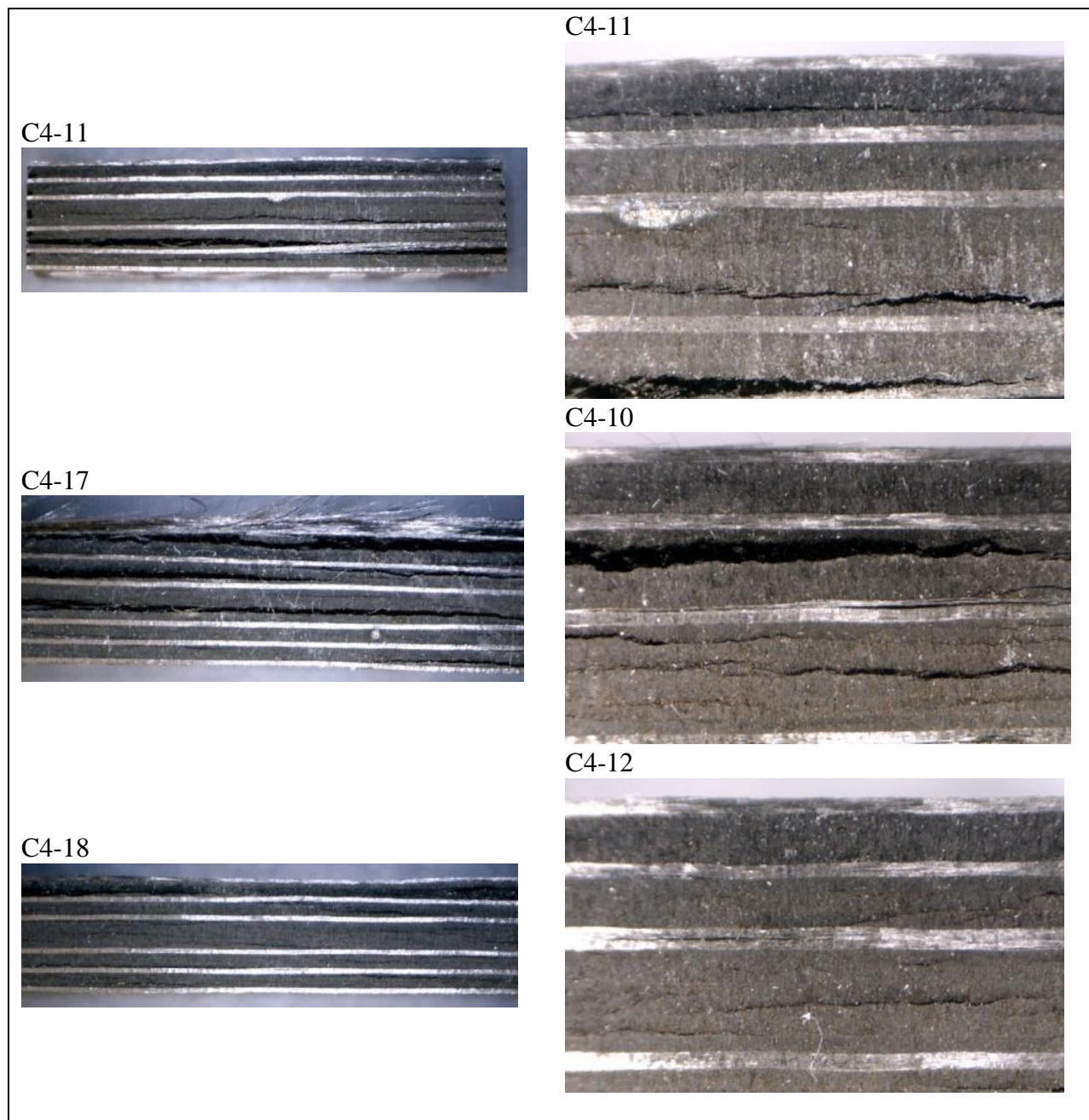


Figure 51. Cross Section of Plate C4 - Exposed at 15 kW/m² for 844s

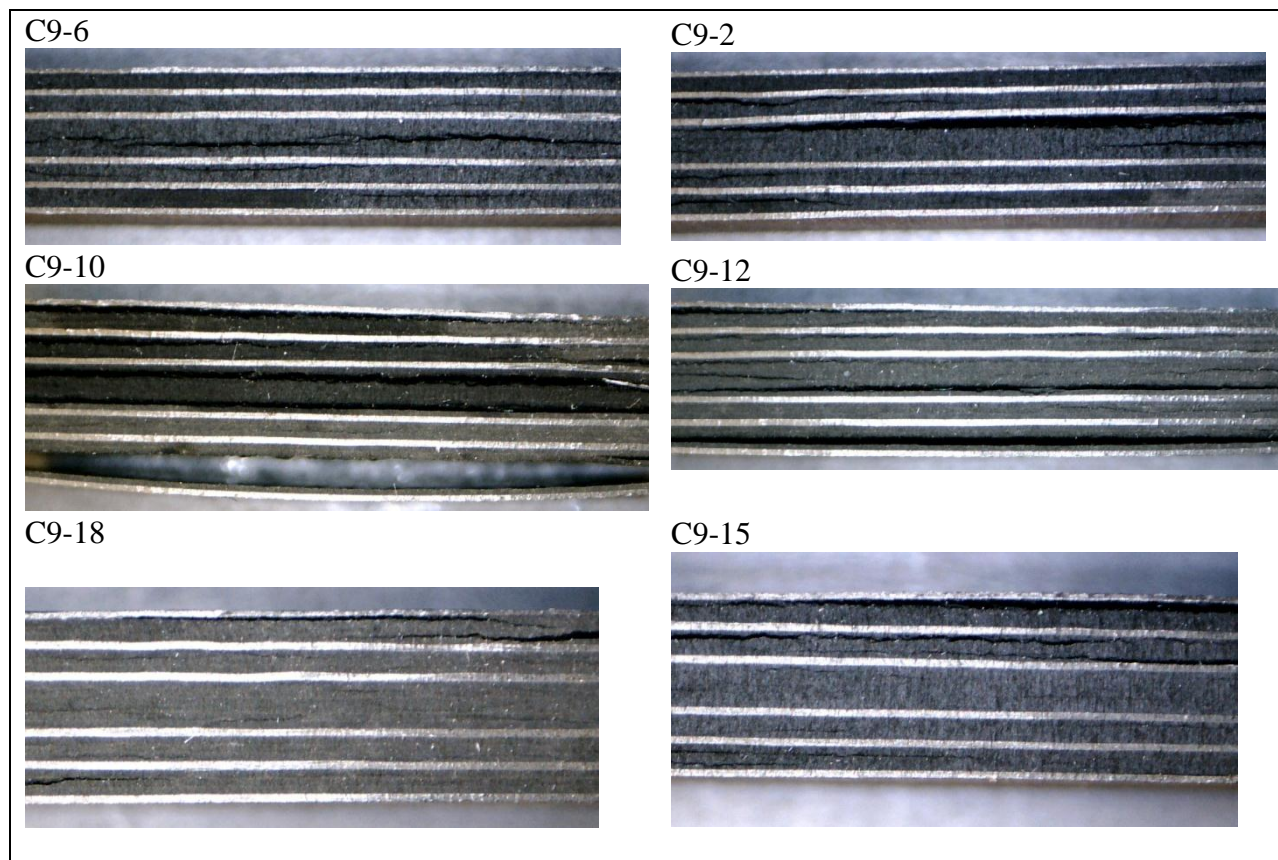


Figure 52. Cross section of plate C9 (0.3 percent moisture content) - Exposed at 15.4 kW/m² for 601 s

5.1.2. IM7/RM3002

Observed damage to the IM7/RM3002 composite plates before and after heat exposure are shown in Figure 53 to Figure 59. Surface damage on these plates included discoloration and, in some cases, multiple raised regions on the heat-exposed surface. No cracking in the fiber direction was seen, as in the IM7/977-3 plates. Note that there is little apparent heat damage in plates that did not delaminate. For example, plate R2 delaminated after approximately 125 s exposure to 26 kW/m² and showed significant damage (Figure 54). Plate R3 was exposed for 91 s at 25 kW/m² and did not delaminate and shows only slight discoloration (Figure 55). Plate R8 was exposed to the lowest heat flux (15 kW/m²) and showed the least topical discoloration and no permanent topical swelling yet still exhibited significant delaminations through the thickness (Figure 60). This is likely because the low heat flux allowed time for heat to conduct around delaminated regions. Plies on the exposed side of the delaminated regions did not increase temperature as rapidly as with the higher heat flux. With higher heat flux, the higher temperatures lead to more significant localized damage to the front face plies in the delaminated areas.

Infrared images of these plates shortly after removal from the heater are shown in Figure 60 and Figure 61. Note that the raised regions shown in the photographs are seen as cooler regions in the

IR images, indicating that these are delaminated areas that cool more quickly when removed from heat.

A cross section of the material prior to any heat exposure is shown in Figure 62. It shows good consolidation with no evidence of large voids or pre-existing delaminations. Cross sections of the heat-exposed plates are shown in Figure 63 to Figure 67. When delaminations occurred, small and large delaminations are seen through the thickness of the plate. Note small delaminations between plies in polished samples not readily seen in the water-jet cut surface (e.g., Figure 65). There is no apparent pattern with regard to the extent of delaminations towards the hot or cooler side of the plate. This is true in both dry samples and with moisture (cf. plate R2 in Figure 63 and R9 in Figure 67). No damage is seen in plates that did not delaminate (Figure 64).

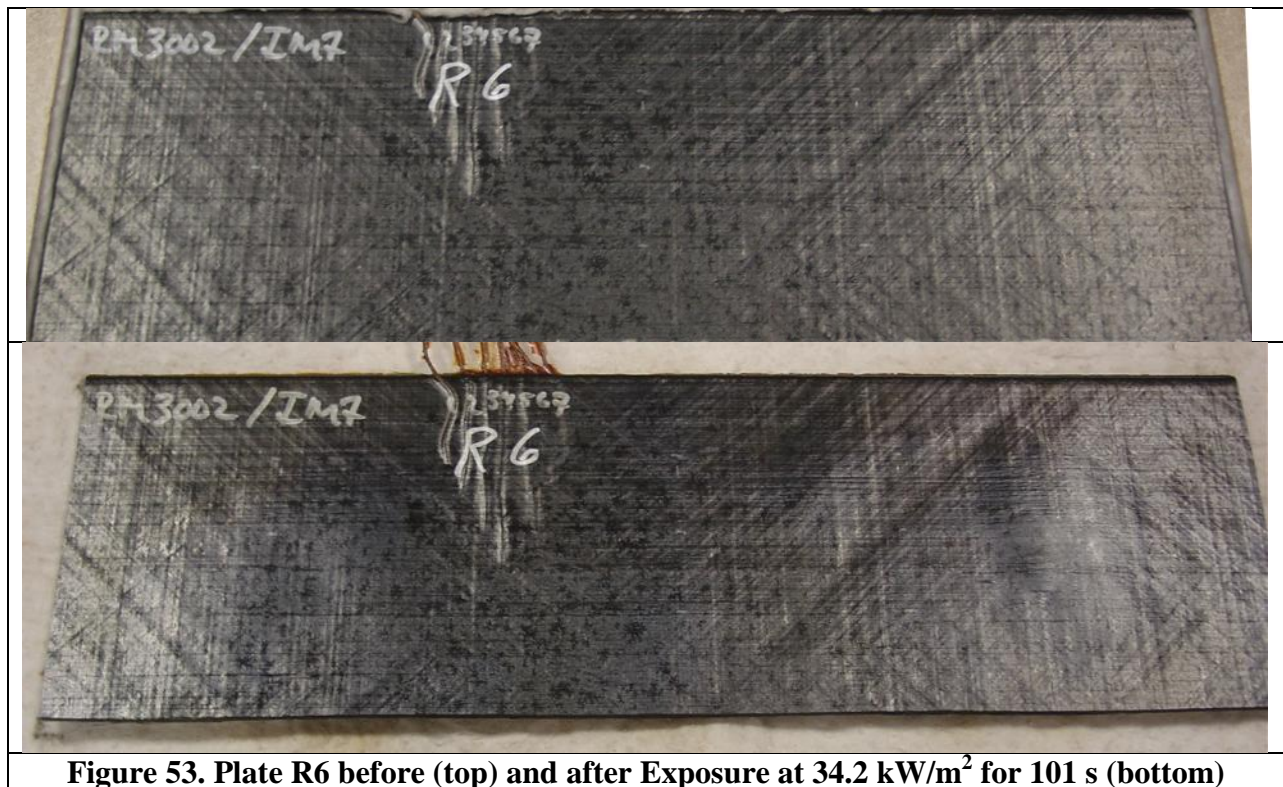


Figure 53. Plate R6 before (top) and after Exposure at 34.2 kW/m² for 101 s (bottom)

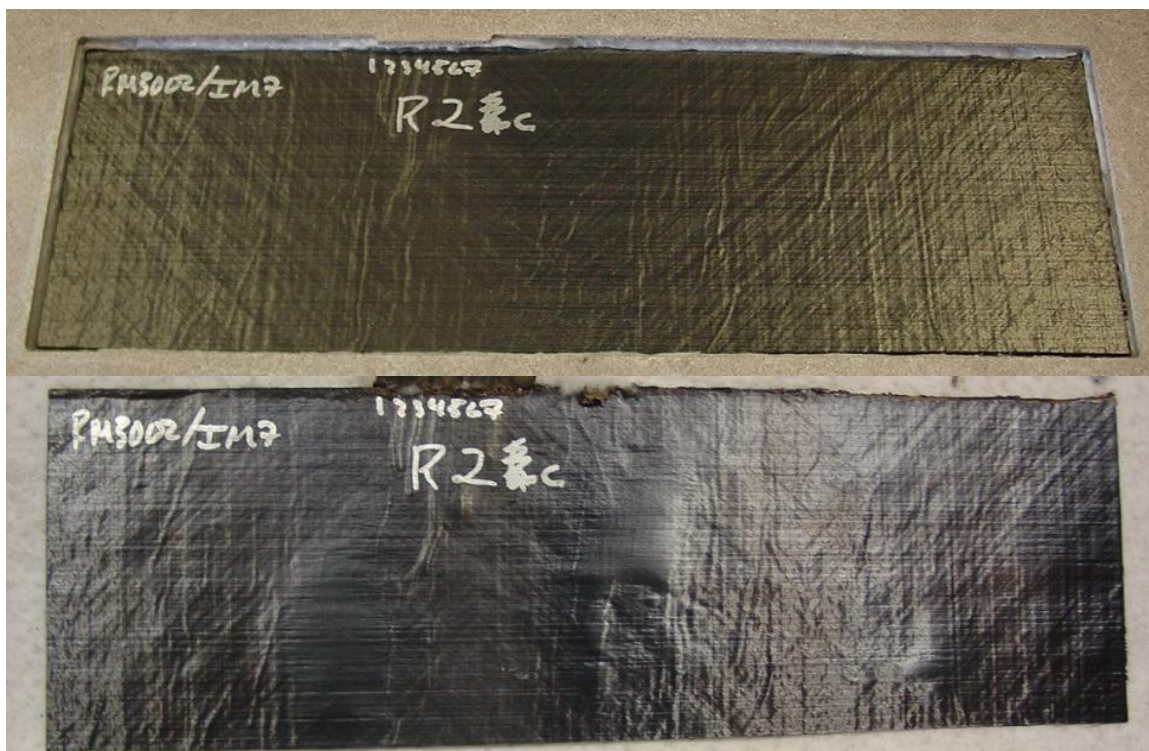


Figure 54. Plate R2 before (top) and after Exposure at 26.2 kW/m^2 for 214 s (bottom)

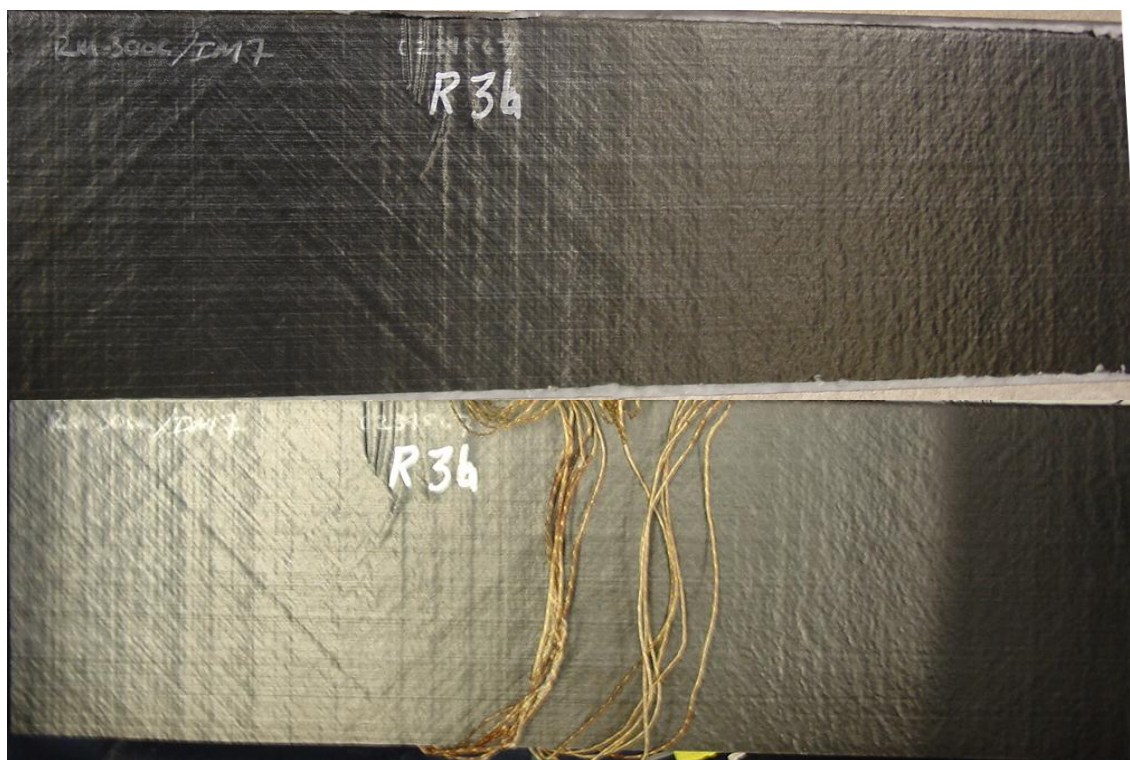


Figure 55. Plate R3 before (top) and after Exposure at 24.9 kW/m^2 for 91 s (bottom)

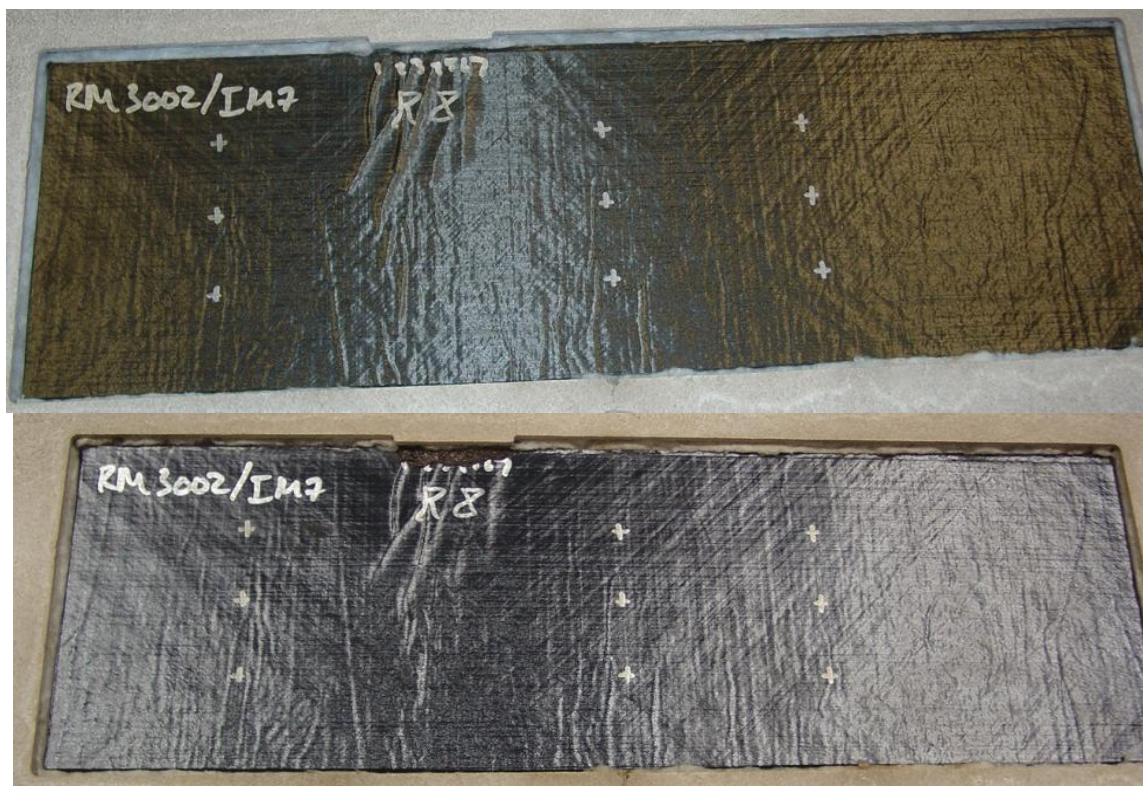


Figure 56. Plate R8 before (top) and after Exposure at 15.3 kW/m^2 for 1040 s (bottom).

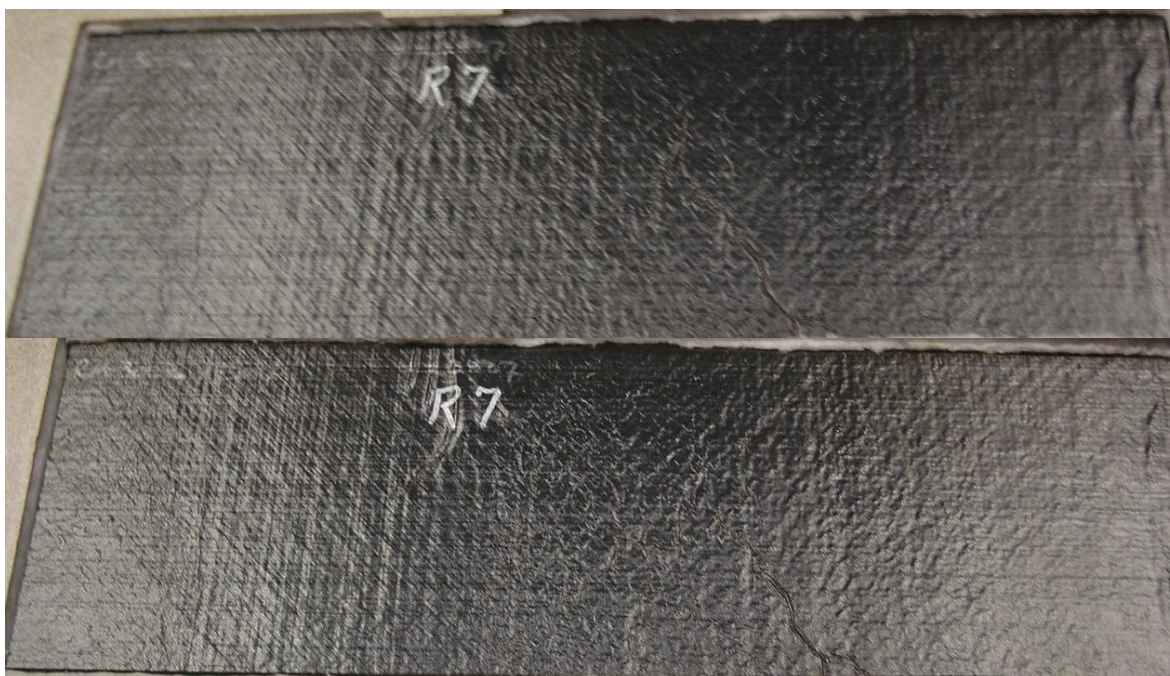


Figure 57. Plate R7 before (top) and after Exposure at 15.2 kW/m^2 for 201 s (bottom)



Figure 58. Plate R4 before (top) and after Exposure at 14.9 kW/m^2 for 151 s (bottom)



Figure 59. Plate R9 (0.4 percent Moisture Content) before (top) and after Exposure at 25.9 kW/m^2 for 201 s (bottom)



Figure 60. IR image of R8 Approximately 8 s after Removal from Heat Source

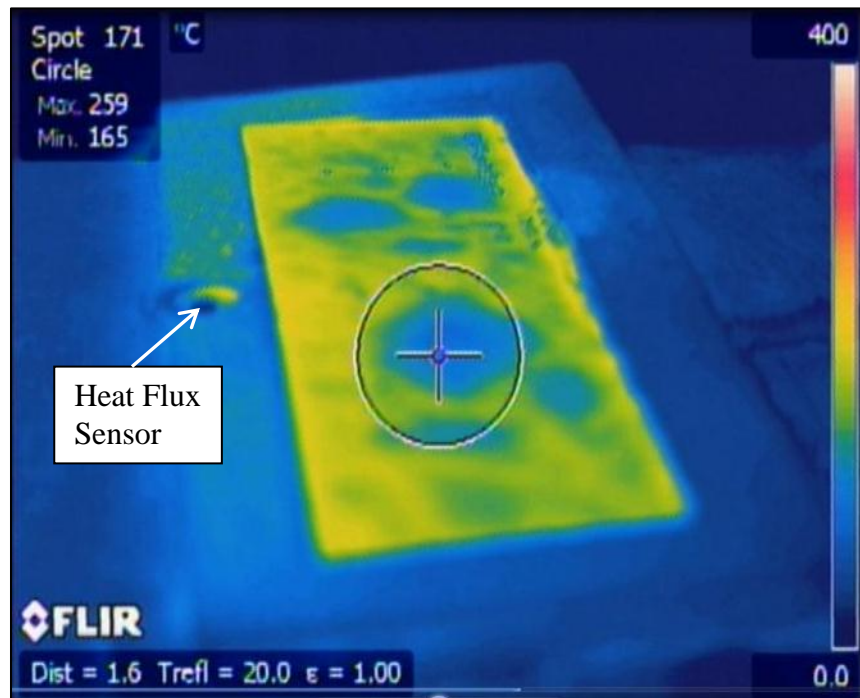


Figure 61. IR image of R9 (0.4 percent Moisture Content) Approximately 30 s after Removal from Heat Source



Figure 62. Cross-section of IM7/RM3002 Plate after being Cut with a Water-jet

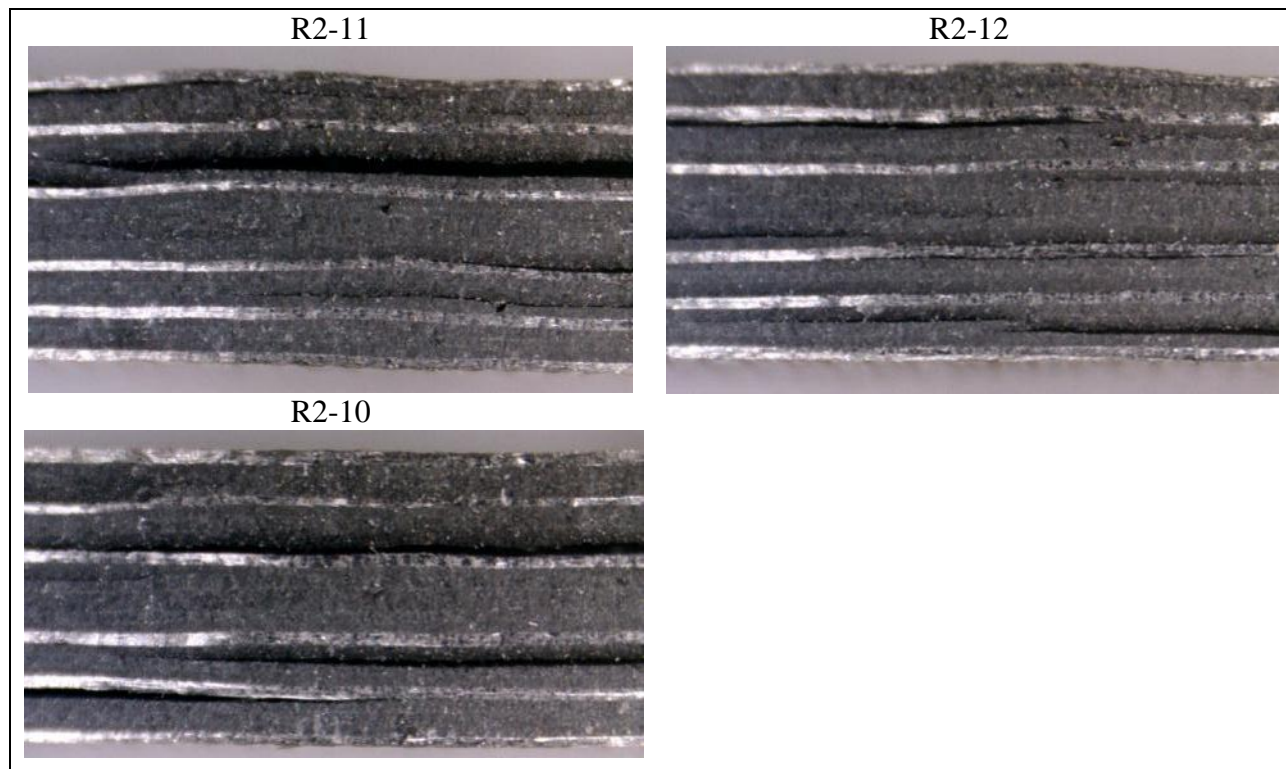


Figure 63. Cross section of Plate R2 – Exposed at 26.2 kW/m^2 for 214 s

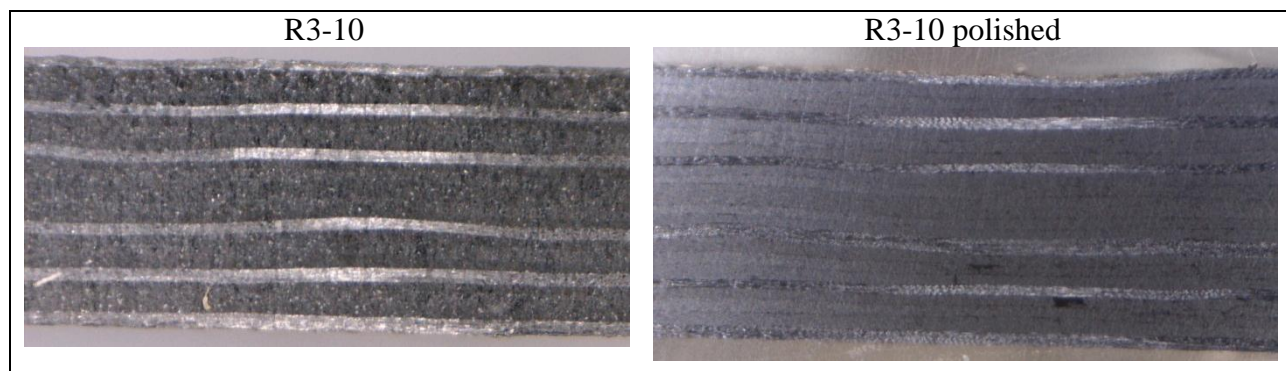


Figure 64. Cross section of Plate R3 – Exposed at 24.9 kW/m^2 for 91 s

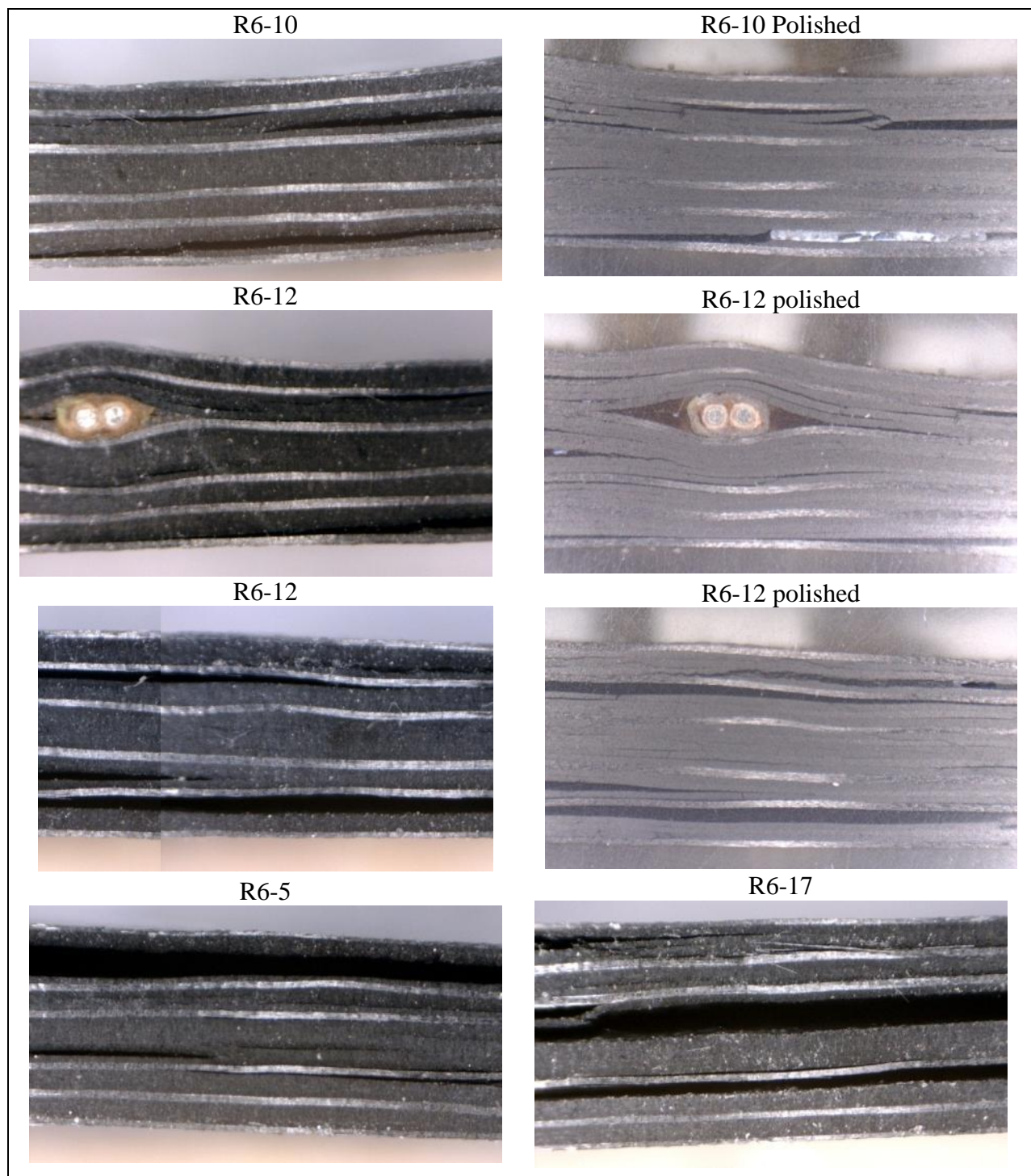


Figure 65. Cross section of Plate R6 - Exposed at 34.2 kW/m² for 101 s

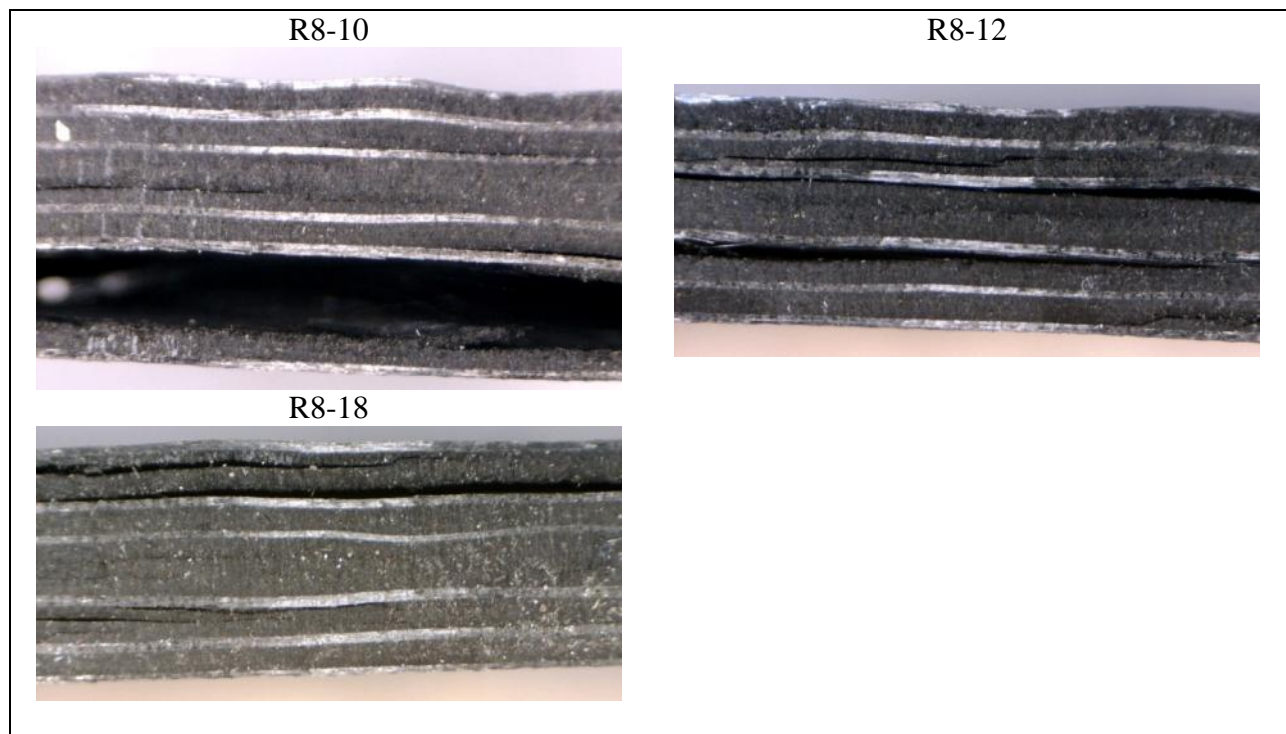


Figure 66. Cross section of Plate R8 – Exposed at 15.3 kW/m² for 1040 s

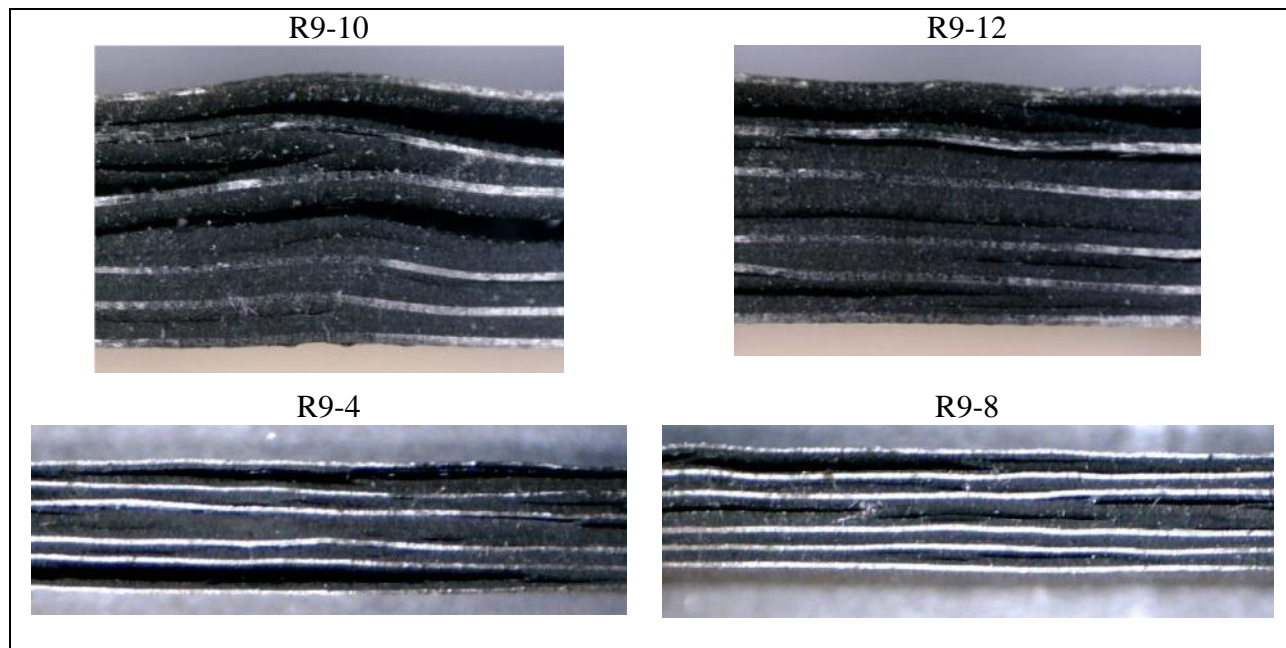


Figure 67. Cross section of Plate R9 (0.4 percent Moisture Content) - Exposed at 25.9 kW/m² for 201 s

5.1.3. IM7/AFR-PE-4

Images of IM7/AFR-PE-4 composite plates before and after heat exposure are shown in Figure 68–Figure 71. Surface damage on these plates included discoloration and, in some cases, multiple raised regions on the heat-exposed surface. Plate A9, with a moisture content of 1.4 percent, displayed cracks in the fiber direction on the front face (Figure 71). These cracks had a raised region around them, indicating that they may be the result of the release of pressure through this crack. For this reason, they will be referred to here as a burst crack. Plate A3 began to buckle upward just as it was removed from the heat source. This evidence, along with the thermal data presented in the next section, indicates that the plate was removed from heat just as delaminations began to grow in the plate. Plate A8 was tested 24 s longer under the same heat flux and showed the same swelled or raised regions typical of delaminated areas as in A3 (cf. Figure 69 and Figure 70).

Infrared images of these plates shortly after removal from the heater are shown in Figure 72 to Figure 74. Note that the raised regions shown in the photographs are seen as cooler regions in the IR images, indicating that these are delaminated areas that cool more quickly when removed from heat.

A cross section of the material prior to any heat exposure is shown in Figure 75. Although there are no pre-existing delaminations, there are large voids in the material especially in the plies towards the back of the plate (insulated side). After trimming the AFR-PE-4 and viewing the cross section, the voids were noticed. The void content appears significant, but was not directly measured. Estimates by the manufacturer from photographs, determined that the material met requirements. Manufacturing factors that can affect void content include trapped solvent, water and methanol condensing during cure. The 24-ply thickness of our samples made solvent and condensation product removal difficult.

Cross sections of the heat-exposed plates are shown in Figure 76–Figure 79. Small and large delaminations are seen through the thickness of the plates in both wet and dry conditions. In this material, the extent of the delaminations appear to be largest on the top (exposed) surface, but smaller cracks are also seen around void regions and ply interfaces throughout the thickness. These smaller cracks are evident even without the large delaminations in the top plies.

Video of the heat exposure test on plate A9 was used to document the plate response sequence. Still images were taken at key times during the sequence, as shown in Figure 79. No response is seen in the plate up to 70 s. At 70 s, the plate begins to warp upwards. Bubbling of the surface is seen at 76s with a rapid evolution of these delaminations over the next 3 s. An audible cracking was heard at 79 s followed by a sudden rebound of the plate that actually damaged the insulating material surrounding the plate. After this time, there is little plate response aside from slight smoking up to 140 s when the plate permanently warped.

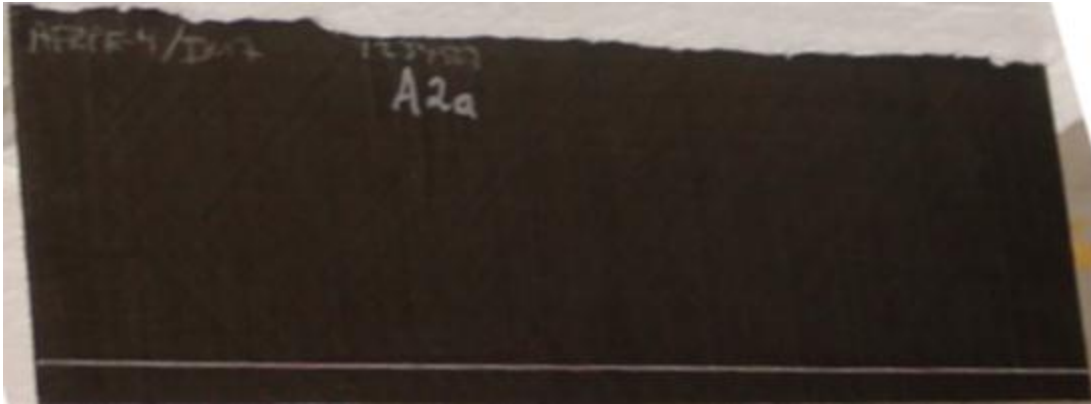


Figure 68. Plate A2 after Exposure at 36.5 kW/m² for 20 s

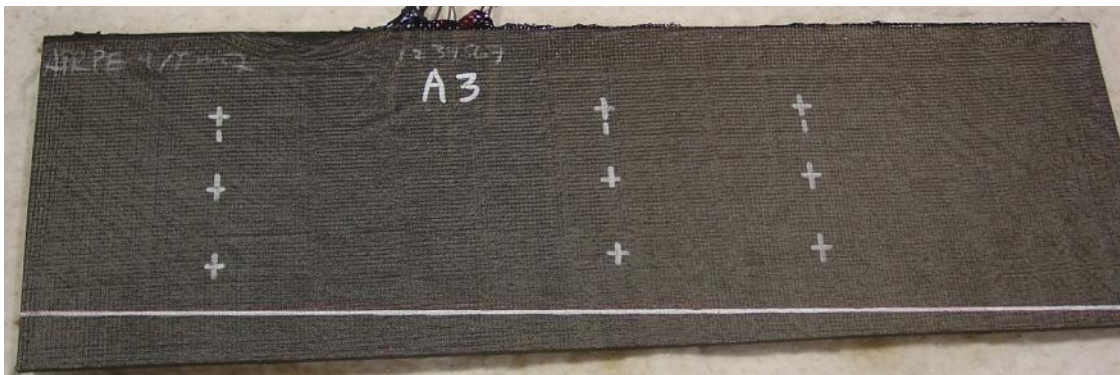


Figure 69. Plate A3 before (top) and after Exposure at 34.1 kW/m² for 127 s (bottom)

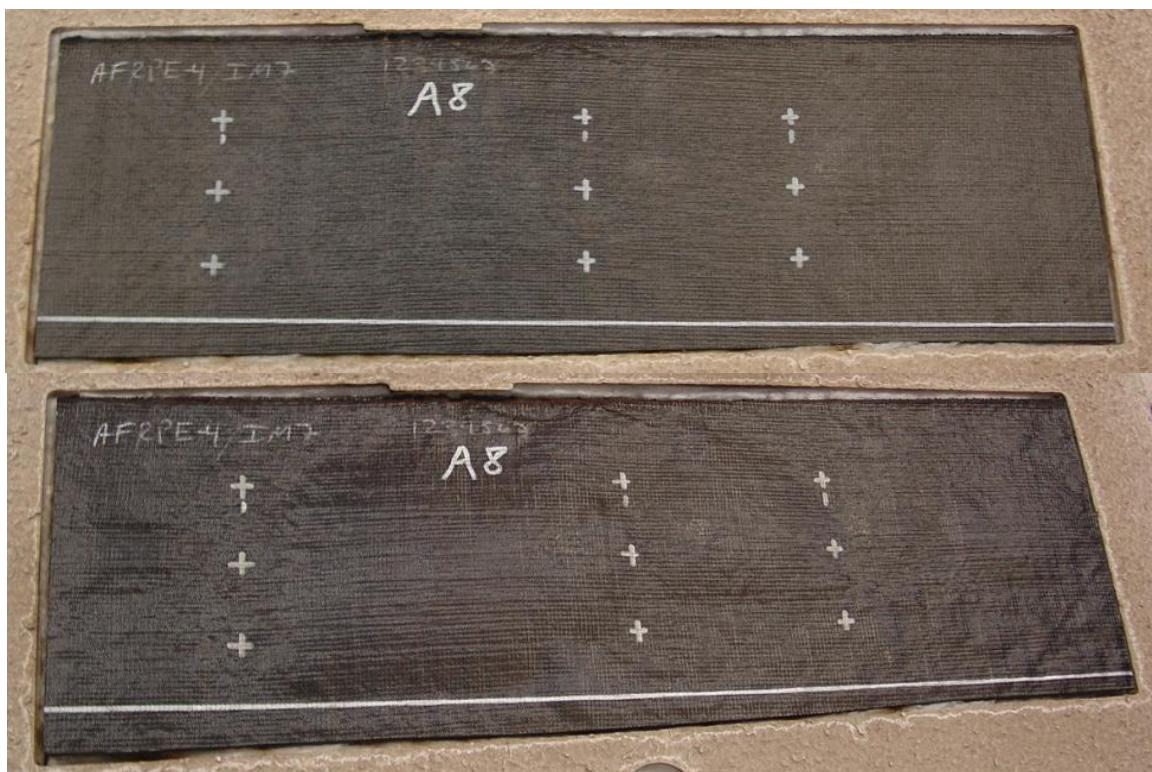


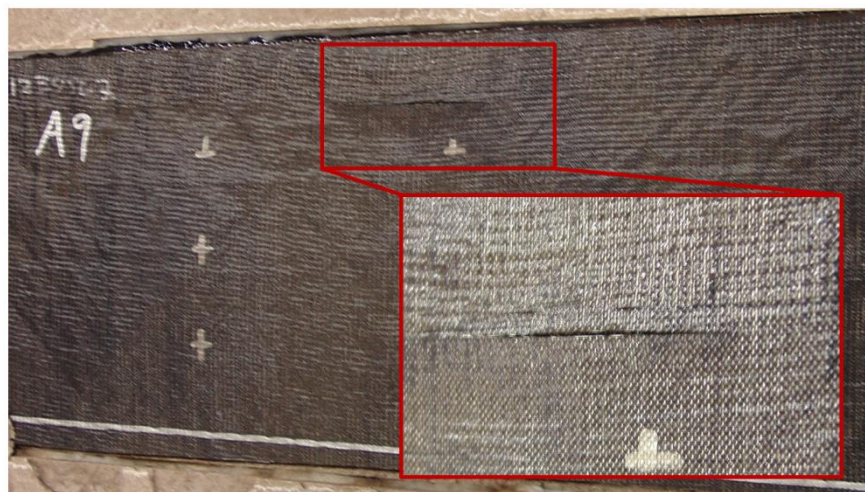
Figure 70. Plate A8 before (top) and after Exposure at 35.1 kW/m² for 151 s (bottom)



(a) Front - Prior to testing



(b) Front – after heat exposure



(d) Front – after heat exposure showing burst crack

Figure 71. Plate A9 (1.15 percent Moisture Content) before (top) and after Exposure at 35.2 kW/m^2 for 152 s (bottom)

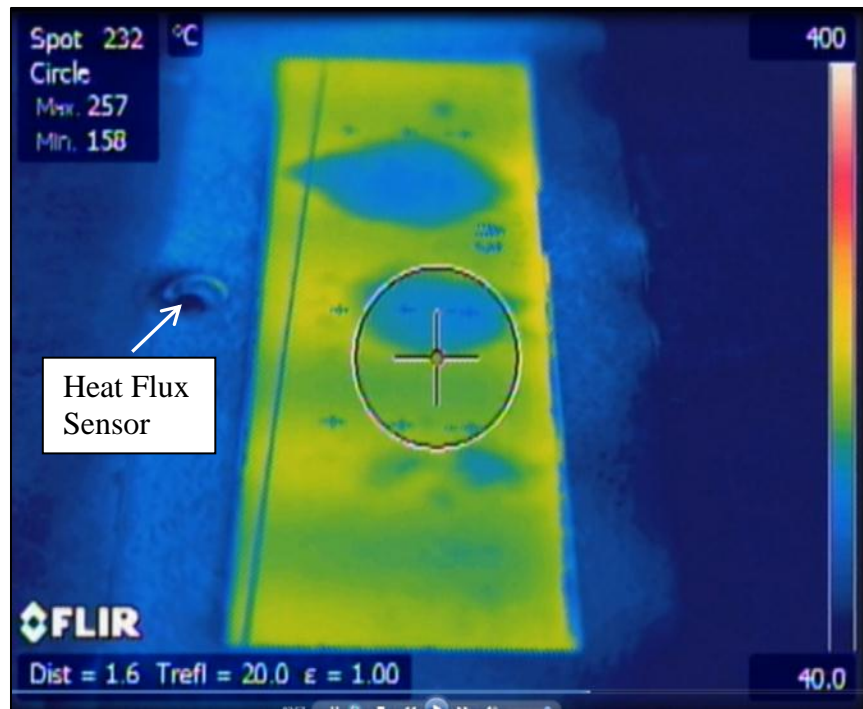


Figure 72. IR image of A3 Approximately 50 s after Removal from Heat Source

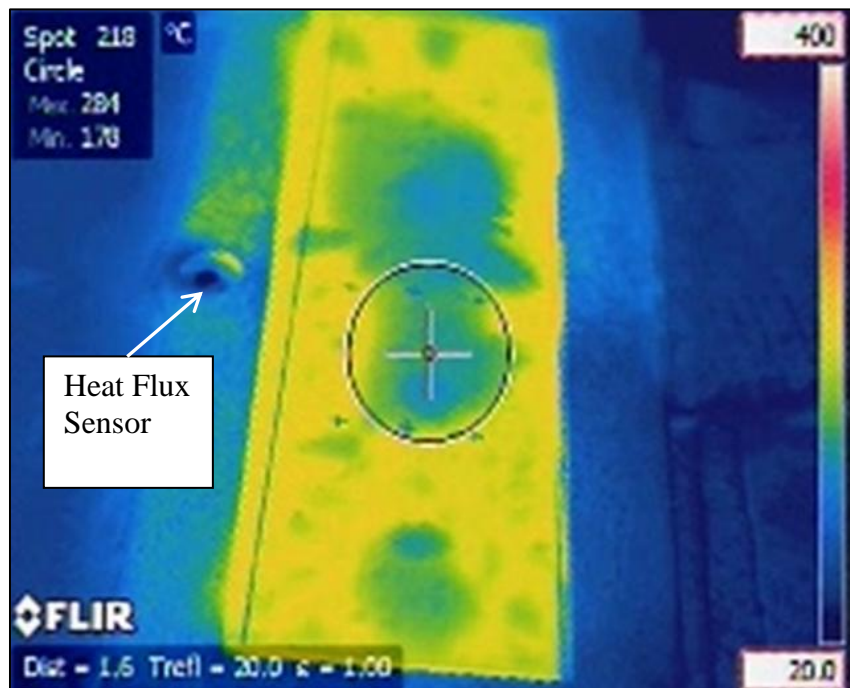


Figure 73. IR image of A8 Approximately 40 s after Removal from Heat Source

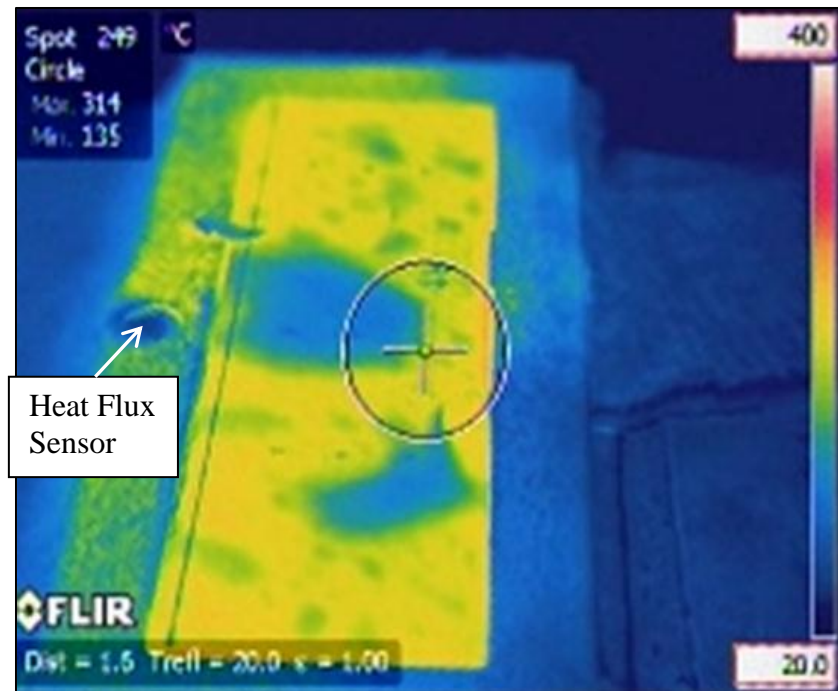


Figure 74. IR image of A9 (1.15 percent Moisture Content) Approximately 20 s after Removal from Heat Source

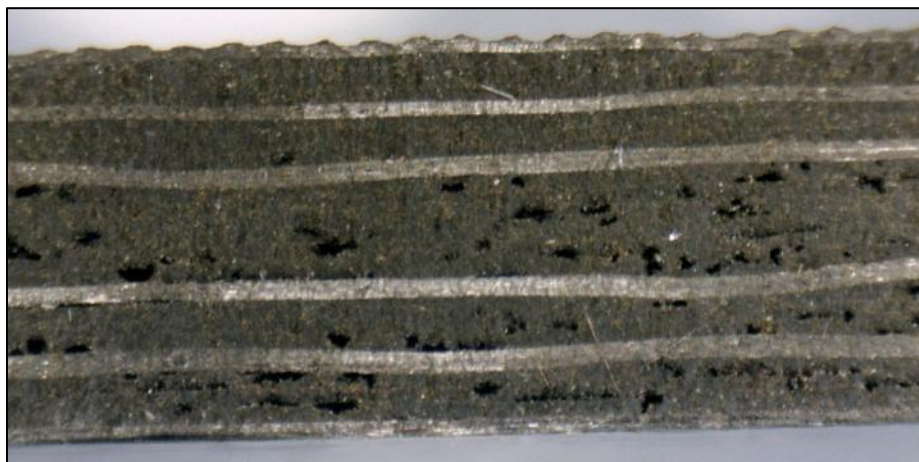


Figure 75. Cross-section of IM7/AFR-PE-4 Plate after being Cut with a Water-jet

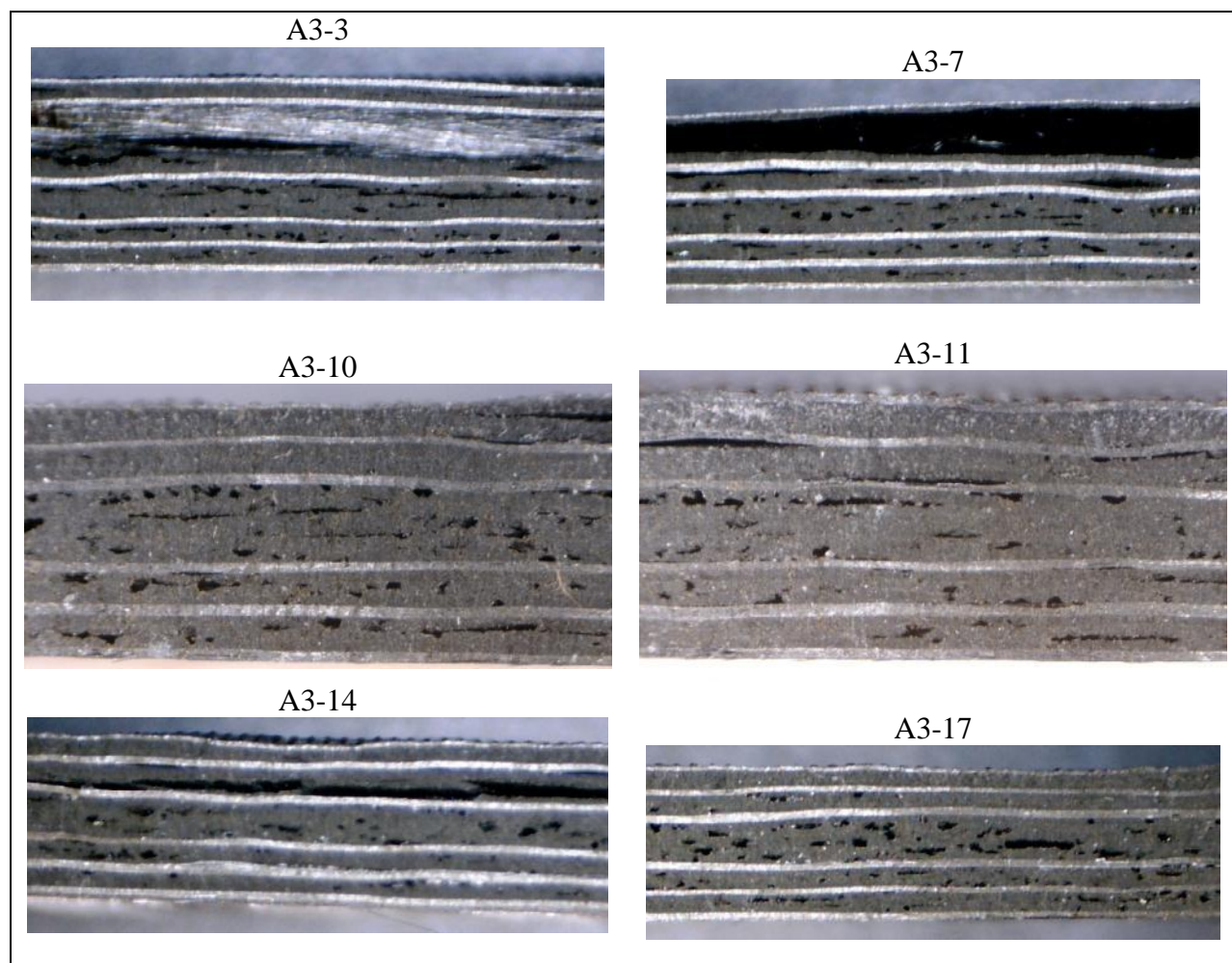


Figure 76. Cross section of Plate A3–Exposed at 34.1 kW/m^2 for 127 s

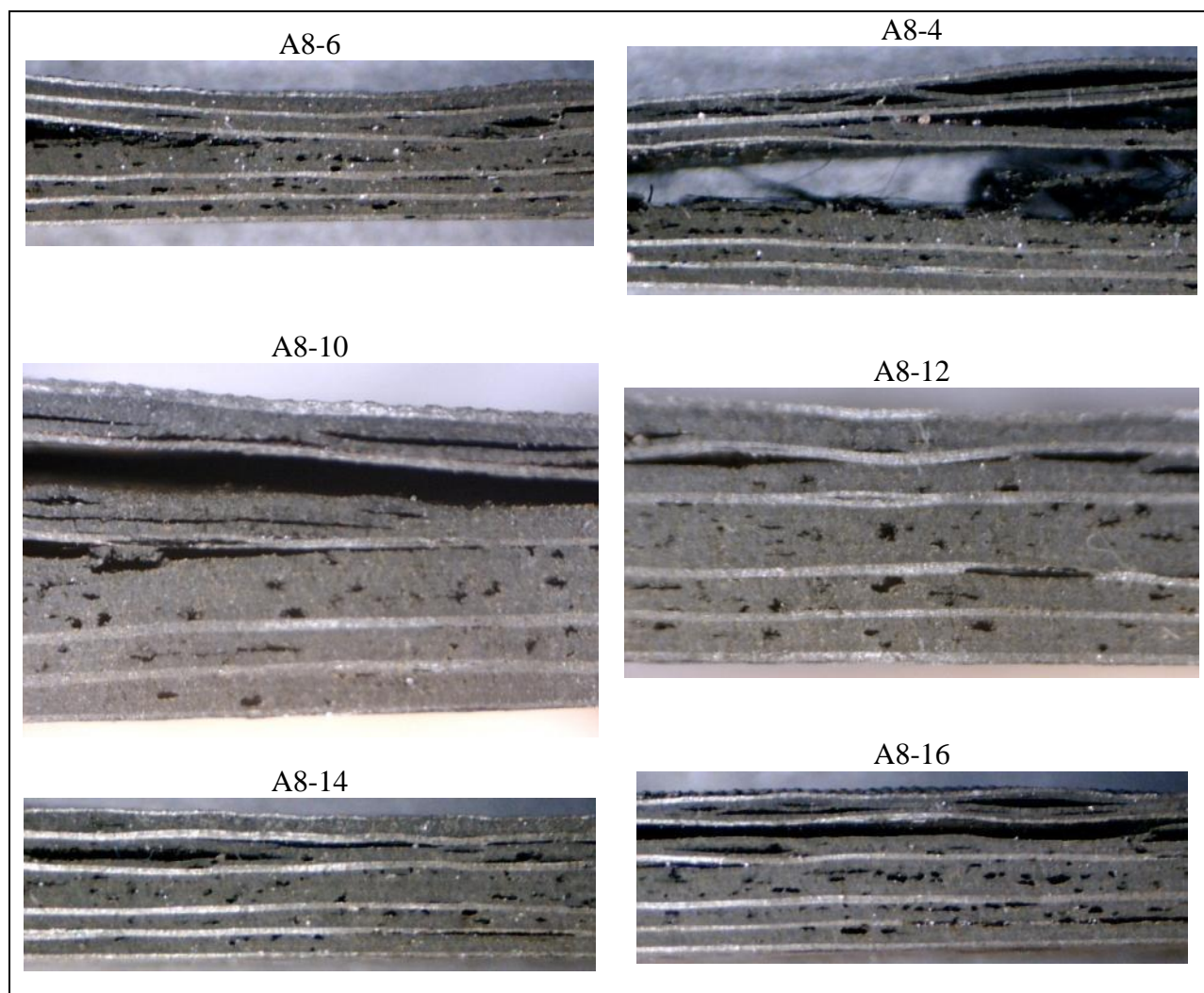


Figure 77. Cross section of Plate A8 – Exposed at 35.1 kW/m² for 151 s

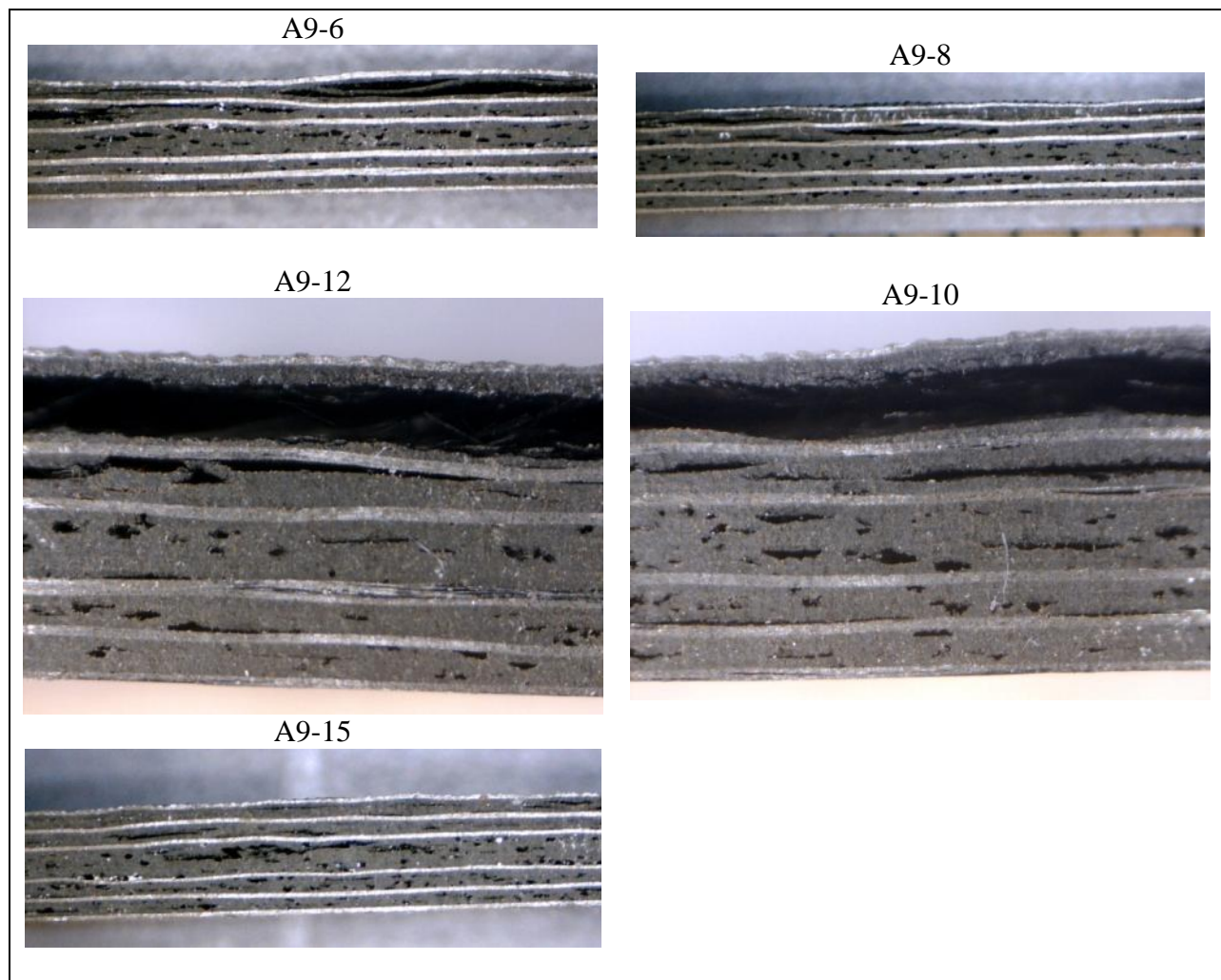


Figure 78. Plate A9 (1.15 percent Moisture Content) – Exposed at 35.2 kW/m^2 for 152 s

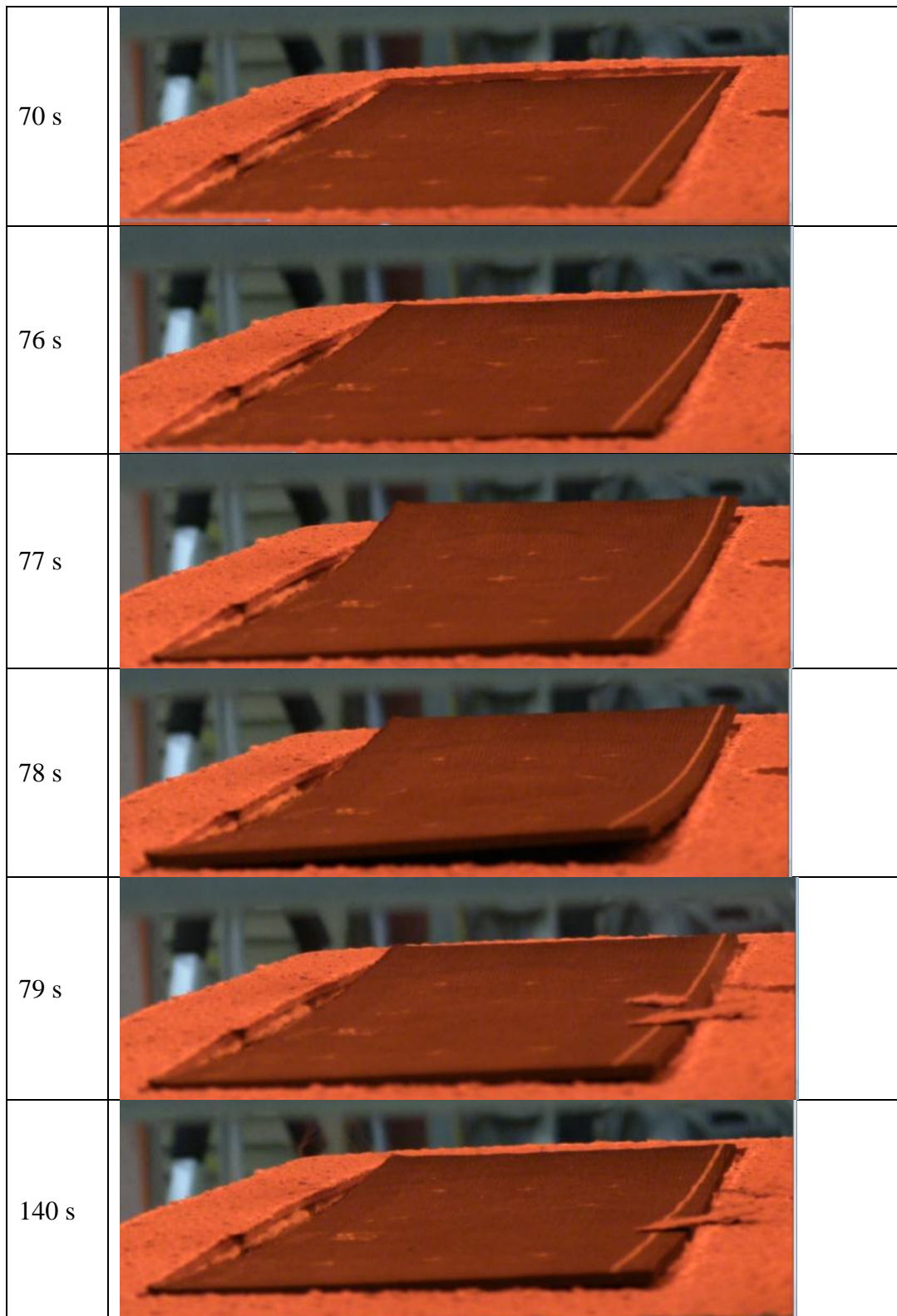


Figure 79. Plate A9 (1.15 percent Moisture Content) During Delamination at 35.2 kW/m²

5.2. Thermal Exposure Histories

The approximate delamination time was estimated from the embedded TC and backface TC readings, as shown in Figure 80 to Figure 92. These times corresponded well with the time of global plate buckling observed during testing. Deviations in the measured embedded TC temperatures are seen during delamination as plies separate from one another. If the TC remains bonded to the ply on the heat-exposed side of the plate, for example, a short-term increase in the rate of temperature increase is seen. A short-term reduction in the rate of temperature increase, and sometimes a temperature drop, is seen if the TC remains bonded to the ply away from the heating. Deviations in the backface TC temperatures, which are originally in contact with the insulated side of the plate, are seen when the surface of the plate is moved away from the TC, such as when global buckling occurs.

Two criteria were used to determine the time of global plate delamination. The first criterion used was the time when three of the embedded TCs showed deviations in the temperature loading rate. Indication from a single TC was not considered definitive because it could indicate when a small crack occurred around an individual TC and not be a good indicator of plate-wide delamination. The second criterion used was when all three backface TC readings (left, center and right) showed a deviation, as discussed above. The time and temperatures reported here are the averages of these two methods.

Note that plate R2 showed some indication of early delamination in plies 1 and 7 at much lower temperatures, as shown in Figure 83, but no indication from the backface TCs. This could have been just at the embedded TCs and not an indication of full plate delamination. Also note that plate A3 was removed from heat just as it was beginning to delaminate as evidenced by the buckling seen at the end of the test and the embedded TC data.

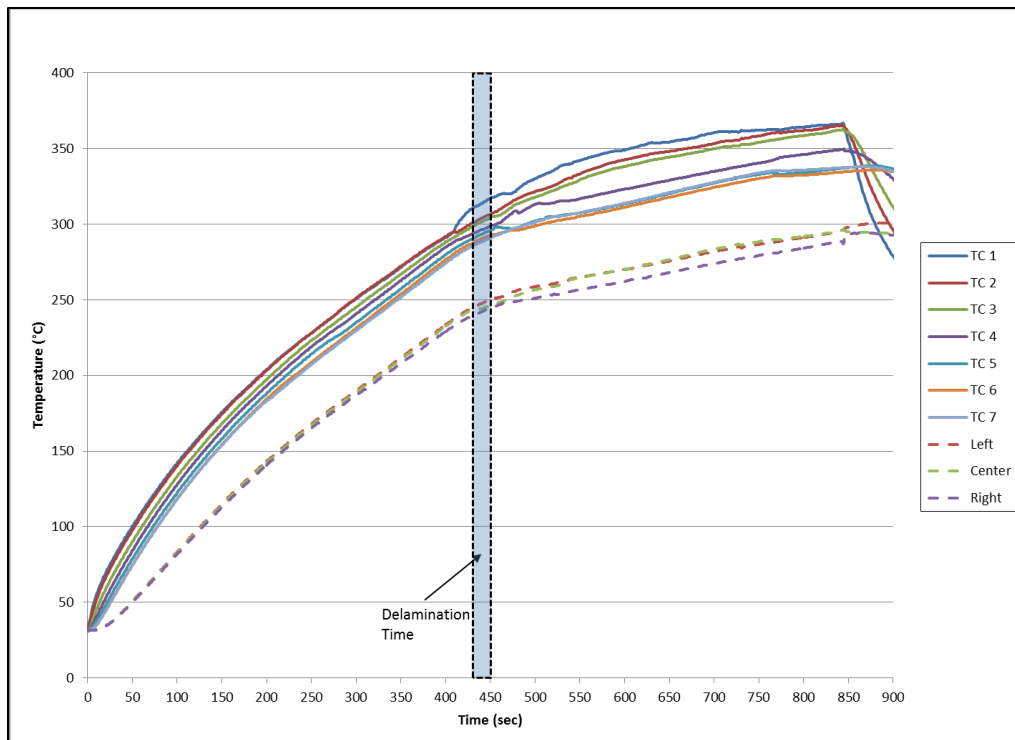
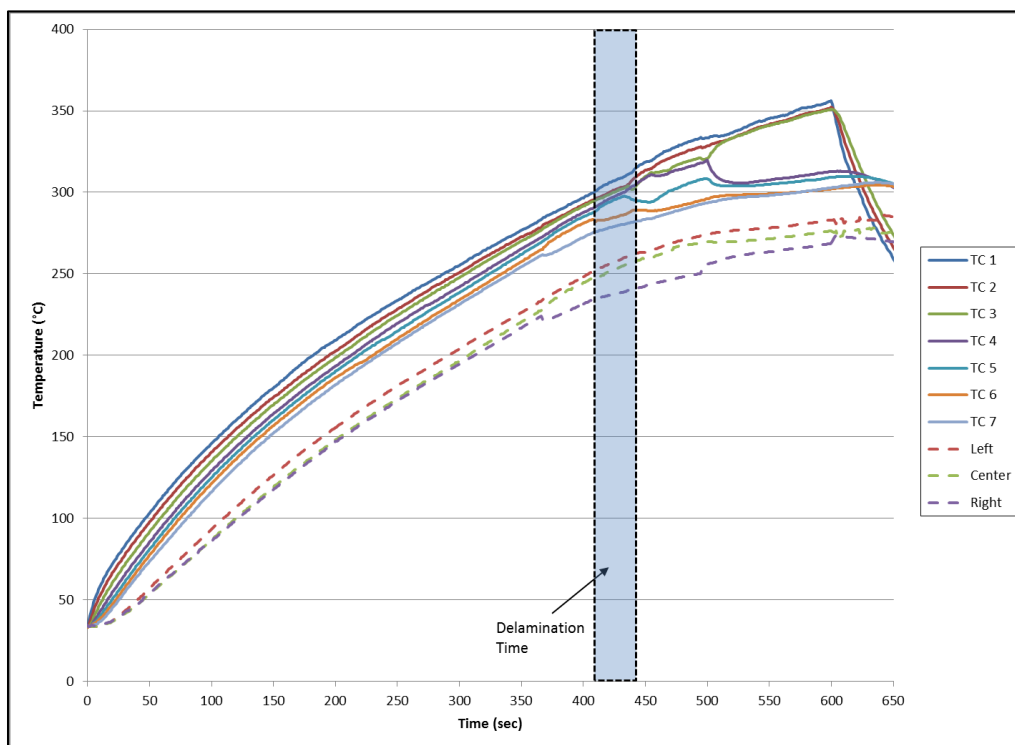


Figure 80. Plate C4 Thermocouple Data (Exposed at 15.2 kW/m^2 for 844s)



**Figure 81. Plate C9 Thermocouple Data
(0.3 percent Moisture Content, Exposed at 15.4 kW/m^2 for 601 s)**

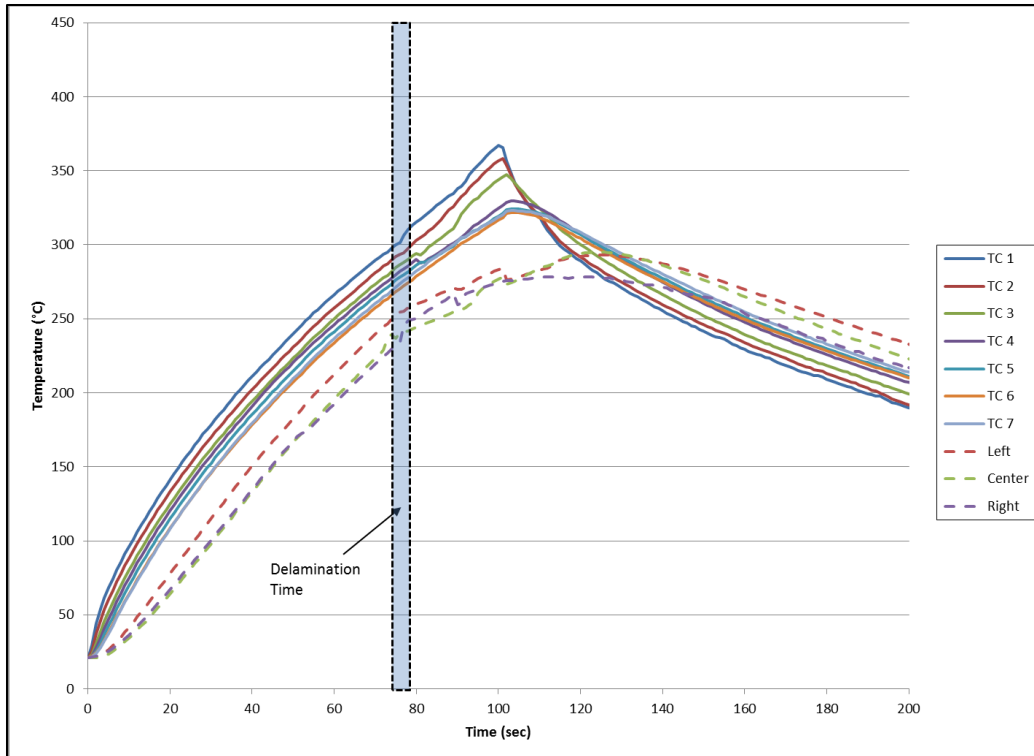


Figure 82. Plate R6 Thermocouple Data (Exposed at 34.2 kW/m² for 101 s)

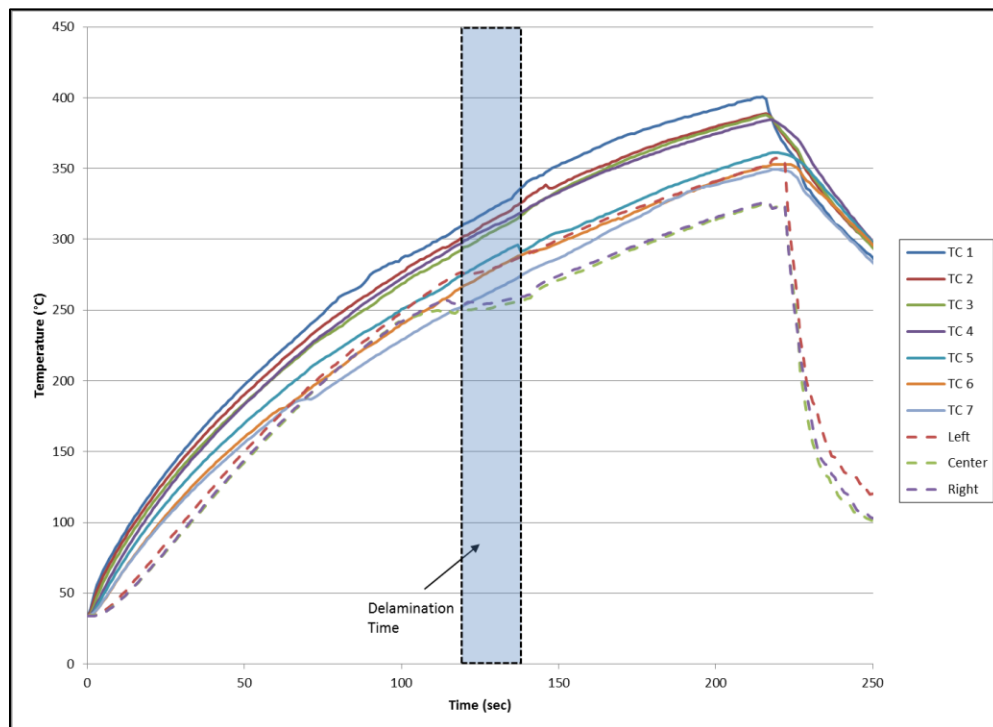
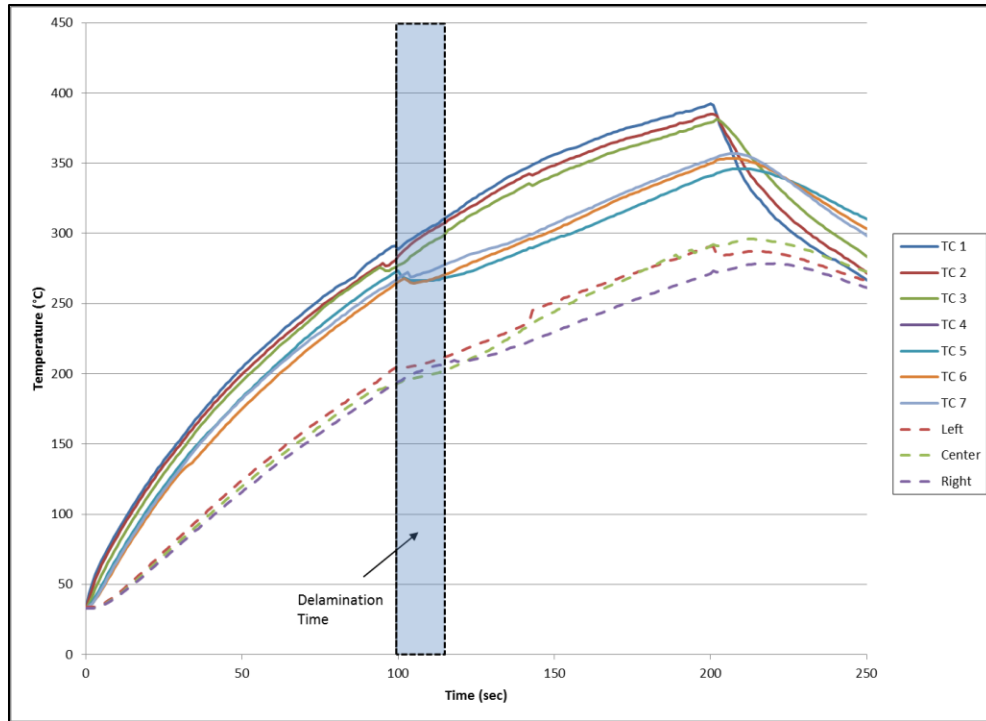


Figure 83. Plate R2 Thermocouple Data (Exposed at 26.2 kW/m² for 214 s)



**Figure 84. Plate R9 Thermocouple Data
(0.4 percent Moisture Content, Exposed at 25.9 kW/m² for 201 s)**

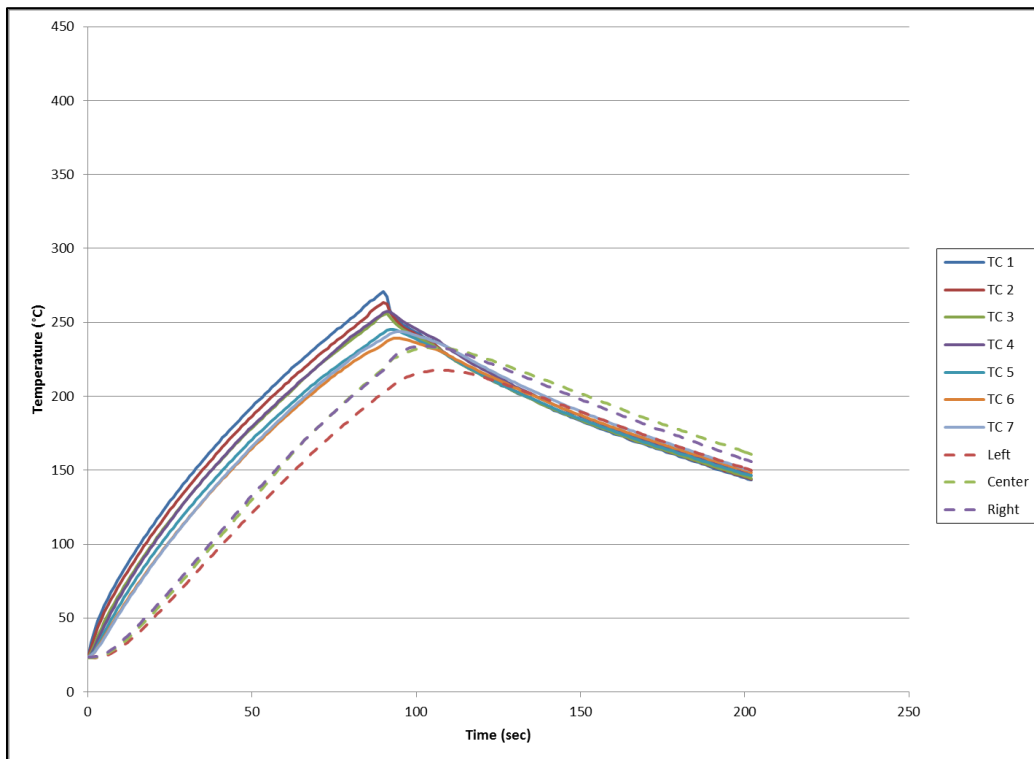


Figure 85. Plate R3 Thermocouple Data (Exposed at 24.9 kW/m² for 91 s)

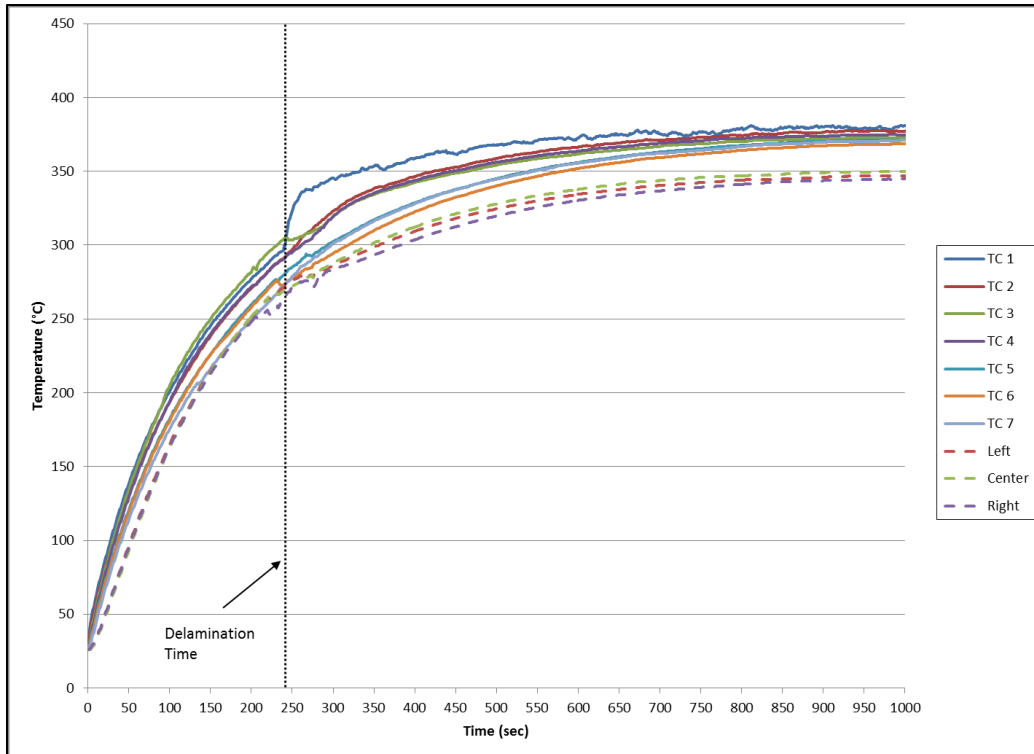


Figure 86. Plate R8 Thermocouple Data (Exposed at 15.3 kW/m² for 1040 s)

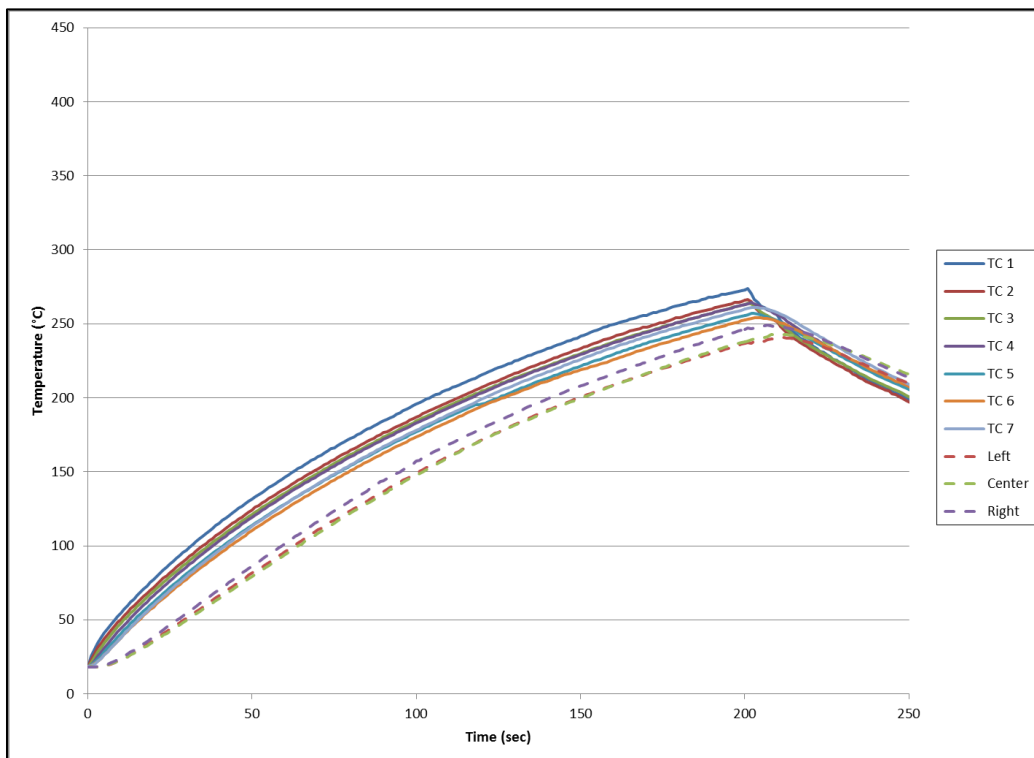


Figure 87. Plate R7 Thermocouple Data (Exposed at 15.2 kW/m² for 201 s)

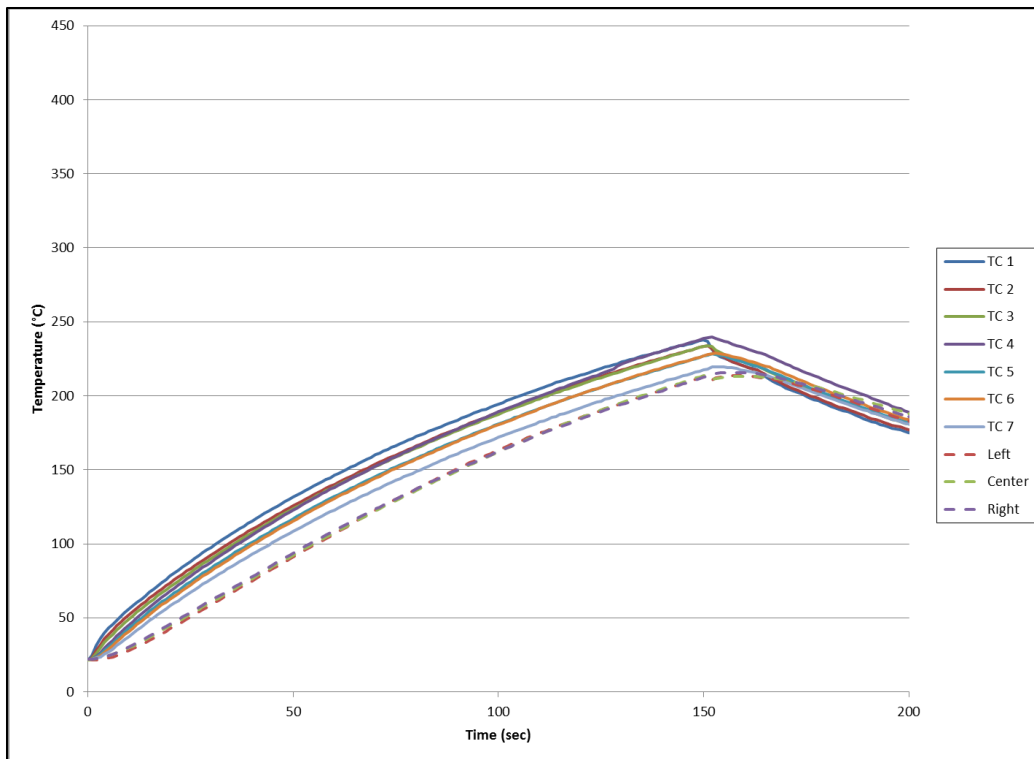


Figure 88. Plate R4 Thermocouple Data (Exposed at 14.9 kW/m^2 for 151 s)

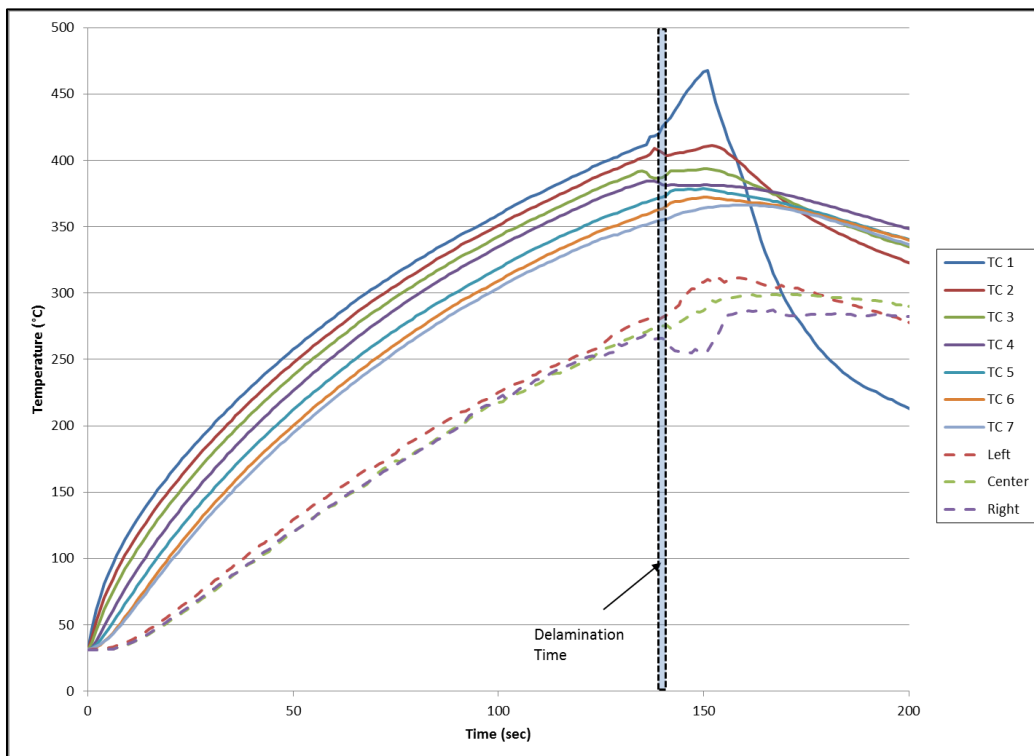


Figure 89. Plate A8 Thermocouple Data (Exposed at 35.1 kW/m^2 for 151s)

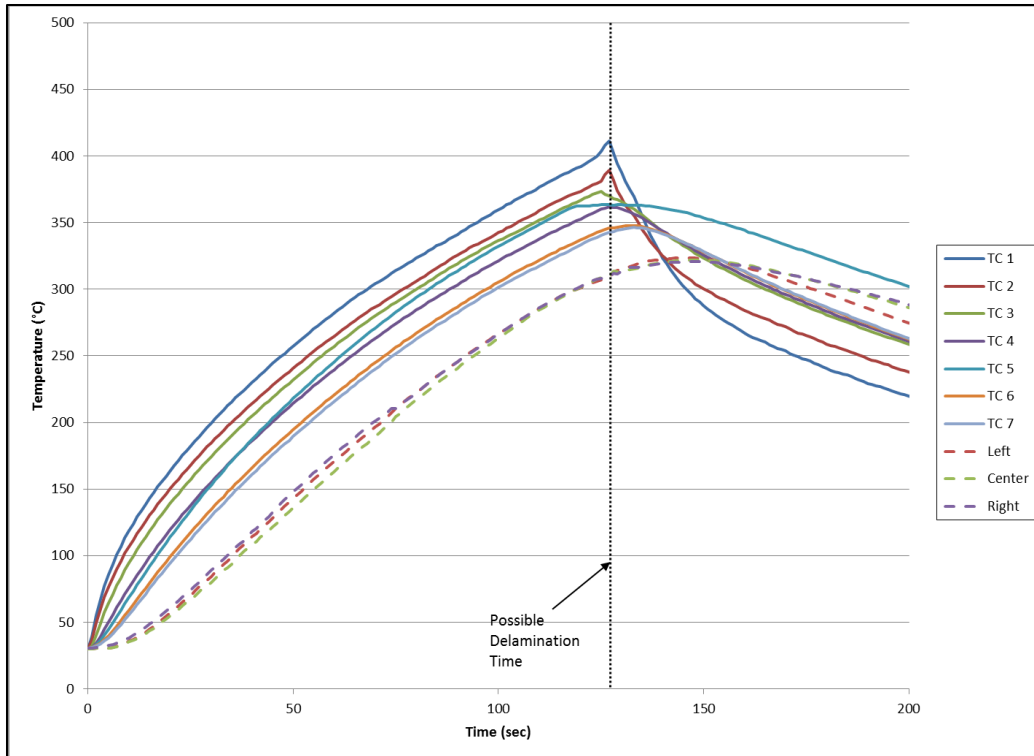


Figure 90. Plate A3 Thermocouple Data (Exposed at 34.1 kW/m² for 127 s)

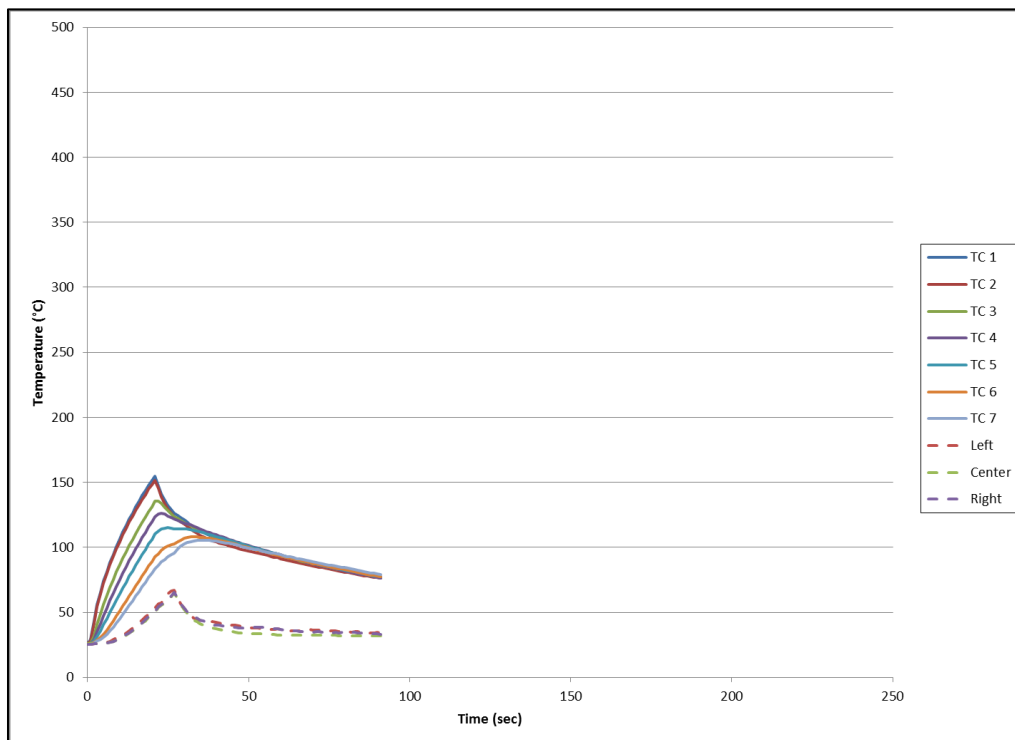


Figure 91. Plate A2 Thermocouple Data (Exposed at 34.0 kW/m² for 20 s)

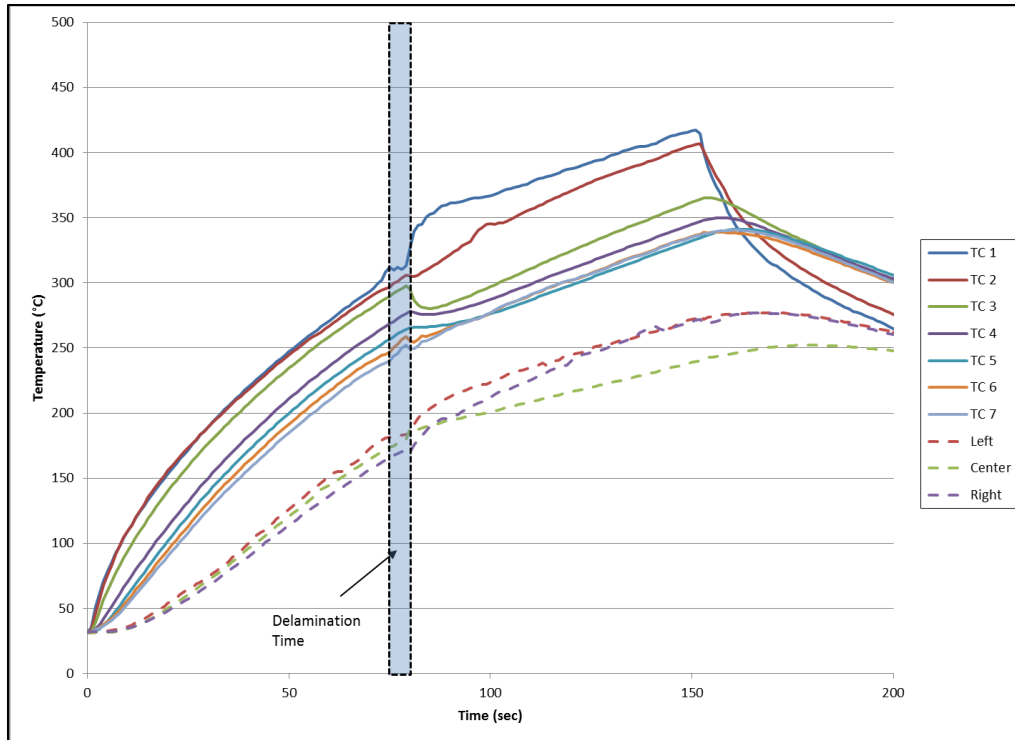


Figure 92. Plate A9 Thermocouple Data (1.15 percent Moisture Content, Exposed at 35.2 kW/m² for 152 s)

5.3. Delamination Time and Temperatures

A summary of the times to delamination for two of the dry materials tested are shown in Figure 93 (IM7/RM3002 and IM7/AFR-PE-4). Results from these two materials can be compared because the plates had nominally the same thickness. Delamination times for IM7/977-3 are not shown as these plates were nominally twice as thick. Time to delamination as a function of heat flux intensity is shown for IM7/RM3002 in Figure 93(a). As would be expected, the time to delamination drops rapidly with increasing heat flux. Limited testing was performed on IM7/977-3 and IM7/AFR-PE-4 composites at a single heat flux intensity, however, so the variation with heat flux is unknown. For comparison between materials, delamination times for IM7/RM3002 and IM7/AFR-PE-4 are shown in Figure 93(b) at a heat flux of 35 kW/m². The higher dry T_g material IM7/AFR-PE-4 took longer to delaminate.

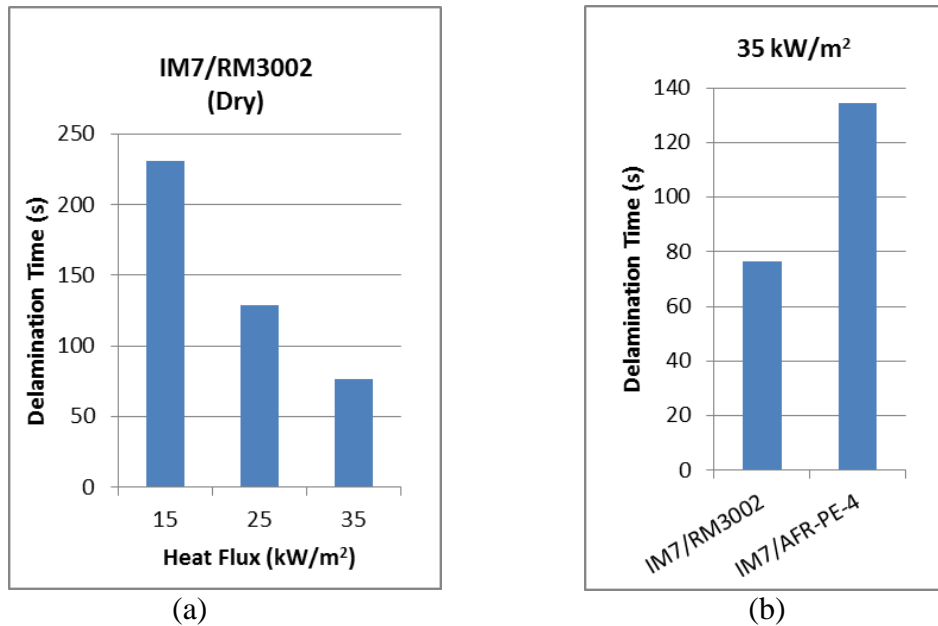


Figure 93. Delamination Times in (a) Dry IM7/RM3002 Plates at Three Heat Flux Magnitudes and (b) In Dry Plates Tested at 35 kW/m²

When moisture was added to the plates, as shown in Figure 94, IM7/AFR-PE-4 had the greatest reduction in the time to delamination. Note that it also had the highest moisture content. The time to delamination at 35 kW/m² was actually reduced to the same time (77 s) as the lower T_g material, IM7/RM3002, tested dry at this heat flux. No conclusion can be made about the relative sensitivity to moisture for all materials tested since each was at a different moisture content at the time of testing. There was not time to fully saturate all materials, nor sufficient materials in the testing program to test at varied moisture contents.

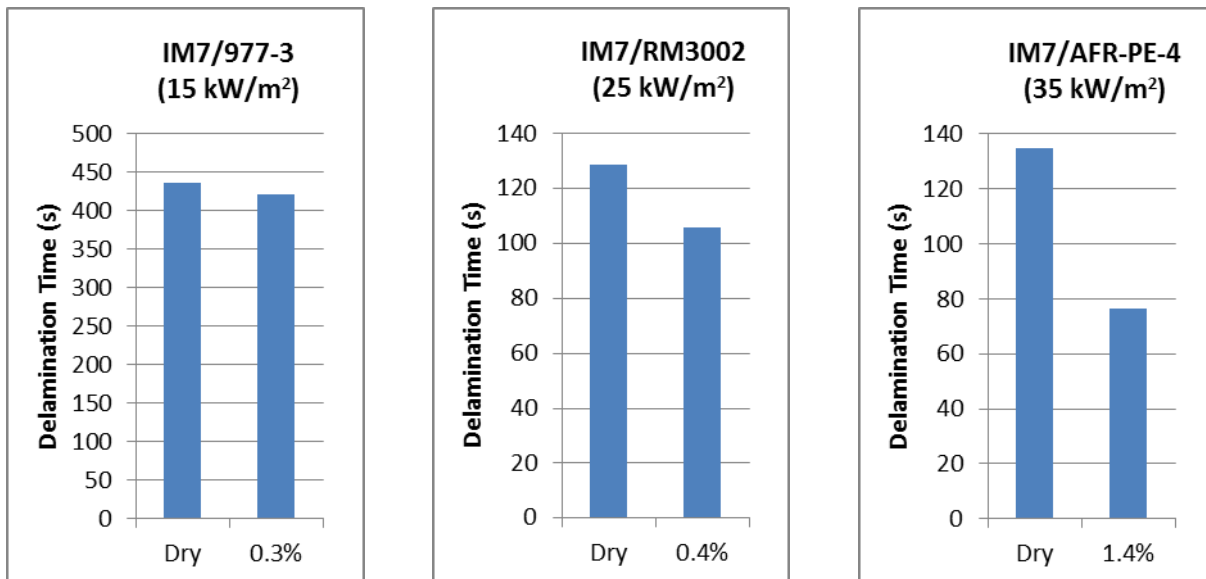


Figure 94. Effect of Moisture Content on the Time to Delamination at Fixed Heat Flux Magnitudes

The lowest Tg material, IM7/977-3, showed the least reduction in time to delamination tested wet and dry, as shown in Figure 94. It is not clear from the limited data what effect the greater specimen thickness, lower heat flux, and smaller temperature gradient had on these samples with regard to the elevated moisture content. Additional testing is needed.

Direct comparisons of the three different composite materials cannot be made because of differences in material thickness and in the heat flux intensities to which each material was exposed. However, the plate temperatures at which delamination occurred can be compared, as shown in Figure 95 for IM7/RM3002 and in Figure 96 for all three materials. Ply temperatures on front (exposed to heat) and back (insulated) of the laminate plate (TC 1 and 7) were recorded at the time of apparent delamination. Results for IM7/RM3002 in Figure 95 also show the temperatures at the time a plate was removed from heat for plates that did not delaminate.

Since IM7/RM3002 was tested at three heat flux intensities, some observation can be made regarding the temperature at which delamination occurred independent of the heat flux applied. Delamination did not occur until the TC 7 temperatures reached approximately 270 °C for all IM7/RM3002 plates tested. Plates that did not reach this temperature at any ply in the samples did not delaminate. Based on this result, one approach to ensure delamination does not occur in IM7/RM3002 would be to limit exposures such that temperatures stay below 270 °C. It is not known whether this would prevent delamination in material with moisture present. A thermodynamic-mechanical model would need to be developed to better predict delamination times for general layups, heat exposures and moisture contents.

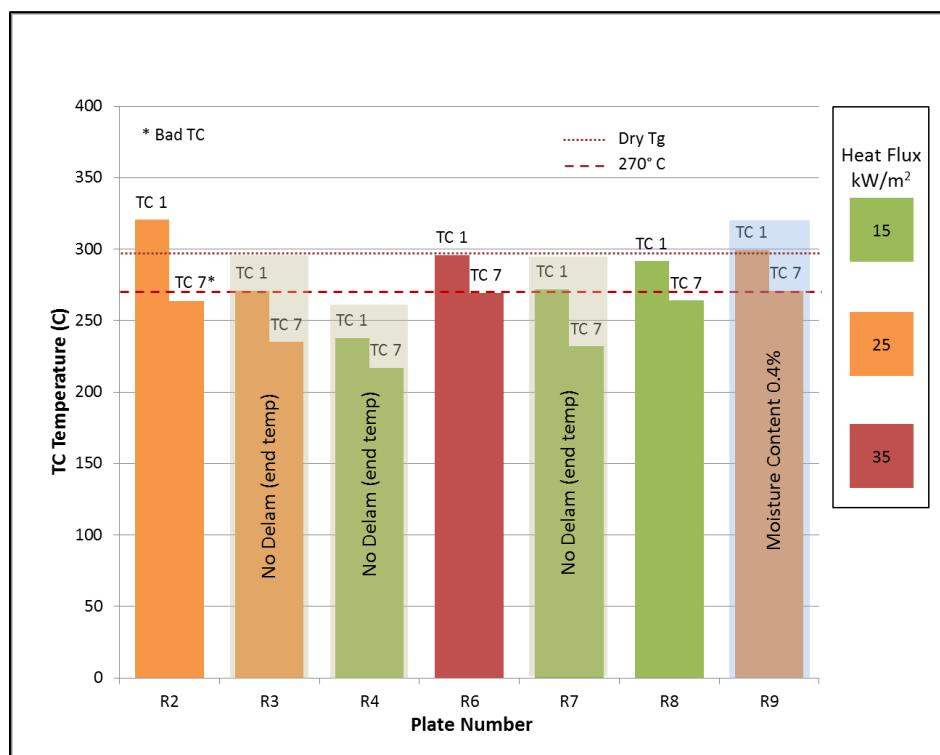


Figure 95. IM7/RM3002 Plate Front (TC 1) and Back (TC 7) TC Temperatures at the Time of Delamination

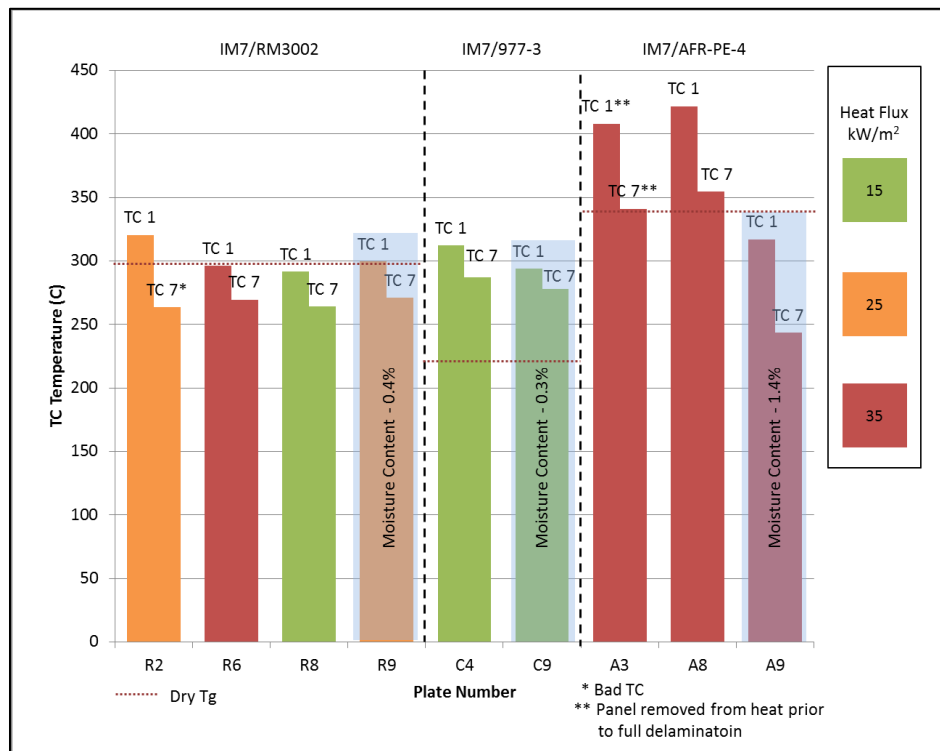


Figure 96. TC Temperatures at the Time of Delamination for all Plates Tested

As was mentioned, the material with the highest Tg, AFR-PE-4, showed the largest reduction in the temperature at which delamination occurs due to the presence of moisture in the composite. As shown in Figure 96, temperatures varied between 341° C on the back faces and 422° C on the front faces of the dry material at the time of delamination. When delamination occurred, the entire plate was above the dry Tg for this material, cited by the manufacturer as 340° C. Water in general acts as a plasticizer, lowering the Tg, but it's effect on this condensation polyimide resin is not known. The temperatures in the plate with 1.4 percent moisture content varied from 244° C to 317° C at the time of delamination, well below the dry Tg.

For the limited test conditions evaluated, IM7/977-3 and IM7/RM3002 showed no delaminations when any part of the material was below 250° C, with and without water moisture. Although IM7/AFR-PE-4 (the material having the highest dry Tg) delaminated with a minimum plate temperature of about 340° C, this temperature was reduced to 225° C with water moisture in the plate. In the absence of a robust method for predicting composite mechanical degradation as a function of time with the dominant damage from delaminations, an interim solution is to use these maximum allowable temperatures based on the limited elevated moisture results. The following are the current recommendations for limiting temperatures in the three materials evaluated to prevent delamination from occurring:

- Limit temperatures to 250° C for IM7/977-3.
- Limit temperatures to 250° C for IM7/RM3002.
- Limit temperatures to 225° C for IM7/AFR-PE-4.

5.4. Mechanical Test Results

5.4.1. Flexural Testing: Four-Point Bending

Four-point bend testing was performed on unexposed and heat-exposed samples with the heat-exposed side in both compression and tension. The flexural strength, maximum strain and chord modulus are shown in Figure 97 to Figure 99. The standard deviation of typically four tests with the heat exposed side in tension (T) and five in compression (C) are shown with the error bars in the figures. Note that plates that did not delaminate from heat exposure are marked with 'ND' and those that did with 'D'. The flexural strength is equal to the maximum stress in the outer fibers at the moment of break. The maximum strain is the strain in the outer fibers at break. Calculation of the chord modulus was discussed in Section 3.4.3.4 and represents the flexural stiffness at low strains relative to the failure strains.

Little to no change of flexural strength is seen in IM7/RM3002 plates that did not delaminate (cf. plates R, R4, R3, R7 in Figure 97). There was very little mass loss in these plates (<0.1 percent). A loss in flexural strength of over 75 percent is seen when the plates delaminate (plates R2, R6, R8). There is also a trend in flexural strength of the delaminated IM7/RM3002 plates with heat flux intensity; the lowest heat flux showed the largest strength and the highest heat flux showed the lowest strength. It is possible that the larger heat fluxes drove the delaminations to grow larger in these plates, but this was not quantified. Other non-destructive evaluation techniques, such as ultrasonic C-scan, are recommended to quantify the degree of delamination.

The IM7/977-3 and IM7/AFR-PE-4 materials also had a large drop in flexural strength once delamination occurred. The highest T_g material, IM7/AFR-PE-4, demonstrated the smallest drop in strength with delamination in the one plate tested (approximately 30 percent). It is important to note, however, that plate A3 was removed from heat just as delamination started. So it is not clear if reduction in flexural strength is less severe in this material or if similar reductions would be seen if allowed to complete delamination.

The overall effect on material chord modulus and failure strain is similar to that for the strength (Figure 98 and Figure 99). The IM7/RM3002 delaminated plates showed a strong dependence on heat flux, with increasing stiffness at lower heat fluxes, as was the case for the flexural strength. Here, the effect on modulus was a drop of 23 percent at the lowest heat flux and a drop of 60 percent at the highest heat flux. The apparent increase in modulus of the IM7/RM3002 plates (cf. plates R, R3, R4, and R7 in Figure 98) is likely due to plate-to-plate variation rather than an effect of the heat exposure. Plate R was thicker than the other plates by approximately 12 percent, with the same number of plies, indicating the fiber volume fraction was likely lower in this plate. Because fibers are the stiff part of the composite, and the matrix is softer, a smaller volume fraction of fibers would be expected to result in a lower chord modulus.

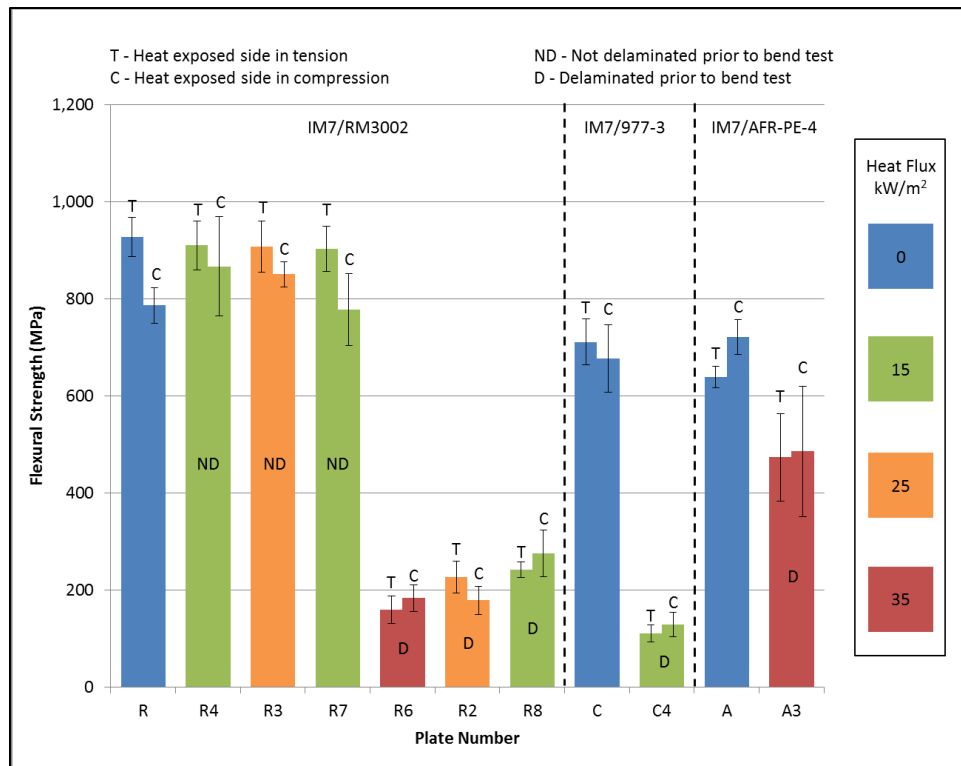


Figure 97. Flexural Strength

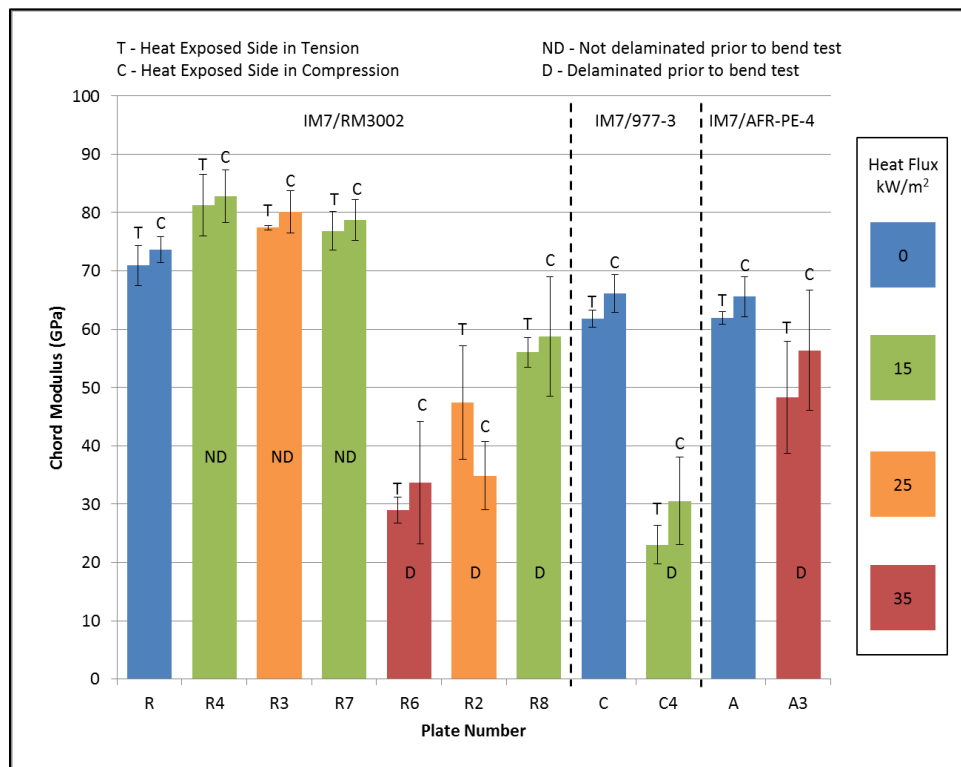


Figure 98. Chord Modulus

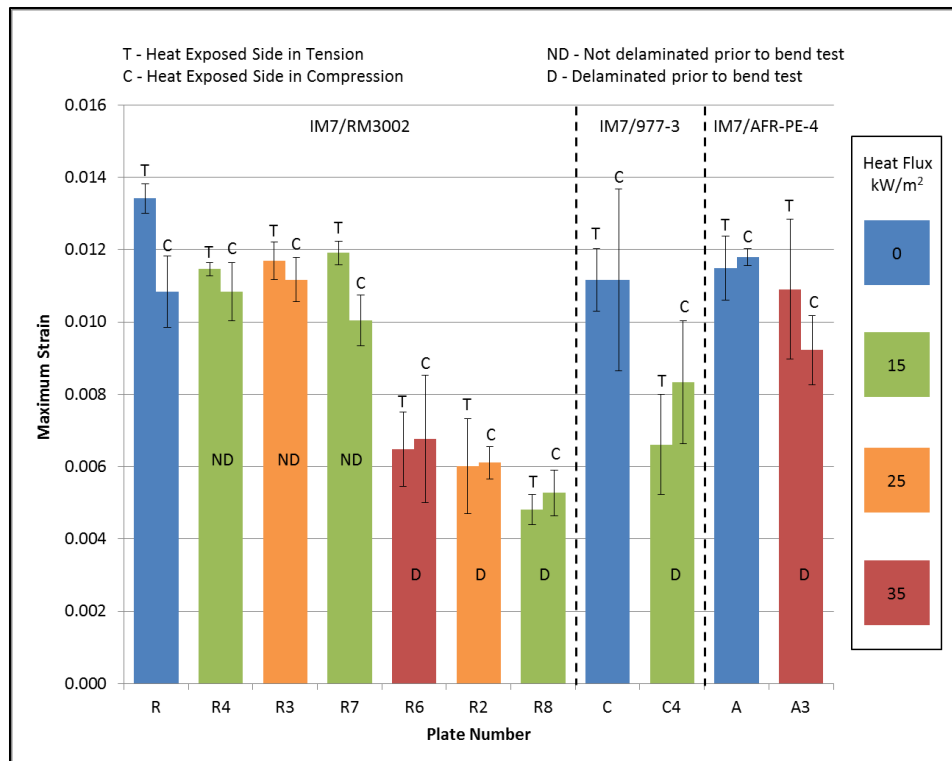
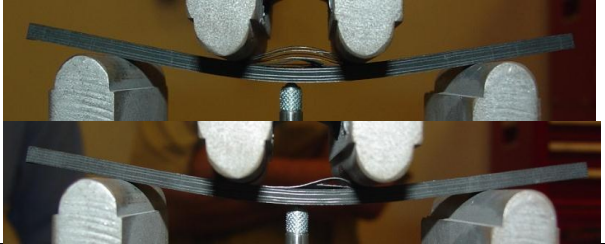
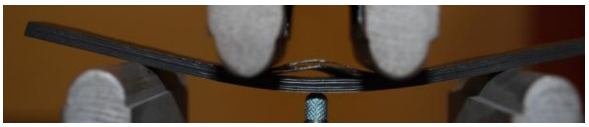

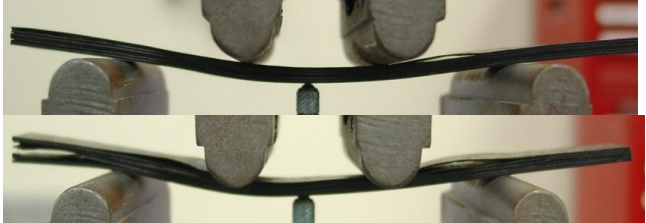
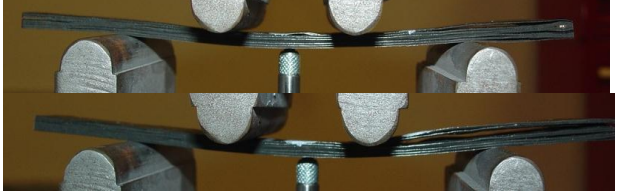






Figure 99. Maximum Strain

Failure modes witnessed in the flexural testing are shown in Table 6. IM7/RM3002 samples exposed to heat, but with no delaminations prior to mechanical testing, failed with the same failure mode as samples not exposed to heat: ply compression failure and delamination in the region between the loading noses. All heat-exposed materials with delaminations from the heat exposure failed between the loading noses or at the end of the sample.

Table 6. Examples of Flexural Failure Modes with and without Heat-induced Damage

Material	Heat Exposure	Failure Mode	Image
IM7/RM3002 (ND)	None	Ply compression failure and delamination	
IM7/RM3002 (ND)	24.9 kW/m ² for 91 s	Ply compression failure and delamination	
IM7/RM3002 (D)	26.2 kW/m ² for 214 s	Center Delamination	
IM7/RM3002 (D)	34.2 kW/m ² for 101 s	Center and End Delamination	
IM7/RM3002 (D)	15.3 kW/m ² for 1040 s	End Delamination	
IM7/977-3 (ND)	None	Delamination with ply buckling	
IM7/977-3 (D)	15.3 kW/m ² for 1040 s	Center and End Delamination	
IM7/AFR-PE-4 (ND)	None	Center Delamination	
IM7/AFR-PE-4 (D)	34.1 kW/m ² for 127 s	End Delamination	
D – Delaminated prior to bend test			ND – Not delaminated prior to bend test

5.4.2. Tensile Testing

Tensile testing was performed on unexposed and heat-exposed samples. The tensile strength, ultimate tensile strain and tensile chord modulus of elasticity are shown in Figure 100–Figure 102. Tensile strength is the maximum stress measured in a sample prior to catastrophic failure. The ultimate tensile strain is the maximum strain prior to catastrophic failure. The tensile chord modulus represents the stiffness at low strains (from 1000 to 3000 microstrain).

The standard deviation of six samples are shown with the error bars in the figures. Only three samples were tested for plates A, C, C4, R and R6. Data for A3 is from a single sample so no standard deviation is shown. Note that plates that did not delaminate from heat exposure are marked with ‘ND’ and those that did with ‘D’. In general, the heat-exposed plates that delaminated showed less degradation in all of these properties than the flexural properties, as would be expected by the dominant damage mode of delamination. Flexural strength is dominated by the interlaminar shear strength, which is degraded by delaminations. Tensile strength is dominated by the fiber strength, but is still degraded to a lesser extent by delaminations due to reduced load transfer between plies.

All materials showed a reduction in tensile strength for samples with delaminations from heat exposure. This reduction was only large for IM7/977-3, which had a 40 percent drop in tensile strength between the two plates tested. Tensile modulus and ultimate tensile strain were also reduced for this material. IM7/AFR-PE-4 showed a similar trend, but the magnitude of the reduction in properties was much smaller. The material IM7/RM3002, with the most tests conducted showed some mixed results.

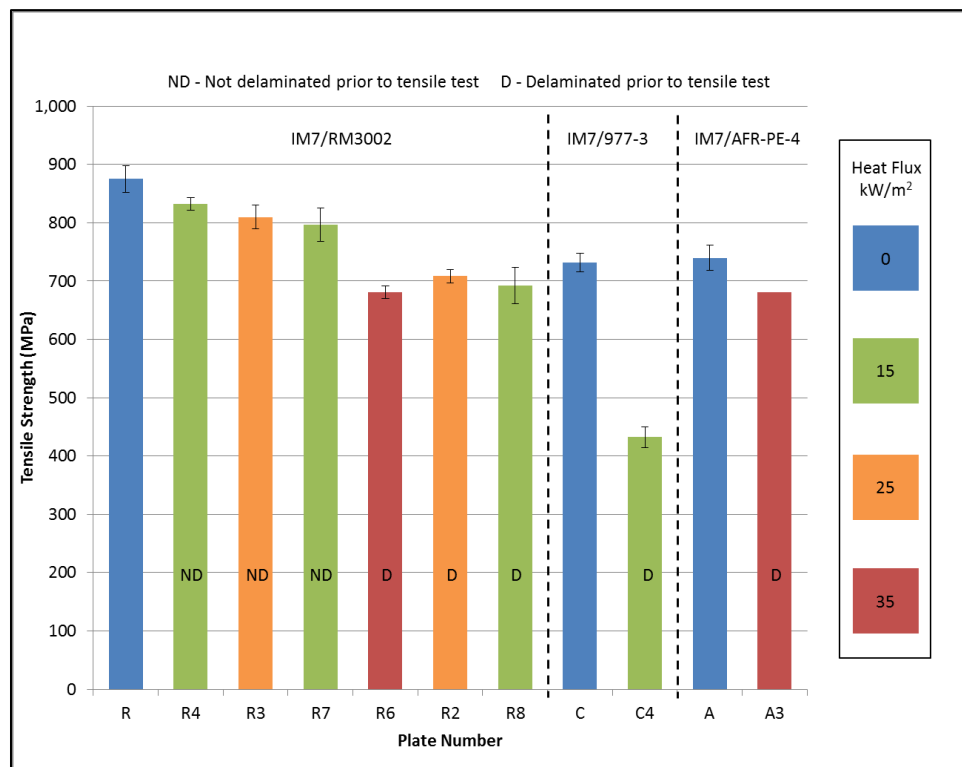


Figure 100. Tensile Strength

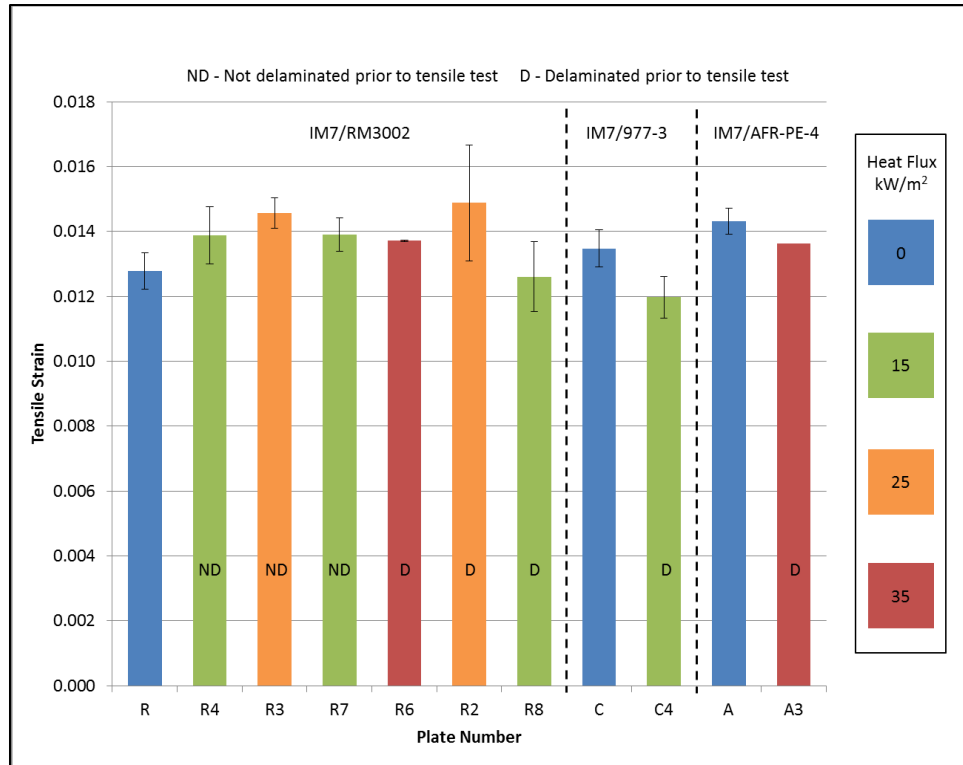


Figure 101. Ultimate Tensile Strain

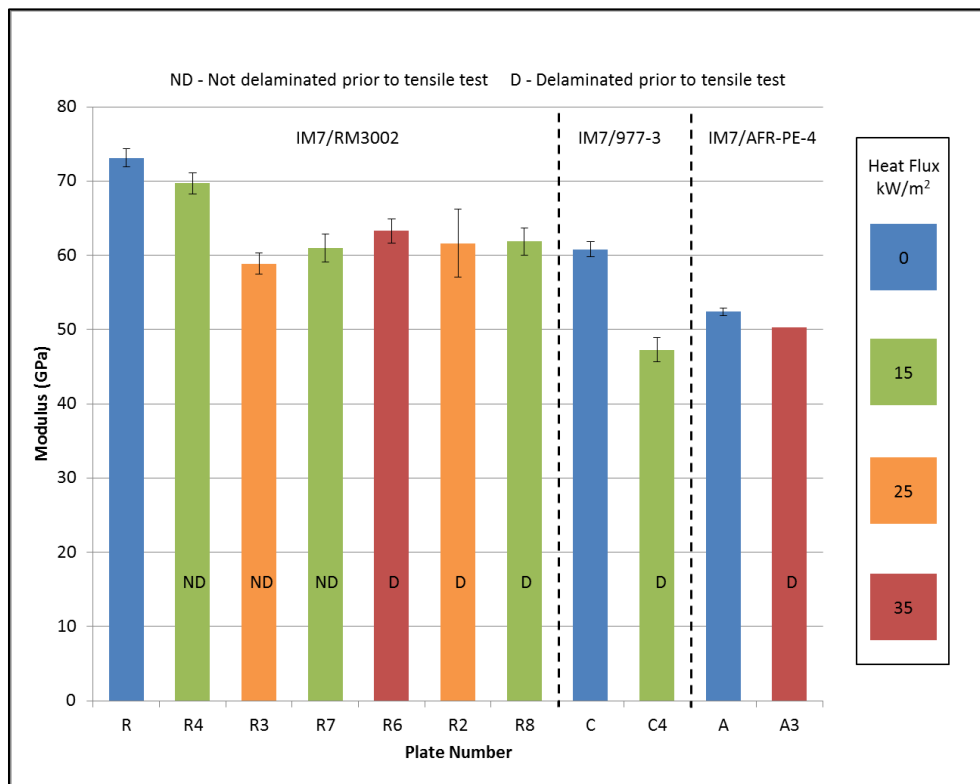


Figure 102. Tensile Chord Modulus of Elasticity

The tensile strength of IM7/RM3002 samples with delaminations from heat exposure was lower than samples with no delaminations, even with heat exposure. This is consistent with the other materials. Despite the lower strength, the ultimate tensile strain shows no trends, however. The chord modulus is also lower for samples with delaminations than material with no heat exposure (plate R). However, plates R3 and R7 with no delaminations also have a lower chord modulus similar to the delaminated plates. Plate variation may be responsible for the differences in chord modulus and ultimate strain rather than the effect of delamination. Future testing should ensure tight control on consistency between plates to avoid this uncertainty.

5.5. Modeling and Simulation of F-22 Fire Scenarios

Advanced CFD modeling of fires within the aircraft engine nacelle and near the wing structures was performed to determine potential fire effects and damage. This section details the results for the scenarios introduced in Section 4.2.1.

5.5.1. Engine Nacelle Model

After teleconferences with the F-22 SPO and the companies involved in designing/building the aircraft components, limited design specifications of the area in and around the F-22 engine nacelle were obtained. The F-22 Pratt & Whitney aircraft engine is shown in Figure 103. Design sketches of the structural components that make up the engine nacelle area were part of the information provided by the SPO. This structural data along with drawings found in TO 00-105E-9 [12], and photographs available on the internet, were utilized to prepare models approximating the engine nacelle structure of the F-22. Note that dimensions were interpolated based on the Frame Stations data provided by the SPO.

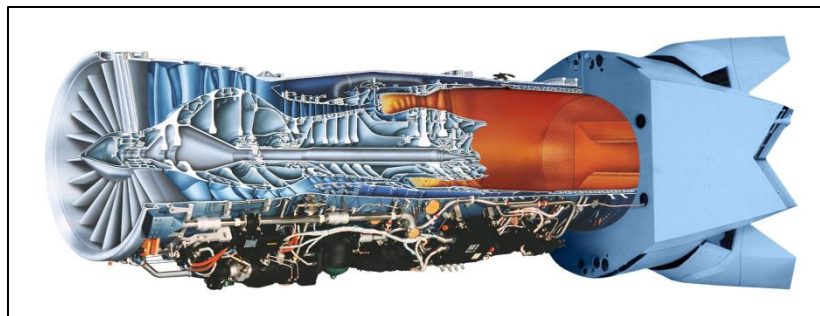


Figure 103. Pratt & Whitney F119-PW-100 Engine

The first attempts at modeling engine nacelle fires used a design with as much detail as possible from the limited information obtained from the F-22 SPO. The CFD model mesh topology of a single engine nacelle area and the aircraft engine is shown in Figure 104. This model was very poorly behaved computationally. The rib structures resulted in areas with very small mesh cells. These small cells were adjacent to large mesh cells which caused considerable instability in the model and impeded the modeled air stream flow through the structure. Figure 105 shows the unlikely flow pattern for this model of air mostly flowing around the engine instead of flowing from the front to the back of the engine.

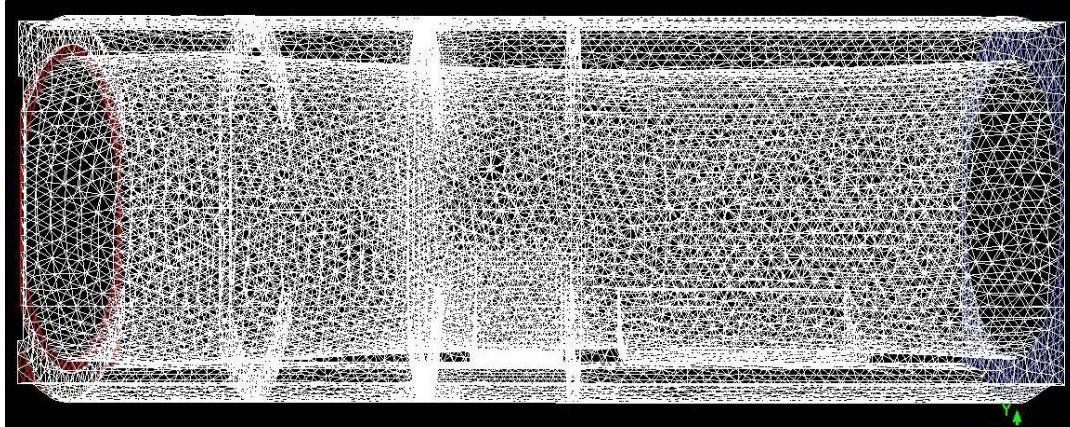


Figure 104. First Engine Nacelle Model

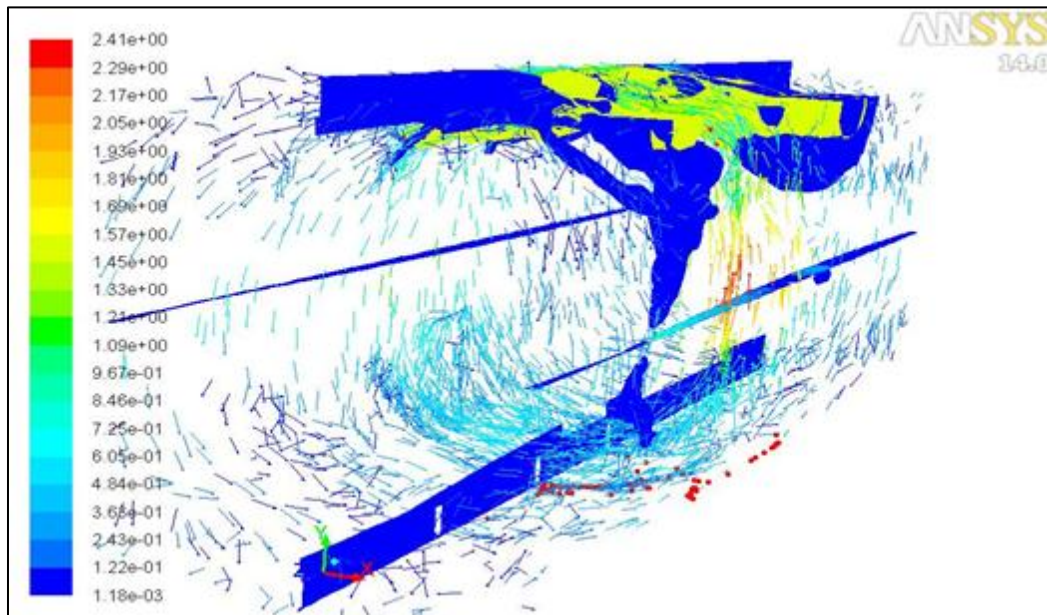


Figure 105. Velocity Vectors from the First Engine Nacelle Model

Applying lessons learned from the first model, a second model was developed without the rib details. This model produced more realistic air flows which accomplish the primary objective of cooling the engine.

The mesh topology for this model is shown in Figure 106, viewed from the bottom of the airplane looking up. This model shows the nacelle region of the plane, both F-119 engines, and a blue dot below the left engine to indicate the fuel leak location. Calculated air flow in this second nacelle model resulted in a much more reasonable flow pattern as shown in Figure 107 with air velocity flowing from the left side (or front) of the engine nacelle to the right side (nacelle rear). Figure 107 also shows incipient fire location inside the engine nacelle. The nacelle walls, engine

and gas temperatures were made invisible in this figure to allow a clearer view of the air velocity and temperature data.

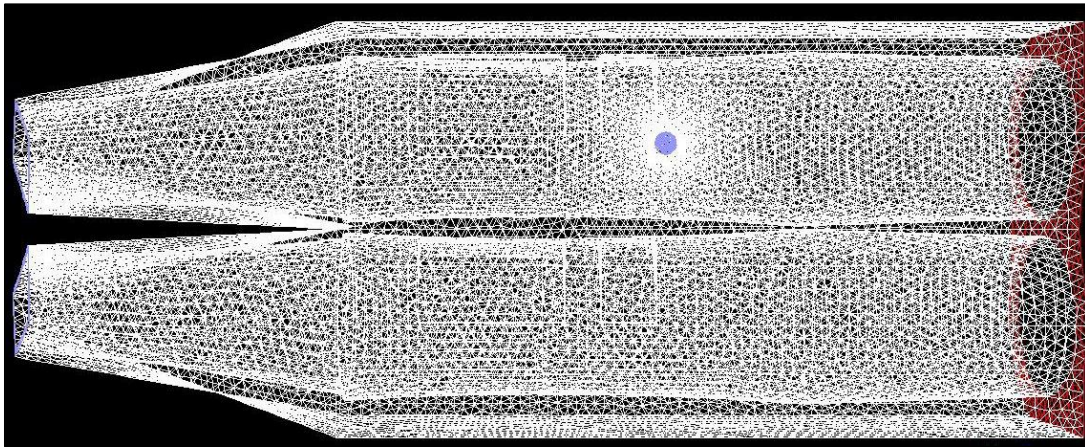


Figure 106. Second Engine Nacelle Spill Fire Model. View from Below

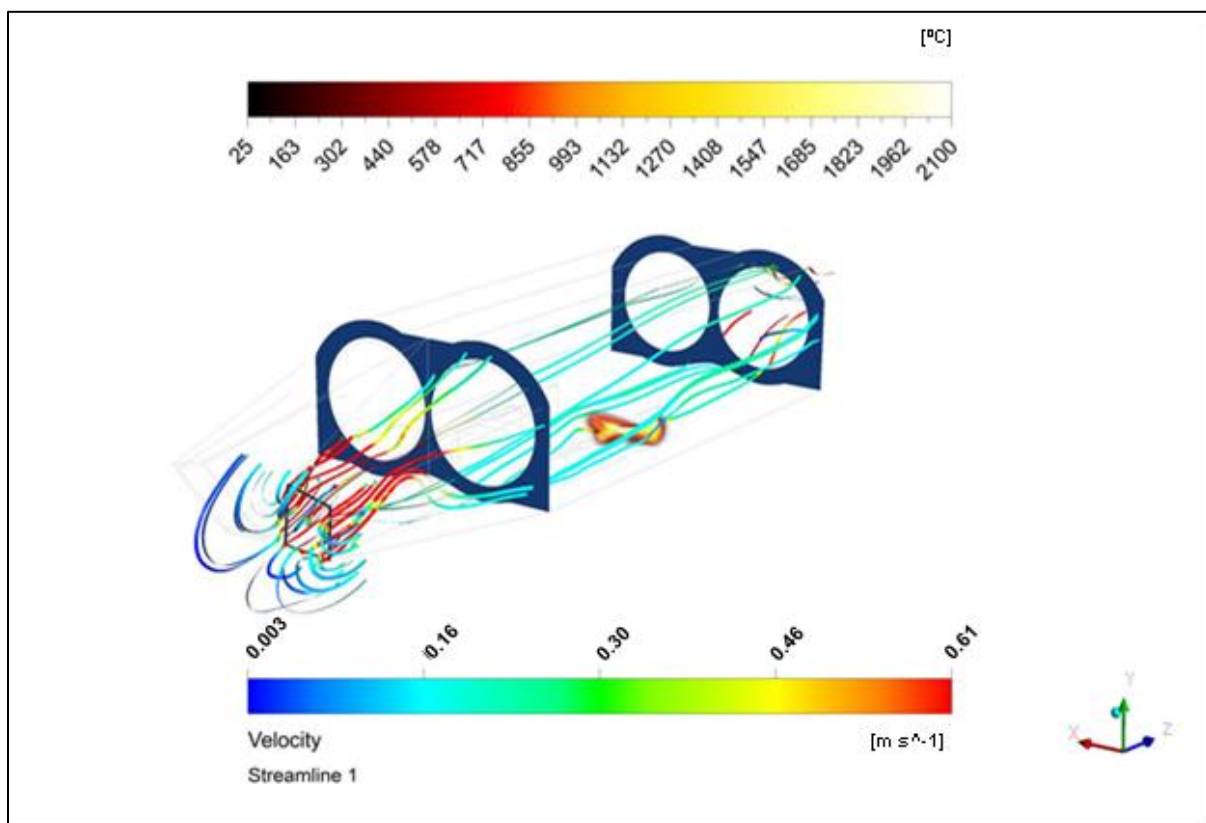


Figure 107. Flow Streams and Fire Zone Temperatures in the Second Nacelle Model

The fuel leak was positioned in a location on the bottom of the engine where a fuel or hydraulic line could rupture, near frame station 681. The fuel flow rate into the nacelle was 0.091 kg/s or about 1.8 gal/min and the fuel was consumed in combustion at the same rate. The fuel

temperature was set to 127 °C. The fuel that pooled in the bottom of the nacelle was assumed to ignite on a hot engine surface.

The composite IM7/5250 wall plates on the top surface of the engine nacelle are similar to the IM7/RM3002 plates that were evaluated in this test program. From information provided, the top surface composite plates were each estimated to be 3.4 m (11 ft) long and 1 m (3.3 ft) wide. The composite in this area was modeled as 3.2 mm (0.125 in) thick with a density of 1,514 kg/m³, specific heat of 2,200 J/g-K, and thermal conductivity of 1.2 W/m-K. The side of the composite wall plate away from the fire was exposed to a constant air temperature of 300 K in the model. Table 7 summarizes the parameters used in the model.

Table 7. Summary of the Engine Nacelle Model

Model Parameter	Value
Fuel Flow Rate/Fuel Consumption Rate	0.091 kg/s (~ 1.8 gal/min)
Fuel Temperature	127 °C
Composite IM7/5250 Top Surface Wall Plates	3.4 m (11 ft) long and 1 m (3.3 ft) wide
Composite Thickness	3.2 mm (0.125 in)
Composite Density	1,514 kg/m ³
Composite Specific Heat	2,200 J/g-K
Composite Thermal Conductivity	1.2 W/m-K
Composite back-side air temperature	300 K

As discussed in Section 4.3.5, the specific heat and thermal conductivity for IM7/RM3002 are nonlinear functions of temperature (see Figure 37). However, constant values were used in the CFD model for several reasons. First IM7/RM3002 is used as a surrogate BMI composite in this analysis for the IM7/5250 used in the F-22. Actual nonlinear properties for IM7/5250 are unknown. Second, as is discussed in the next section, the temperature increase happens quickly, leading to pyrolysis temperatures in the first 3 s. Using temperature-dependent values would not have a significant effect on this result, so no further effort was expended.

5.5.2. Engine Nacelle Fire

The incident scenario modeled assumed a fuel spill resulting in JP-8 fuel pooled in the lower area of the left nacelle and igniting. This model was used to develop a profile of thermal effects on the composite surfaces that form the top of the nacelle. A depiction of the modeled fire and interior gas temperature is shown in Figure 108. The fire plume can be seen to propagate around the engine (not shown) on the right side (when facing the front of the engine nacelle). Due to the geometry of the engine nacelle areas, the hot gases generated from the fire are contained in the right nacelle area.

This fire results in a high heat flux region on the top surface of the right nacelle and increased temperature of the composite wall plates at the top surface of the nacelle. Figure 109 shows the composite surface temperatures on the right top surface plate of the nacelle at time intervals from ignition until 12.2 s after ignition. Figure 109 is a plan view of the plates from below. The right side of the figure is the engine intake, the left side is the engine exhaust. No increase in surface

temperature is indicated on the left side nacelle top surface since the fire is initially contained on the right side nacelle of the aircraft.

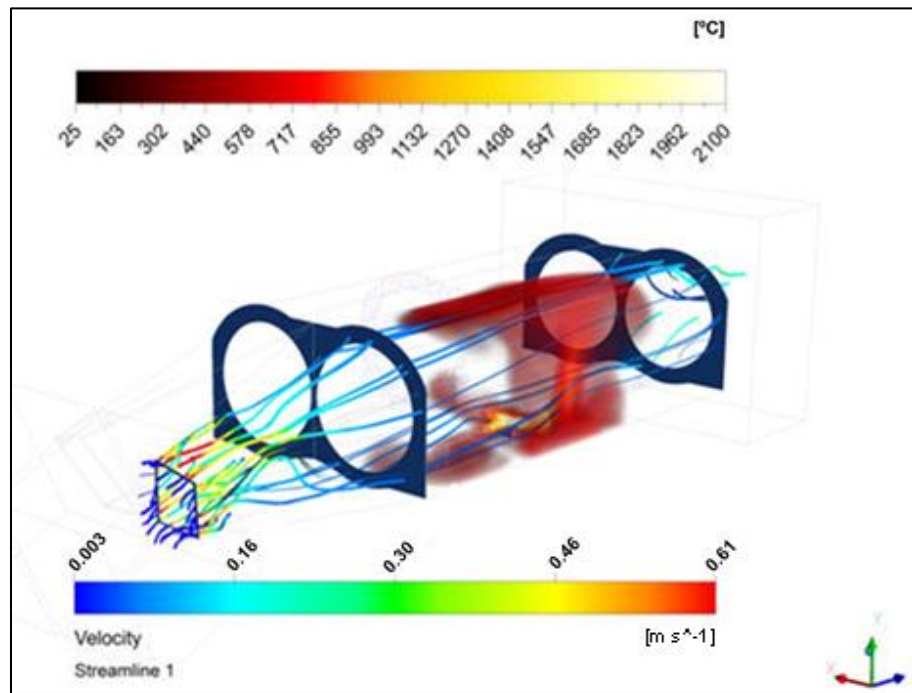


Figure 108. Nacelle Fire and Interior Gas Temperatures

Figure 110 depicts calculated gas temperatures in two planes (or slices) of the modeled nacelle, similar to the gas temperatures shown in Figure 108. The locations of these slices are shown as shaded regions, close to the center. Figure 110 shows the view looking from the back of the nacelle toward the front at four time durations after ignition. Almost all of the elevated temperatures are shown on the right side of the nacelle (left side of Figure 110).

A fire of this type progresses rapidly due to elevated initial temperatures. As a result, analysis of the model results show that composite material surface temperatures at the top of the nacelle reach temperatures exceeding 250 °C just seconds into the fire event and a majority of the surface area of the top wall of the engine nacelle exceeds this temperature in 12 s. Calculations predict that the composite material will reach the measured RM3002 critical temperature of 250 °C where delaminations occurred in the experiments over a large area of the plate within 2 to 5 s (see delamination temperature observations in Section 5.3). These delaminations caused a major reduction in material strength in the experiments.

The conditions on the composite are quite different from the experiments, however, where direct flame impingement causes rapid heating (greater than 150 °C/s versus a maximum of about 15 °C/s in the experiments). Primary decomposition (pyrolysis) of IM7/RM3002 begins at about 400 °C (see Figure 35). Pyrolysis of the nacelle wall would therefore begin at approximately 3 s along the plate edge. Note that this effect is not included in the CFD model as the heat transfer

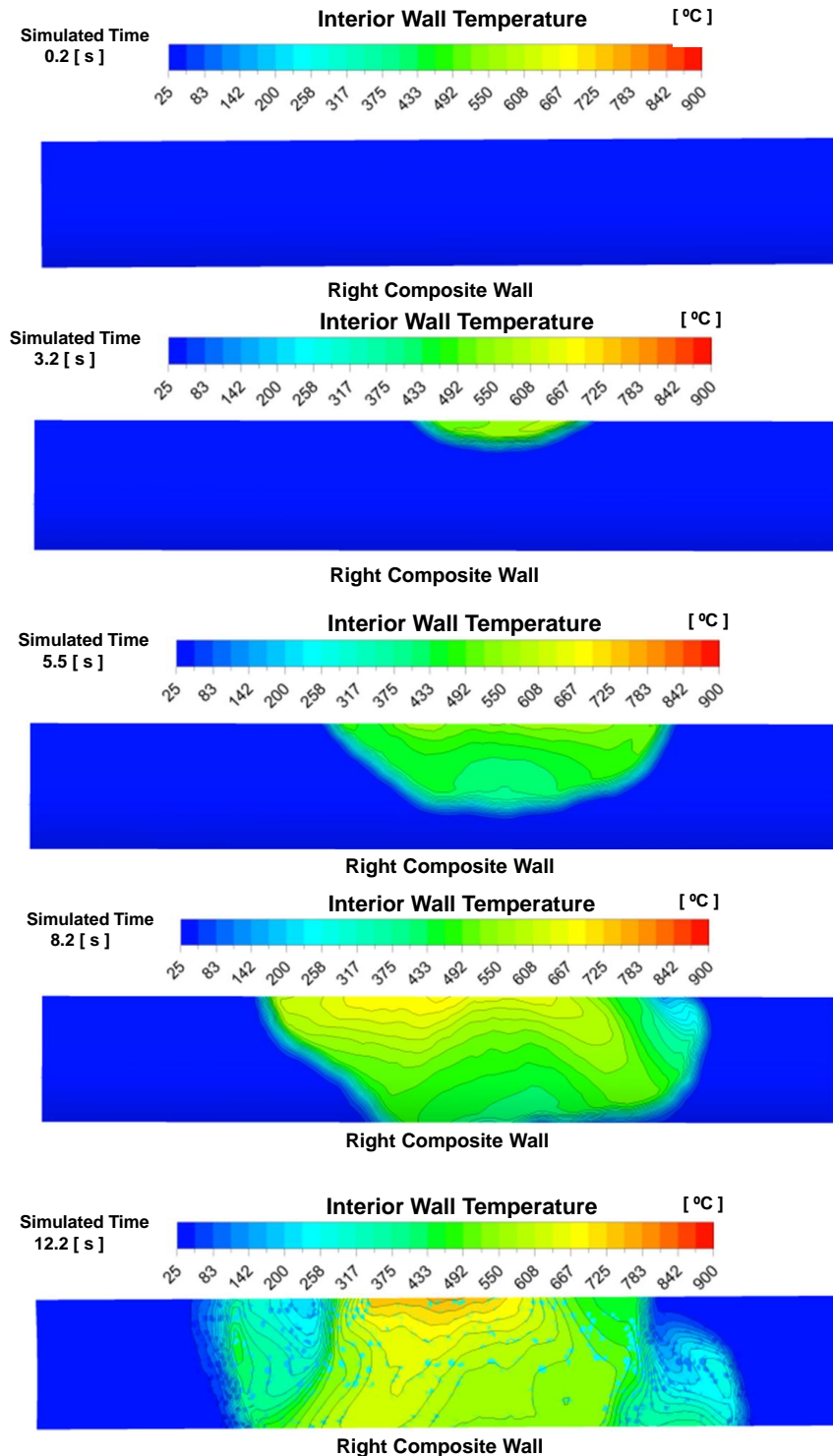


Figure 109. Interior Surface Temperatures of Top Nacelle Plates at Five Time Steps after Fire Ignition (Plan View From Underneath – Engine Inlet on Right)

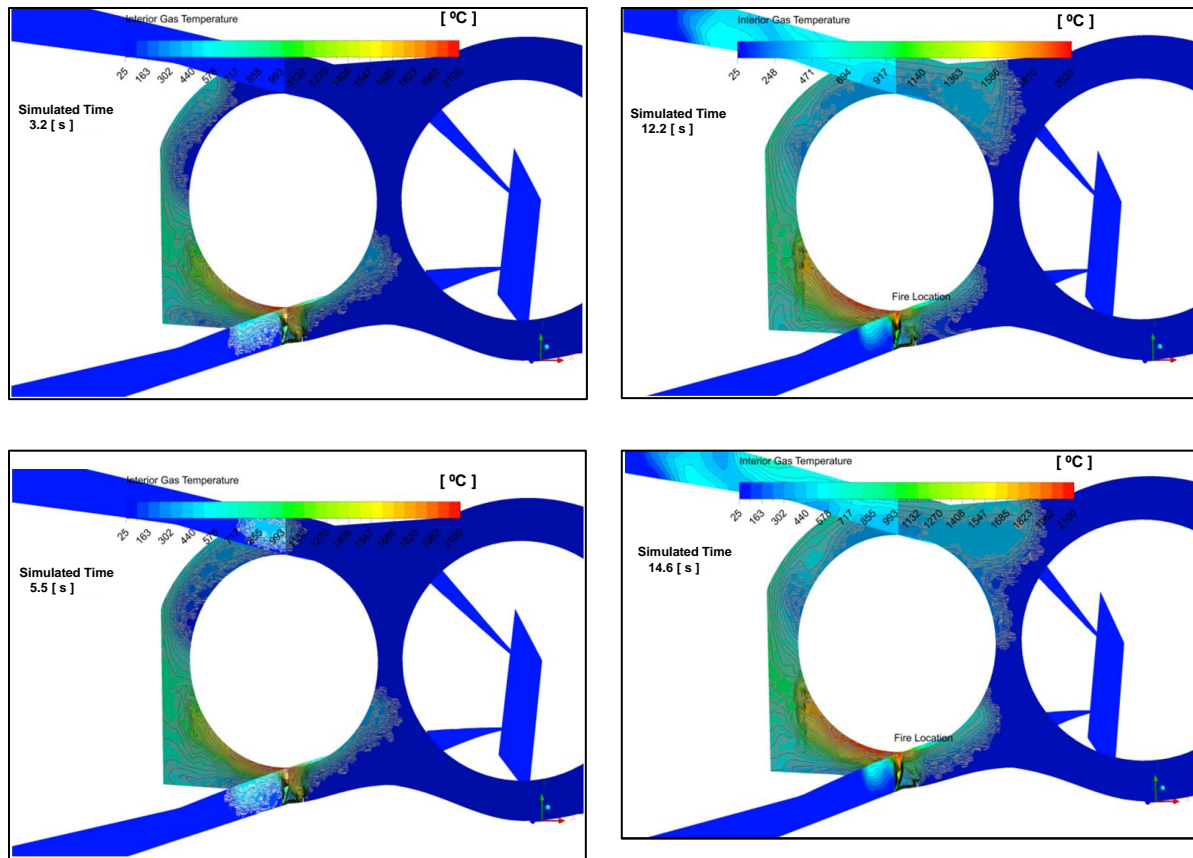


Figure 110. Fire Zone Gas Temperature Profiles in Two Planes at Four Time Steps

and pyrolysis code developed under this effort was not coupled with the CFD code. Results shown in Figure 109, after reaching this temperature, would be affected by this decomposition. Analysis of the composite using the 1-D heat transfer and pyrolysis code shows pyrolysis of the nacelle top plate over a wide area. By 30 s of exposure, the material is more than 50 percent pyrolyzed through 40 percent of the plate thickness. This plate would have very little residual strength or stiffness. The analysis assumed a constant heat flux on the heat-exposed surface of 340 kW/m^2 , which results in the approximate rate of heating seen in the CFD analysis. A more detailed analysis with the code was not performed because composite exposure tests in this study only evaluated lower heat exposures to temperatures below the pyrolysis temperature. Material parameters after pyrolysis begins are therefore only estimates based on other materials studied in the past. The 1-D heat transfer model was not calibrated above pyrolysis temperatures with the available data. Whether delaminations would occur with the pyrolysis occurring concurrently is not known. Either way, it appears that the composite would be rapidly damaged in the first 30 s of exposure.

5.5.3. Small Fuel Spill Model

A second scenario for fire protection response is the case of a small fuel spill fire under the wing of the aircraft. This event was modeled as a 1-m diameter pool fire under one wing representative of a potential 0.025 kg/s (0.5 gal/min) jet fuel spill during refueling. The fuel is

initially at its flash point temperature, 43 °C. Figure 111 shows this scenario in the fire's incipient stage and shows the wind velocity vectors calculated. The geometry in the model of areas impacted by the flame, including the underside of the wing and the lower fuselage, were adequate to determine the impact of the flame on aircraft surface temperatures.

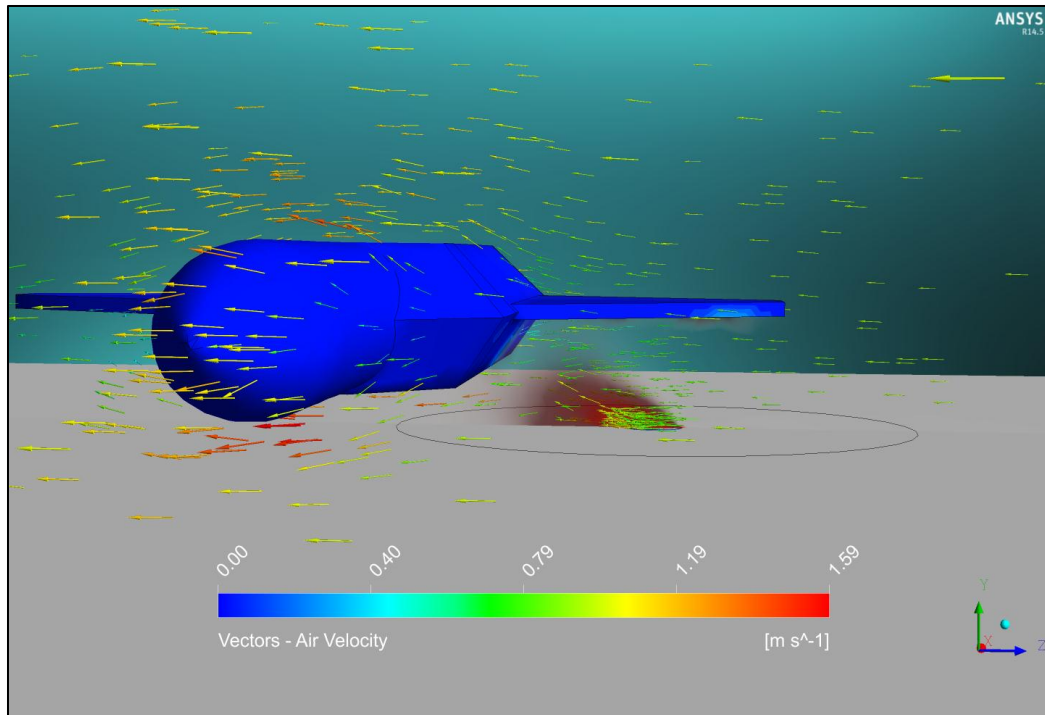


Figure 111. Flow Streams and Fuel Spill Fire

The composite material on the underside of the F-22 wing and the lower fuselage is IM7/5250-4 which is similar to the IM7/RM3002 plates that were evaluated in this test program. The composite in this area was modeled as 3.2 mm (0.125 in) thick with a density of 1,514 kg/m³, specific heat of 2,200 J/g-K, and thermal conductivity of 1.2 W/m-K. Jet fuel combustion was calculated using JetSurF Version 2.0. The model included a cross wind speed of 1 m/s (3.3 ft/s) from the wing tip toward the fuselage across the fire area. This model was used to develop a profile of thermal effects on the composite surfaces that form the lower portion of the wing. Table 8 summarizes the parameters used in the model. As in the engine nacelle model, specific heat and thermal conductivity have non-linear properties but were modeled as constant values here. From Figure 37, both values vary rapidly with temperature, and so average values were used based on preliminary data for IM7/977-3.

Table 8. Summary of the Small Fuel Spill Model

Model Parameter	Value
Fire Size	1 m (3.3 ft) diameter
Fuel Flow Rate	0.025 kg/s (0.5 gal/min)
Fuel Temperature	43 °C
Cross Wind	1 m/s (3.3 ft/s)
Fuel Recession Rate	0.032 kg/m ² -s
Composite Material	IM7/5250-4
Composite Thickness	3.2 mm (0.125 in)
Composite Density	1,514 kg/m ³
Composite Specific Heat	2,200 J/g-K
Composite Thermal Conductivity	1.2 W/m-K
Composite back-side air temperature	300 K

5.5.4. Small Fuel Spill Fire

The jet fuel spill combustion was calculated using JetSurF Version 2.0. This model was used to develop a profile of thermal effects on the composite surfaces that form on the lower side of the aircraft wing. The fuel, initially at flash point temperature, results in the pool fire reaching maximum flame heights in under 10 s after ignition. Figure 111 shows the approximate size of the fire at steady state. This fire will remain this size and continue to cause damage to the aircraft until the fuel flow rate is stopped and the fire burns out or until mitigated by fire extinguishing agents.

This fire scenario results in a high heat flux region on the lower surface of the aircraft wing. The temperature history on the lower wing surface is shown in Figure 112. Figure 113 and Figure 114 show the velocity profile and a contour plot, respectively, of the lower wing surface temperatures 3 s into the fire event.

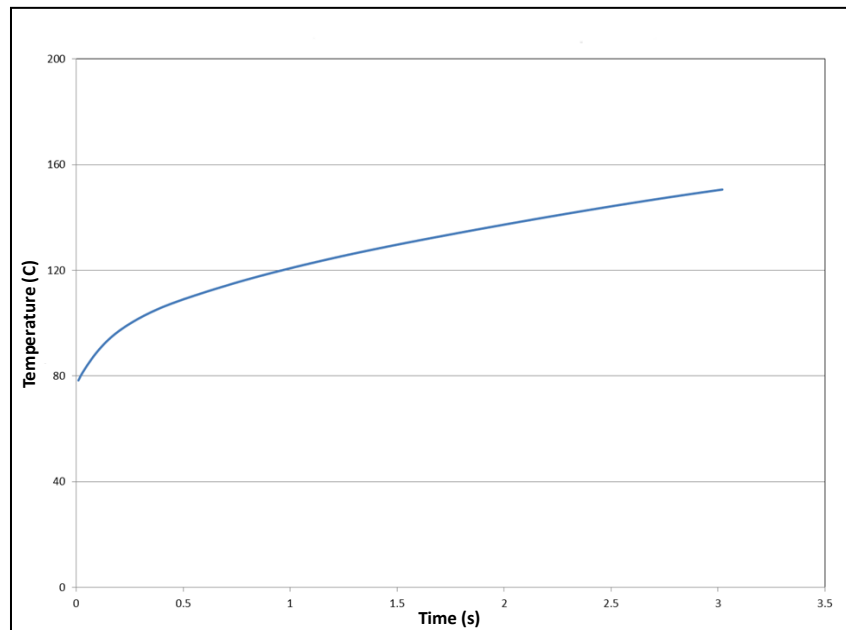


Figure 112. Maximum Surface Temperatures on the Wing Lower Skin

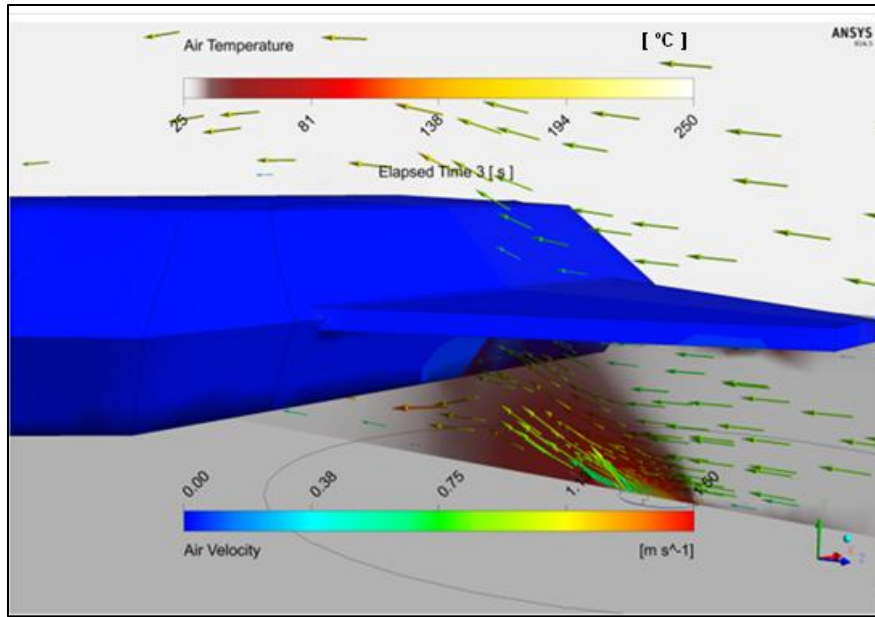


Figure 113. Flow Streams and Fuel Spill Fire at 3 s

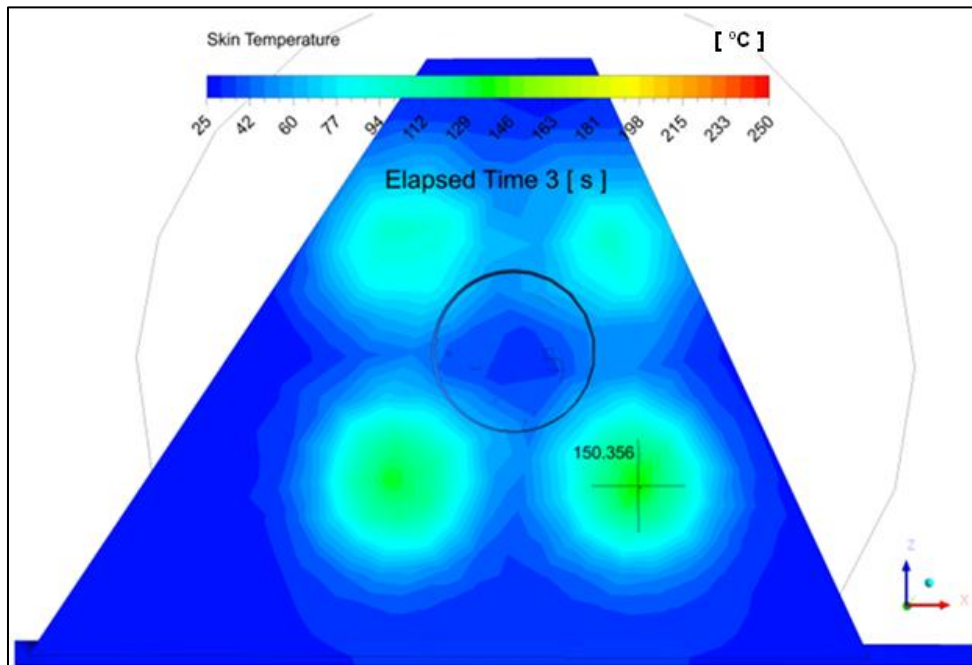


Figure 114. Lower Wing Composite Surface Temperatures at 3 s

The model results at 3 s of fire exposure show that composite material surface temperatures on the wing exceed 150 °C. Based on this rate of surface temperature increase, the critical delamination temperature of 250 °C for this material would be exceeded on the lower wing in less than 45 s.

The time for a spill fire to reach full involvement will vary based on fuel temperatures, type of ignition source, and the mitigation efforts of ground personnel with portable extinguishers. If it is assumed that the fuel temperature is initially well below its flash point, the best case scenario would have the 1-m diameter pool fire reach full involvement approximately 45 s after ignition. This will result in initial damage to the aircraft skin in less than 1.5 min (see delamination temperature observations in Section 5.3).

5.5.5. Small Fuel Spill Fire Adjacent to Aircraft

The results from the two CFD models clearly show that direct flame impingement on composite material surfaces will cause extensive damage in seconds, not minutes. Direct flame impingement can produce a heat flux that equals or exceeds 120 kW/m^2 [31], leading to rapid and severe damage to composite aircraft materials. Less severe damage occurs when direct flame impingement does not occur. Therefore, the thermal loading from fires adjacent to the aircraft was analyzed. In this case, there is predominantly radiant heating on the aircraft surfaces.

A method by Shokri and Beyler [32] can be used for preliminary assessment of liquid hydrocarbon fuel pool fire thermal radiation in kW/m^2 where

$$\dot{q}'' = 15.4 \left(\frac{L}{D} \right)^{-1.59} \quad (5.1)$$

The L is the distance from the center of the fire and D is the diameter of the circular pool fire. Therefore $(L-D/2)$ is the distance from the edge of the fire. The formula calculates values at a height the same as the base of the fire and doesn't take into account the height of the adjacent target. Using this formula (without a safety factor of two that is sometimes used with this equation [31]) with the heat flux values from Table 2 (15, 25, and 35 kW/m^2), the distances from the center of the fire can be calculated for each flux based on the fire diameter. Example results are in Table 9.

Table 9. Heat Flux Adjacent to a Fuel Spill Fire

Jet Fuel Fire Pool Diameter	Distance from center of fire (m) [ft]		
	15 (kW/m^2)	25 (kW/m^2)	35 (kW/m^2)
1 m [3.3 ft]	1.0 [3.3]	0.7 [2.4]	0.6 [2.0]
1.8 m [6 ft]	1.8 [6.0]	1.3 [4.4]	1.1 [3.5]
5 m [16.5 ft]	5.1 [16.7]	3.7 [12.1]	3.0 [9.8]
10 m [33 ft]	10.2 [33.4]	7.4 [24.2]	6.0 [20.0]

Based on the delamination temperatures seen experimentally for the three composites studied (Section 4.3.6), the time to reach these temperatures were calculated using the approximate time to reach delamination temperatures for each of the three classes of composite materials evaluated based on heat flux exposure levels.

For the three composites studied in this program, the time to reach the delamination temperatures discussed in Section 4.3.6 were calculated using the 1-D heat transfer model (Section 4.3) for radiant heat fluxes of 15, 25 and 35 kW/m^2 . These times are shown in Table 10. Note that the thickness of each material is different and represents a nominal thickness of the quasi-isotropic

plates used in the testing. It was assumed that the heat flux was constant at the prescribed value for the duration shown (there was a ramp period in the experiments), and that the back of each plate was perfectly insulated. These are both conservative assumptions for any real structure and real fire. This table and Table 9 can be used together to estimate the time available to extinguish the fires listed in Table 9 before delamination occurs.

Table 10. Delamination Predictions of Composites

Composite Material (Delam. Temp., Thickness)	Time until delamination begins (s)		
	15 (kW/m ²)	25 (kW/m ²)	35 (kW/m ²)
IM7/977-3 (250 C, 0.25 in)	272	142	90
IM7/RM3002 (250 C, 0.13 in)	129	74	51
IM7/AFR-PE-4 (225 C, 0.15 in.)	129	72	47

As an example, a 5 m (16.5 ft) diameter spill fire that is centered 3.7 m (12.1 ft) from a composite surface will result in a heat flux of 25 kW/m² (Table 9). From Table 10, the IM7/977-3 composite material will begin to delaminate in 142 s. If the fire is instead centered 5.1 m (16.7 ft) from the surface the heat flux will be 15 kW/m², and the material will begin to delaminate in 272 s. These longer times seem reasonable for ARFF response time requirements and demonstrate that small adjacent fires can be contained to minimize the risk of heat-induced delaminations in the composite structures.

For general use, Equation 5.1 is used to first calculate the heat flux on the aircraft structure at a given distance from the fire for a specified pool diameter. Then the 1-D heat transfer code is used to calculate the time at which the delamination temperature is reached for the composite material at that location. To eliminate the need of running the 1-D heat transfer code for general use, the code could be exercised by the authors to develop the times to delamination for general offset fire scenarios and composite types and thickness. The results can be provided in three potential forms: (1) tabular form (expanded version of Table 10), (2) surface plots showing time to delamination for each composite layup, or (3) in a simple MS Excel Workbook. The tables and the surface plots would require the user to interpolate for specific fire scenarios not specifically in the table. The Workbook would perform the interpolation for the user. The only output from the Workbook would be a time to delamination with the following user-specified inputs:

1. Distance from the center of the fire – L,
2. Diameter of the circular pool fire – D,
3. Composite type: IM7/RM3002, IM7/977-3, IM7/AFR-PE-4,
4. Layup: [0,90,45,-45]ns, where n=1,2,3, etc. and the ‘s’ indicates a symmetric laminate.

To develop the dataset, variations in laminate thickness would be evaluated based on increments in the symmetric quasi-isotropic layup used in the tests [0,90,45,-45]ns. Three to four thicknesses would be evaluated, depending on the time to delamination. Only balanced, symmetric layups would be considered because it is unknown if other general layups would have similar delamination temperatures. A range of heating intensities would be considered, representing intensities from varied fire diameters and distances.

6. CONCLUSIONS

For all materials and heat flux intensities tested, it was found that the composite materials experienced sudden and catastrophic damage in the form of delaminations, sometimes throughout the entire thickness, prior to any significant charring or mass loss. Delaminated composite material samples displayed little residual mechanical strength in flexure (up to 85 percent strength loss) and greatly reduced tensile strength (up to 40 percent strength loss). In contrast, samples exposed to similar heat flux and durations, but removed from heat prior to delamination, showed little reduction in mechanical strength. The time at which delamination occurred was indicated by thermocouple data and global buckling of the plate. Time to delamination was affected by the moisture content of the plate, with delamination occurring at shorter exposure times for plates with higher moisture content.

Material IM7/RM3002 was tested at all three heat flux intensities in the dry state. The time to delamination ranged from 77 s at the highest heat flux intensity to 231 s at the lowest intensity. With water moisture at 0.4 percent, the delamination time was reduced from 129 s to 106 s at the intermediate heat flux, 25 kW/m².

Material IM7/977-3 was only tested at the lowest heat flux, 15 kW/m². The dry plate delaminated at 437 s. This plate was approximately twice as thick as the other materials due to the larger ply thickness, so the rate of temperature increase for the same heat flux intensity was lower as heat was absorbed into the greater amount of material. The presence of 0.3 % water moisture reduced this delamination time slightly to 421 s.

Material IM7/AFR-PE-4 was only tested at the highest heat flux, and it delaminated at 135 s dry and 77 s with 1.4 percent moisture content. No conclusion can be made at this time about the relative sensitivity to moisture between materials because all of the materials were tested at different moisture content and heat flux combinations. There was not time in the testing program to fully saturate all of the materials and determine their respective changes in delamination time and temperature. This material had the highest T_g and showed the largest reduction in the temperature at which delamination occurs due to the presence of moisture in the composite (26 percent), but it also was tested with the highest moisture content of the three materials. The temperature at which the wet AFR-PE-4 delaminated was well below the dry T_g.

It is postulated that high pressure gases in the plate from water vapor and resin outgassing, coupled with the reduction of the interlaminar strength at elevated temperatures are the cause for the sudden delamination observed in experiments. Once a small crack initiates, strong thermal gradients are produced, and the corresponding thermal stresses drive the delamination further. This mode may not occur when the materials are exposed to a much higher heat flux, such as from ignition and burning of volatiles next to the composite surface. At much higher heat flux intensities pyrolysis at the surface may create an avenue for internal gases to escape through the remaining fibers rather than building up pressure.

To perform the second step in the analysis, prediction of internal temperatures and pyrolysis through the thickness of the composite, a 1-D heat transfer model was developed. The nonlinear material heat transfer and thermogravimetric properties for this model were calibrated using test data for the three composites of interest. The model demonstrated good agreement up to the

delamination temperature ranges seen during panel heat exposure tests. However, these properties are approximate based on fits to the data. More accurate properties can be obtained using test methods specific to measuring temperature-dependent and degree of pyrolysis-dependent thermal conductivity and specific heat. These measurements would improve model predictions for general use. To analyze specific structures in more detail with strong gradients of heat flux across the surface, the thermal damage model would need to be integrated into an existing computational 3-D heat transfer code.

There are currently no models that can predict the thermally-induced delaminations seen in the experiments. Therefore, Step 3 of the analysis, to predict mechanical degradation of the material as a function of time, cannot currently be performed with the desired accuracy. Although the 1-D heat transfer model can be used to predict temperatures up to delamination, there are currently no good criteria for predicting when this damage occurs. A thermodynamic-mechanical model to predict delamination initiation and growth in general structural laminates is needed before a complete analysis can be performed.

In the absence of a robust method for predicting composite mechanical degradation as a function of time with the dominant damage from heat-induced delaminations, an interim solution is to use maximum allowable temperatures based on the results from the limited testing performed. This is not a comprehensive method for ensuring that delamination does not occur for general laminates and heat flux histories, but is the best that can be recommended based on the current understanding of the damage initiation and growth. This is especially true because the effect of water moisture in the IM7/AFR-PE-4 laminate causes delamination well below the dry T_g. These temperatures may also lead to extremely short response time requirements. Additional heat exposure and mechanical testing are needed to develop a thermodynamic-mechanical delamination model to improve these predictions.

The following are the interim recommendations for limiting temperatures in the three materials evaluated to prevent delamination from occurring:

- Limit temperatures to 250 °C for IM7/977-3.
- Limit temperatures to 250 °C for IM7/RM3002.
- Limit temperatures to 225 °C for IM7/AFR-PE-4.

For the limited test conditions evaluated, IM7/977-3 and IM7/RM3002 showed no delaminations when any part of the material was below 250 °C, with and without water moisture. Although IM7/AFR-PE-4 (the material having the highest dry T_g) delaminated with a minimum plate temperature of about 340 °C, this temperature was reduced to 225 °C with water moisture in the plate.

High-fidelity simulations of aircraft fires either in the interior of the engine nacelle and on the ground beneath the wing when flames impinge on the composite material surface indicate that damage would likely occur within the first minute or less, based on the temperature restrictions above and the degree of pyrolysis calculated. Although this result is from only two fire scenarios, the fire sizes selected were small (6.81 liter/min in the engine nacelle and a 1-m diameter, 1.89 liter/min pool fire on the ground).

In the engine nacelle scenario, the rapid heating makes either delamination and/or severe pyrolysis of the composite likely in less than 30 s. The composite material surface temperatures

at the top of the nacelle exceed the criteria for delamination found in experiments within 5 s of exposure. By 30 s of exposure, the nacelle top plate is more than 50 percent pyrolyzed through 40 percent of the plate thickness. This plate would have very little residual strength or stiffness. Whether delaminations would occur with the pyrolysis occurring concurrently is not known. Either way, it appears that the composite would be rapidly damaged in the first 30 s of exposure. In the scenario with a small fuel spill beneath the wing, the model results indicate that the critical delamination temperature for the wing composite material would be exceeded on the lower wing in less than 45 s.

Radiant heating on a surface from adjacent pool fires (no direct flame impingement) was predicted with a simple analytical model. This model is based on spill fire size and distance from the center of the fire to predict heat flux. This heat flux was then used as input to the 1-D heat transfer model developed under this effort to predict material temperatures versus time. The time at which the temperature restrictions are reached are then determined for each fire scenario for a given composite type and thickness. Use of this model demonstrated that many pool fires close to the aircraft can result in radiant heating such that composite delamination occurs in over two to three minutes for the thicknesses tested in this research.

To eliminate the need of running the 1-D heat transfer code for analysis of other fire scenarios, the code could be exercised by the authors to develop the times to delamination for general offset fire scenarios and composite types and thickness. The results can be provided in three potential forms: (1) tabular form (expanded version of Table 10), (2) surface plots showing time to delamination for each composite layup, or (3) in a simple MS Excel Workbook. The tables and the surface plots would require the user to interpolate for specific fire scenarios not specifically in the table. The Workbook would perform the interpolation for the user. The only output from the Workbook would be a time to delamination. Development of the Workbook or tables was not performed because of the preliminary nature of the criteria for preventing delamination.

Finally, ignition of volatiles at the heat exposed surface did not occur in any of the tests due to the low-intensity radiant heating. With surface ignition, or much higher heat flux intensities, pyrolysis has been observed in other composite material systems as the dominant damage mechanism, as opposed to sudden delaminations. It is not known which form of heating leads to shorter response time requirements for these materials. Additional testing with ignition at the surface would be required to make this determination.

7. RECOMMENDATIONS

The following are operational and technical recommendations based on the results from this research.

7.1. Operational Recommendations

For small fires with direct flame impingement on the aircraft, which will likely rapidly raise temperatures above the critical thresholds, the following actions are recommended:

1. Work with ground support organizations to maintain and improve the ability of ground support personnel to provide effective initial response to fires involving composite aircraft during maintenance, pre-flight and post-flight operations.
2. Work with SPOs to develop ground CONOPs and system retrofits to mitigate fire hazards identified in various weapons systems.
3. Work with MAJCOM Fire Chiefs in establishing response plans and CONOPS that acknowledge the enhanced risk associated with composite aircraft fire hazards.
4. Support research and development activities which will result in mitigation and/or reduction of fire risk in composite aircraft.

For small fires adjacent to the aircraft where the dominant mode of heating is from thermal radiation of the pool fire, the interim approach proposed in this report for predicting time to delamination is recommended. It should be stressed that this approach is based on limited testing and a limited understanding of how and when these catastrophic delaminations occur in the materials studied.

7.2. Technical Recommendations

7.2.1. Heat Exposure Testing

Further heat exposure tests should be conducted on the materials of interest at varied heat flux and water moisture levels. Although IM7/AFR-PE-4 was close to fully saturated at the time of testing, it is unknown what water moisture saturation level the other materials would have attained. Likewise, the only material tested at multiple heat fluxes was IM7/RM3002. As there are remaining plates of material with embedded TCs for IM7/977-3 and AFR-PE-4, some of this testing could be performed without further purchase of material.

Heat exposure tests should also be expanded to include the following:

- Testing at additional water moisture levels, laminate thickness and layups.
- Testing in a mechanically-constrained condition to inhibit global buckling in order to exam the effect on damage in the plates. The current unconstrained testing led to global buckling, which may have induced more damage than in a constrained plate.
- Testing under load. Mechanical stresses due to loading may cause the heat-induced delaminations seen during testing to occur at even lower temperatures. Realistic loads for structures in the aircraft during a given fire scenario are recommended (e.g., gravity loading on structures around the landing gear).

- Testing with ignition of volatiles at the heat-exposed surface.

7.2.2. Thermally-induced Delamination Model

A model should be developed to predict the thermally-induced delaminations seen in the experiments. This model may take the form of a thermodynamics-mechanics based model where the high pressure gases from release of volatiles and water vapor drive initial cracks (flaws) in the material. As the fracture toughness of the matrix is reduced with temperature, and any thermal stress-induced gradients, the crack will grow into a delamination. Significant experimental data are needed to support the development of such a model, including

- Evaluation of delamination fracture toughness as a function of temperature.
- Decomposition kinetics testing by TGA and mass spectroscopy to determine the rate of gas release and chemical composition as a function of time and temperature.
- Heat exposure experiments of plates with varied stacking sequence and thickness to validate the model.

7.2.3. Heat Transfer Modeling

The material properties used in the composite heat transfer model were calibrated to test data for the three CFRP systems evaluated. The calibrated properties are estimates and should be better characterized using test methods specific to measuring through-thickness thermal conductivity and specific heat in order to improve model predictions for general use [e.g., 26].

In some structures the post-delamination heat transfer behavior may be of interest for further damage analysis. The heat transfer model would need further development to predict this behavior. Improvements would involve two major components: (1) a thermomechanical model to predict delamination (Section 7.2.2 above) and (2) modification to the heat transfer code to allow for heat transfer across cracks between plies.

7.2.4. High-Fidelity Modeling and Simulation

To analyze structures in more detail with strong gradients of heat flux across the surface, and varied composite stacking sequences and thicknesses used in real structures, the heat transfer and thermal damaged models (Sections 7.2.2 and 7.2.3 above) would need to be integrated into an existing computational 3-D heat transfer and structural analysis code. This is recommended to improve the accuracy of results in general application.

Finally, although these recommendations would directly support the development of tools for predicting firefighting response times, they would also benefit the aircraft design community to develop more fire and heat-resistant structures.

8. REFERENCES

1. On 20 December 2004, at 2340Z/1540 local time, the Mishap Aircraft, F/A-22, Serial Number 00-4014, crashed on initial takeoff from Nellis AFB
2. Keerigan, Kevin, ["B-2 Fire at AAFB Back in February of 2010 Was 'Horrific,' Not 'Minor'."](#) *pacificnewscenter.com*, 1 September 2011. Retrieved: 5 January 2012.
3. Mayer, Daryl, "Program office brings home 'wounded warrior'." *wpaafb.af.mil*. Retrieved: 5 January 2012.
4. Gibbs, J. H. and DiMarzio, E. A. Nature of the Glass Transition and the Glassy State, *J. Chem. Phys.* 28, 373 (1958).
5. Shen, C. and G.S. Springer, "Moisture Absorption and Desorption of Composite Materials", *J. of Composite Materials*, Vol. 10, January, 1976, pp. 2-20.
6. ASTM D 3039-08. Standard Test Method for Tensile Properties of Polymer Matrix Composite Materials.
7. ASTM D 6272 - 10 Standard Test Method for Flexural Properties of Unreinforced and Reinforced Plastics and Electrical Insulating Materials by Four-Point Bending.
8. Steinhaus, T., Welch, S., Carvel, R., and Torero, J.L. (2007), "Large-Scale Pool Fires," *Thermal Sciences Journal*. Vol. 13 Issue 13 (special on fire).
9. Tieszen, S., Nicolette, V.F., Gritzo, L.A., Holen, J.k., Murray, D., and Moya, J.L. (1996), "Vortical Structures in Pool Fires: Observations, Speculation, and Simulation," Sandia Report SAND96-2607
10. ANSYS FLUENT Theory Guide, Chapter 8. Non-Premixed Combustion, Release 14.0 - © 2011 SAS IP, Inc.
11. H. Wang, E. Dames, B. Sirjean, D. A. Sheen, R. Tangko, A. Violi, J. Y. W. Lai, F. N. Egolfopoulos, D. F. Davidson, R. K. Hanson, C. T. Bowman, C. K. Law, W. Tsang, N. P. Cernansky, D. L. Miller, R. P. Lindstedt, A high-temperature chemical kinetic model of *n*-alkane (up to *n*-dodecane), cyclohexane, and methyl-, ethyl-, *n*-propyl and *n*-butyl-cyclohexane oxidation at high temperatures, JetSurF version 2.0, September 19, 2010 (<http://melchior.usc.edu/JetSurF/JetSurF2.0>).
12. Technical Order 00-105E-9, Aerospace Emergency Rescue and Mishap Response Information (Emergency Service) and NATO Standardization Agreement 3896, Revision 15, Segment 12, HQ AFCEA at: HSAFCEA.CEXF@tyndall.af.mil , 31 March 2011.
13. A.G. Gibson, P.N.H. Wright, Y.-S. Wu, A.P. Mouritz, Z. Mathys and C.P. Gardiner, "The Integrity of Polymer Composites During and After a Fire", *Journal of Composite Materials*, Vol. 38, No. 15, (2004), pp. 1283-1307.
14. A.P. Mouritz and Z. Mathys, "Mechanical properties of fire-damaged glass reinforced phenolic composites", *Fire Mat* (2000), Volume 34, pp. 67-75.
15. A.P. Mouritz and Z. Mathys, "Post-fire mechanical properties of marine polymer composites", *Composite Structures* (1999), Volume 47, pp. 643-653.

16. A.P. Mouritz and Z. Mathys, "Post-fire mechanical properties of glass reinforced polyester composites" *Composites Science and Technology* (2001), Volume 61, pp. 475–90.
17. A.P. Mouritz and Z. Mathys, C.P Gardiner, "Thermomechanical modeling the fire properties of fibre-polymer composites", *Composites, Part B*, Volume 35 (2004), pp. 467-474.
18. N. Dodds, A.G. Gibson, D. Dewhurst, J.M. Davies, "Fire Behaviour of Composite Laminates," *Composites, Part A*, No. 31 (2000), pp. 689-702.
19. Holmes, B.S., Kirkpatrick, S.W., MacNeill, R.A., and Bocchieri, R.T., "Space Based Lethality Target Hardening Support for BMDO," ARA Project 0724, Final Report, August 2002.
20. H.E. Read and M.H. Rice, "Failure of Solid Rocket Engines Due to Laser Radiation Exposure," S-Cubed Report No. SSS-DFR-93-14222, December 1993.
21. H.H. Legner, et al., "Laser Material Effects and Lethality Handbook," Physical Sciences Incorporated Report No. PSI 1302/TR-1615[I-VI], August 1999.
22. S. Ledakowicz and P. Stolarek, "Kinetics of Biomass Thermal Decomposition," *Chemical Papers* (2002), Volume 56, Number 6, pp. 378–381.
23. A.P. Mouritz, Z. Mathys, and A.G. Gibson, "Heat Release of Polymer Composites in Fire", *Composites, Part A*, Volume 37 (2006), pp. 1040-1054.
24. ASTM Standard E1641-07. Standard Test Method for Decomposition Kinetics by Thermogravimetry.
25. J.G. Quintere, R.N. Walters, and S. Crowley, "Flammability Properties of Aircraft Carbon-Fiber Structural Composite," FAA Report DOT/FAA/AR-07/57, Federal Aviation Administration, October 2007.
26. "Thermophysical Properties of Composite Materials," TPRL, Inc. Report Number 2263, November 1999.
27. J.K. Chen, et al, "A Study of Laser/Composite Material Interactions," *Composites Science and Technology*, 54 (1995) 35-44.
28. C.A. Griffis, R.A. Masumura, and C.I. Chang, "Thermal Response of Graphite Epoxy Composite Subjected to Rapid Heating," NRL Memorandum Report 4479, Naval Research Laboratory, March 1981.
29. R.M. Jones, Mechanics of Composite Materials, Hemisphere Publishing Company, New York, 1975.
30. Chang, F.K. and K.Y. Chang, "A Progressive Damage Model for Laminated Composites Containing Stress Concentration," *J. of Composite Materials*, 21, 834-855, 1987.
31. Beyler, Craig L. "*Fire Hazard Calculations for Large, Open Hydrocarbon Fires*". The SFPE Handbook of Fire Protection Engineering Third Edition. 2002
32. Shokri, M., Beyler, C.L., "*Radiation from Larger Pool Fires*" *SFPE Journal of Fire Protection Engineering*, 4, 1, pp.141-150. 1989.

APPENDIX

A.1. Tensile Data Summaries

Table A-1. RM-3002

Test Sample Number	Failure Code [6]*	Tensile Strength (MPa)	Tensile Strain ($\mu\epsilon$)	Modulus of Elasticity (GPa)
R-3	XGV	867	12,548	71.7
R-4	XGV	858	13,421	73.8
R-5	XGV	901	12,389	73.9
R2-14	XGV	699	12,896	64.8
R2-16	XGV	704	15,403	56.4
R2-18	XGV	721	16,354	63.7
R3-13	XGV	779	14,549	59.1
R3-14	XGV	795	13,874	59.9
R3-15	XGV	813	14,520	60.6
R3-16	XGV	814	15,292	59.4
R3-17	XGV	820	14,446	57.2
R3-18	XGV	837	14,756	57.1
R4-13	XGV	827	14,646	69.1
R4-14	XGV	847	14,792	68.2
R4-15	XGV	824	14,077	71.0
R4-16	XGV	824	13,356	71.1
R4-17	XGV	844	13,995	70.9
R4-18	XGV	825	12,433	68.0
R6-13	N/A			61.5
R6-14	XGV	692	13,680	64.6
R6-15	N/A			62.6
R6-16	N/A			62.4
R6-17	XGV	671	13,742	62.9
R6-18	XGV	679	13,723	65.9
R7-13	N/A			61.5
R7-14	XGV	812	13,608	63.4
R7-15	XGV			62.0
R7-16	N/A			58.3
R7-17	XGV	814	14,514	61.6
R7-18	XGV	764	13,617	59.2

* XGV - eXplosive, Gage, Various

Table A-1. RM-3002 (Cont.)

Test Sample Number	Failure Code [6]*	Tensile Strength (MPa)	Tensile Strain (µε)	Modulus of Elasticity (GPa)
R8-13	XGV	654	11,274	61.7
R8-14	XGV	685	11,699	62.3
R8-15	XGV	698	12,954	61.7
R8-16	N/A			61.0
R8-17	XGV	739	13,670	65.1
R8-18	XGV	686	13,452	59.4

* XGV - eXplosive, Gage, Various

Table A-2. AFRPE

Test Sample Number	Failure Code [6]*	Tensile Strength (MPa)	Tensile Strain (µε)	Modulus of Elasticity (GPa)
A-3	LIB	719	13,877	52.1
A-4	LVV	762	14,641	52.1
A-5	LIB	738	14,468	53.0
A3-13	LAT and XWB	681	13,627	50.3

* LIB – Lateral, Inside grip/tab, Bottom
LVV - Lateral, Various, Various
LAT - Lateral, At grip/tab, Top
XWB - eXplosive, <1W from grip/tab, Bottom

Table A-3. CYCOM

Test Sample Number	Failure Code [6]*	Tensile Strength (MPa)	Tensile Strain (µε)	Modulus of Elasticity (GPa)
C-13	XGV	715	12,941	61.0
C-15	XGM	736	13,423	61.7
C-16	XGM	746	14,080	59.7
C4-13	XGV	451	12,618	47.5
C4-14	XGV	431	11,994	45.5
C4-15	XGV	416	11,333	48.8

* XGV - eXplosive, Gage, Various
XGM - eXplosive, Gage, Middle

A.2. Bend Data Summaries

Table A-4. RM-3002

Test Sample Number	Exposed Side	Flexural Strength (MPa)	Flexural Strain (mm/mm)	Chord Modulus (GPa)	Failure Type
R-10	Tension	870	0.0136	65.9	compression with delamination
R-11	Tension	957	0.0137	72.0	compression
R-12	Tension	926	0.0128	73.7	compressive delamination
R-13	Tension	954	0.0135	71.9	compression
R-14	Compression	812	0.0115	72.1	compression with delamination
R-15	Compression	760	0.0101	75.2	compressive delamination
R2-1	Tension	266	0.0049	56.5	lateral delamination
R2-2	Tension	233	0.0052	55.1	end delamination
R2-3	Tension	220	0.0062	40.5	compressive delamination
R2-4	Tension	186	0.0078	37.6	compressive delamination
R2-5	Compression	208	0.0059	37.2	compressive delamination
R2-6	Compression	171	0.0056	32.6	compressive delamination
R2-7	Compression	138	0.0068	26.9	compressive delamination
R2-8	Compression	170	0.0064	34.8	compressive delamination
R2-9	Compression	207	0.0059	42.7	compressive delamination
R3-1	Tension	975	0.0123	77.5	compression with delamination
R3-2	Tension	848	0.0110	76.8	compression
R3-3	Tension	916	0.0117	77.6	compression with delamination
R3-4	Tension	892	0.0117	77.7	compression with delamination
R3-5	Compression	808	0.0103	84.8	compression with delamination
R3-6	Compression	864	0.0118	75.9	compression
R3-7	Compression	866	0.0109	81.6	compression
R3-8	Compression	843	0.0117	81.3	compression
R3-9	Compression	869	0.0112	77.2	compression

Table A-4. RM-3002 (Cont.)

Test Sample Number	Exposed Side	Flexural Strength (MPa)	Flexural Strain (mm/mm)	Chord Modulus (GPa)	Failure Type
R4-1	Tension	911	0.0114	83.2	compression
R4-2	Tension	875	0.0113	77.7	compression with delamination
R4-3	Tension	981	0.0114	87.7	compressive delamination
R4-4	Tension	872	0.0117	76.3	compression
R4-5	Compression	891	0.0114	81.7	compression
R4-6	Compression	754	0.0097	78.5	compression
R4-7	Compression	942	0.0115	84.5	compression
R4-8	Compression	982	0.0113	89.8	compressive delamination
R4-9	Compression	766	0.0103	79.4	compression
R6-3	Tension	155	0.0068	29.3	end delamination
R6-4	Tension	137	0.0062	26.1	lateral delamination
R6-6	Tension	201	0.0077	31.6	end delamination
R6-8	Tension	146	0.0052	28.8	lateral and end delamination
R6-1	Compression	223	0.0048	51.1	lateral and end delamination
R6-2	Compression	180	0.0070	32.6	end delamination
R6-5	Compression	166	0.0082	23.6	lateral delamination
R6-7	Compression	195	0.0087	27.6	end delamination
R6-9	Compression	152	0.0052	33.6	compressive delamination

Table A-4. RM-3002 (Cont.)

Test Sample Number	Exposed Side	Flexural Strength (MPa)	Flexural Strain (mm/mm)	Chord Modulus (GPa)	Failure Type
R7-2	Tension	894	0.0122	72.6	compression
R7-4	Tension	884	0.0116	77.9	compressive delamination
R7-6	Tension	864	0.0116	76.5	compression with delamination
R7-8	Tension	970	0.0121	80.4	compressive delamination
R7-1	Compression	724	0.0094	81.7	compression
R7-3	Compression	802	0.0099	79.9	compressive delamination
R7-5	Compression	892	0.0110	82.1	compression with delamination
R7-7	Compression	763	0.0106	74.9	compression
R7-9	Compression	707	0.0094	75.1	compressive delamination
R8-2	Tension	239	0.0048	56.9	compressive delamination
R8-4	Tension	260	0.0052	52.3	end delamination
R8-6	Tension	222	0.0042	57.7	end delamination
R8-8	Tension	247	0.0049	57.2	end delamination
R8-1	Compression	310	0.0053	62.9	end delamination
R8-3	Compression	335	0.0047	71.7	end delamination
R8-5	Compression	226	0.0052	49.7	end delamination
R8-7	Compression	231	0.0063	47.0	end and compressive delamination
R8-9	Compression	274	0.0048	62.7	compressive delamination

Table A-5. AFRPE

Test Sample Number	Exposed Side	Flexural Strength (MPa)	Flexural Strain (mm/mm)	Chord Modulus (GPa)	Failure Type
A-2	Tension	614	0.0113	60.7	compression
A-4	Tension	643	0.0124	62.3	compression
A-6	Tension	659	0.0107	62.8	end compression
A-1	Compression	707	0.0119	64.4	lateral delamination
A-3	Compression	762	0.0119	69.4	end delamination
A-5	Compression	695	0.0115	62.9	lateral delamination
A3-2	Tension	450	0.0138	40.3	end delamination
A3-4	Tension	393	0.0099	44.0	compression
A3-6	Tension	447	0.0100	46.8	end delamination
A3-8	Tension	603	0.0099	62.1	lateral delamination
A3-1	Compression	662	0.0109	63.1	end delamination
A3-3	Compression	337	0.0089	48.1	end delamination
A3-5	Compression	385	0.0088	43.4	lateral and end delamination
A3-7	Compression	463	0.0088	59.3	end delamination
A3-9	Compression	580	0.0087	68.0	bend

Table A-6. CYCOM

Test Sample Number	Exposed Side	Flexural Strength (MPa)	Flexural Strain (mm/mm)	Chord Modulus (GPa)	Failure Type
C-2	Tension	663	0.0104	60.3	lateral delamination
C-5	Tension	757	0.0121	63.1	lateral and compressive delamination
C-7	Tension	713	0.0110	61.9	lateral and compressive delamination
C-1	Compression	658	0.0105	62.7	compression with delamination
C-4	Compression	753	0.0139	66.5	lateral and compressive delamination
C-6	Compression	619	0.0091	69.2	compressive delamination
C4-2	Tension	130	0.0079	25.3	lateral and end delamination
C4-4	Tension	96	0.0051	20.5	lateral delamination
C4-6	Tension	95	0.0058	19.9	end delamination
C4-8	Tension	121	0.0076	26.4	end delamination
C4-1	Compression	162	0.0074	39.8	lateral and end delamination
C4-3	Compression	115	0.0095	24.0	lateral and end delamination
C4-5	Compression	100	0.0068	22.2	lateral and end delamination
C4-7	Compression	119	0.0107	30.8	lateral and end delamination
C4-9	Compression	149	0.0072	35.9	end and compressive delamination

A.3. Data Sheets

Composite IR Heater Test Data Sheet

Test Date: _____ Start Time: _____

Location: AFRL Tyndall AFB, FL – Building 9443
Fire Garage

Composite Material: _____

Sample Number: _____

Sample PreConditioning: _____

Previously Recorded Weight: _____ g Initial Weight: _____ g

Table Height: _____ from the bottom of HF1 to the bottom of IR Heater frame

Check the three TC's in the center, they should be pointed up, just past the surface of the bottom insulation, and can push straight down with light finger pressure.

Edge Shield Material: _____

The entire front surface is exposed.

IR Heater SetPoint: _____ °C	35kW/m ² → 825 °C	start test at 824-825 °C
	25kW/m ² → 730 °C	start test at 731-730 °C
	15kW/m ² → 610 °C	start test at 611-610 °C

Desired Exposure Time: _____ s

Data Recorded As: _____

Remove table and composite plate from heat.

Immediately turn on fan that is 3.05 m away, blowing parallel to exposed surface.

Continue with cooling until all embedded Thermocouples are below 170°C.

Wind Speed: _____ Temp: _____ °C Humidity: _____ percent

Exposure Time to hear audible composite popping: _____ s

Actual Exposure Time: _____ s

Describe Sample Damage:

Resulting Fire:	_____
Texture:	_____
Color:	_____
Additional:	_____

Final Weight: _____ g

Comments:

Composite Tensile Test Data Sheet

Test Date: _____ Start Time: _____
Test Conductor: _____ Operator: _____

Location: AFRL Tyndall AFB, FL – Building 9742

Controlled Laboratory Environment

Temperature: _____ Relative Humidity: _____ percent

Composite Material: _____ Cut Using: _____

Fiber Orientation: _____°

Sample Number: _____

Sample PreConditioning: _____

Overall Length: _____

Gage Width 1: _____

Gage Thickness 1: _____

Gage Width 2: _____

Gage Thickness 2: _____

Gage Width 3: _____

Gage Thickness 3: _____

Average Width: _____

Average Thickness: _____

Grip Length: _____

Tabs Used? Yes / No

Tab Material: _____ Tab Thickness: _____

Bevel Angle: _____° Overall Tab Length: _____

Fiber Orientation: _____° Epoxy Adhesive: _____

Overall thickness: _____ Top End: _____ Bottom End: _____

Grip Type: _____ Pressure: _____

Grip Surface: _____

Rotationally Self-Aligning? Yes / No

Front Strain: _____ Gage Length: _____ Strain: _____ percent

Back Strain: _____ Gage Length: _____ Strain: _____ percent

Initial Readings: Before Bottom Gripped After Bottom Gripped

Front: _____

Back: _____

Head-Speed Rate: _____ Data Sample Rate: _____/s

Data to record: Axial Displacement, Axial Force, Axial Extensometer, Time

Data Recorded As: _____

Ultimate Tension: _____ mm _____ min _____ sec

Three Part Failure Mode Code: _____

Comments:

Composite 4-Point Bend Test Data Sheet

Test Date: _____ Start Time: _____
Test Conductor: _____ Operator: _____
Location: AFRL Tyndall AFB, FL – Building 9742

Controlled Laboratory Environment
Temperature: _____ Relative Humidity: _____ percent

Composite Material: _____ Cut Using: _____
Fiber Orientation: _____°
Sample Number: _____
Sample PreConditioning: _____

Overall Length: _____
Gage Width 1: _____ Gage Thickness 1: _____
Gage Width 2: _____ Gage Thickness 2: _____
Gage Width 3: _____ Gage Thickness 3: _____
Average Width: _____ Average Thickness: _____

Deflection Measuring Device: _____

Material	Fixture	Crosshead Rate (mm/min)	Max. Deflection (mm)
Cycom	Large	2.64	15.01
RM3002	Small	3.33	18.90
AFRPE	Small	2.82	16.00
Cytec	Small	6.83	25.40

Fixture Used: Large: 31.75 mm load span, 95.25 mm support span, 9mm radii
Small: 25.4 mm load span, 76.2 mm support span, 5mm radii

The Loading Nose assembly shall be of the type which will not rotate.
Check for Loading Nose and Support parallelism with the cut-out plate.

Crosshead Rate: _____ mm/min
Max. Deflection / Crosshead Rate = _____ min = _____ min _____ sec

Data Sample Rate: _____/s
Data to record: Axial Displacement, Axial Force, Deflection, Time
Data Recorded As: _____

Maximum Force: _____ mm _____ min _____ sec
Pause the test when the applied load drops; take close up pictures of sample under this load.
Stop the test, remove the load, then the sample from the fixture; take more pictures.

Calculated Support Span to Depth Ratio: _____

Comments:

LIST OF SYMBOLS, ABBREVIATIONS, AND ACRONYMS

°C	degree(s) Celsius
°F	degree(s) Fahrenheit
%	percent
1-D	one-dimensional
3-D	three-dimensional
ρ	density
ΔH	heat generated/absorbed
σ	the Stephan-Boltzmann constant
ε	emissivity
$\mu\varepsilon$	micro strain, strain (in/in) $\times 10^6$
A.C.S.	American Chemical Society
AFRL	Air Force Research Laboratory
AFOSR	Air Force Office of Scientific Research
APU	auxiliary power unit
ARFF	aircraft rescue firefighting
BMI	bismaleimide polymer
c	specific heat
CFD	computational fluid dynamics
CFRP	carbon fiber reinforced polymer
CMAAP	Composite Material Analysis Program
CONOPS	concept of operations
CYCOM 977-3	epoxy IM7/977-3 carbon fiber composite
DoD	Department of Defense
ERDC	US Army Corps of Engineers Engineer Research and Development Center
IM7	intermediate modulus carbon fiber
IR	infrared
FE	finite element
ft	foot; feet
gal	gallon(s)
h	convection coefficient
in	inch(es)
k	thermal conductivity
ksi	1000 pounds per square inch
kW	1000 watts
kW/m ²	1000 watts per square meter
lbf	pound force
m	meter (s)
min	minute(s)
MPa	1,000,000 Pascals
NA	non-adiabatic
NIST	National Institute of Standards and Technology
PDF	probability density function
Q (q) or q''	heat flux measured in kW/m ²
rpm	rotations per minute

s	second (s)
SPO	System Program Office
STD	standard deviation
TC	thermocouple
TGA	thermogravimetric analysis
T _g	glass transition temperature